REDUCED GRAPHENE OXIDE EMBEDDED POLYMERIC NANOFIBERS FOR THERMO-RESPONSIVE DRUG DELIVERY SYSTEMS

by

Tugay Sancar

B.S., Chemistry, Boğaziçi University, 2020

Submitted to the Institute for Graduate Studies in
Science and Engineering in partial fulfillment of
the requirements for the degree of
Master of Science

Graduate Program in Chemistry
Boğaziçi University

2022

ACKNOWLEDGEMENTS

First of all, I would like to express my sincere thanks to thesis supervisor Prof. Amitav Sanyal and co-advisor Prof. Rana Sanyal for continued support, motivating guidance, kind interest, constructive feedback, and giving me the chance to improve and show myself throughout my undergraduate years till the last day of the thesis year. I appreciate their encouraging attention, valuable opportunities for me and all the members of our research group to grow, and impressive approach to research and science.

I also would like to thank my jury member Prof. Ufuk Saim Günay, for his precious revisions and time in reviewing my thesis.

I would like to express my deepest gratitude to Ismail Altınbaşak. He tirelessly answered each question all along my undergraduate years. His innovative mentorship and priceless company helped me throughout my life. His invaluable assistance and brilliant, skillful supervision enriched this study even further than my expectations.

I also would like to thank Ali Rıza Ülker for helping me with the characterization studies. His endless support and kind friendship always motivated me.

I wish to thank Nazlı Taylan for her heavenly company. Her characteristics always impressed me to be encouraged.

Financial support from Bogaziçi University Research Grant (Project Number 18482, Boun code 21BP7) is gratefully acknowledged.

ABSTRACT

REDUCED GRAPHENE OXIDE EMBEDDED POLYMERIC NANOFIBERS FOR THERMO-RESPONSIVE DRUG DELIVERY SYSTEMS

In recent years, nanofibers have become popular in biomedical applications because of their distinctive qualities, such as the large surface area to volume ratio, porosity, and appreciable mechanical strength. Electrospinning is the most widely utilized method to manufacture nanofibers due to its straightforward setup and cost-effective production. Fabricated nanofibers can be modified with different functional groups to impart characteristic properties and enable their application. In recent years, ‘click’ chemistry transformations have been preferred to functionalize nanofibers.

In this thesis, clickable copolymers were synthesized to generate furan functionalized polymeric nanofibers with the help of electrospinning. Morphological features of the produced nanofibers were characterized with SEM. Reduced graphene oxide (r-GO) was embedded into the nanofiber during electrospinning to provide a photothermal property to the fibrous material. Irradiation of r-GO-containing materials with near-infrared (NIR) light results in the conversion of the light into heat and increases the temperature of the surface of the fibrous substrate. Doxorubicin (DOX) was modified with a maleimide functional group to enable Diels-Alder (DA) cycloaddition between furan-functionalized nanofibers and maleimide-modified drug molecules. After successfully conjugating the drug molecule, exposing drug conjugated nanofiber to NIR light leads to retro Diels-Alder (rDA) reaction resulting in drug release thanks to rapid light-to-heat conversion.

ÖZET

TERMO-DUYARLI İLAÇ TAŞIMA SİSTEMLERİ İÇİN AZALTILMIŞ GRAFEN OKSİT GÖMÜLÜ POLİMERİK NANOLİFLER

Son yıllarda nanolifler, geniş yüzey alanı/hacim oranı, gözeneklilik ve kayda değer mekanik mukavemet gibi ayırt edici nitelikleri nedeniyle biyomedikal uygulamalarda popüler hale gelmiştir. Elektrospinning, basit kurulumu ve uygun maliyetli üretimi nedeniyle nanolifleri üretmek için en yaygın kullanılan yöntemdir. Üretilen nanolifler, karakteristik özellikler kazandırmak ve uygulamalarını sağlamak için farklı fonksiyonel gruplarla modifiye edilebilir. Son yıllarda nanolifleri işlevsel hale getirmek için 'klik' kimya dönüşümleri tercih edilmiştir.

Bu tezde, elektrospinning yardımıyla furan fonksiyonelleştirilmiş polimerik nanolifler üretmek için tıklanabilir kopolimerler sentezlendi. Üretilen nanoliflerin morfolojik özellikleri SEM ile karakterize edilmiştir. İndirgenmiş grafen oksit (r-GO), elyaflı malzemeye fototermal bir özellik sağlamak için elektro-eğirme sırasında nano elyafın içine gömüldü. r-GO içeren malzemelerin yakın kızılötesi (NIR) ışıkla ışınlanması, ışığın ısıya dönüştürülmesiyle sonuçlanır ve lifli substratın yüzeyinin sıcaklığını arttırır. Doksorubisin (DOX), furan-fonksiyonelleştirilmiş nanolifler ve maleimid-modifiye ilaç molekülleri arasında Diels-Alder (DA) eklenmesini sağlamak için bir maleimid fonksiyonel grubu ile modifiye edildi. İlaç molekülünün başarılı bir şekilde konjuge edilmesinden sonra, ilaç konjuge nanofiberin NIR ışığına maruz bırakılması, retro Diels-Alder (rDA) reaksiyonuna yol açar ve hızlı ışık-ısı dönüşümü sayesinde ilaç salınımı ile sonuçlanır.

TABLE OF CONTENTS

ACKNOWLEDGEMENTS iii
ABSTRACT iv
ÖZET v
TABLE OF CONTENTS vi
LIST OF FIGURES viii
LIST OF ACRONYMS/ABBREVIATIONS xiv
1. INTRODUCTION 1
1.1. Nanofibers 1
1.2. Electrospinning Technique 2
1.3. Electrospinning Parameters 5
1.3.1. Solution Parameters 5
1.3.2. Ambient Parameters 10
1.4. Applications of Electrospun Nanofibers 11
1.5. Stimuli-Responsive Nanofibers 17
1.6. Reduced Graphene Oxide (r-GO) 21
1.7. Near-Infrared Laser (NIR) Activation 22
1.8. Click Chemistry as A Tool for Functionalization 24
1.8.1. Diels-Alder Reaction 24
2. AIM OF THE STUDY 27
3. EXPERIMENTAL 28
3.1.1. Materials 28
3.1.2. Instrumentation 28
3.1.3. Synthesis of Furan Containing Copolymers 29
3.1.4. Preparation of r-GO-PFMA-PMMA 29
3.1.5. Preparation of r-GO-PMMA 29
3.1.6. Electrospinning of r-GO-PFMA-PMMA-Copolymer 29
3.1.7. Electrospinning of r-GO-PMMA 30
3.1.8. Fluorescent Dye Conjugation on r-GO-PFMA-PMMA-NFs 30

3.1.9. Release of Chemically Bonded F-Mal from r-GO-PFMA-PMMA-NFs 30
3.1.10. Synthesis of Furan Protected Maleic Anhydride (FuMa) 31
3.1.11. Synthesis of Furan Protected Maleimide Acid (FuMa-Acid) 31
3.1.12. Synthesis of Maleimide Acid (Mal-Acid).....31
3.1.13. Synthesis of Maleimide-NHS (Mal-NHS) 32
3.1.14. Synthesis of Doxorubicin-Maleimide (DOX-Mal) 32
3.1.15. Conjugation of DOX-Mal to r-GO-PFMA-PMMA-NFs.....33
3.1.16. Release of DOX-Mal from r-GO-PFMA-PMMA-NFs.....33
4. RESULTS and DISCUSSION 34
4.1.1. Synthesis and Characterization of PFMA-PMMA Copolymer.....34
4.1.2. Fabrication and Characterization of PFMA-PMMA-NFs.....36
4.1.3. Functionalization of PFMA-PMMA-NFs 38
4.1.4. Drug Modification and Characterization.....43
4.1.5. DOX-Mal Conjugation to r-GO-PFMA-PMMA-NFs and Characterization 47
4.1.6. Photothermally Triggered Release of Chemically Bonded DOX-Mal 48
5. CONCLUSION 50
REFERENCES 51
APPENDIX: COPYRIGHT NOTICES.....63

LIST OF FIGURES

Figure 1.1. Depicted comparative diameters of a human red blood cell and single human hair with a diameter of electrospun nanofibers [11]..... 2

Figure 1.2. Schematic illustration of Taylor Cone formation [12]. 3

Figure 1.3. Schematic illustration of a traditional electrospinning setup [14] 4

Figure 1.4. Schematic illustration of different types of electrospinning spinnerets [15]. 5

Figure 1.5. SEM images of polystyrene polymer-based nanofibers upon increasing concentration since other parameters are constant [17]. 6

Figure 1.6. Photography of polymeric nanofibers produced from different molecular weights where a) 9000–10,000 g/mol, b) 13,000–23,000 g/mol and c) 31,000–50,000 g/mol (solution concentration: 25 wt. %) [18]. 6

Figure 1.7. SEM images of 20 weight percent of PVAc nanofibers at different voltages on the left and on the right, the average diameter of electrospun nanofiber [19]. 7

Figure 1.8. SEM images of PVDF nanofibers with the increase in distance between collector and the tip of spinneret: a) 18cm, b) 20 cm, c) 22 cm, and d) 24 cm [21]. 8

Figure 1.9. SEM images of Nylon 6 nanofibers upon increase in flow rate where (a) 0.1mL/hr, (b) 0.5 mL/hr, (c) 1 mL/hr, (d) 1.5 mL/hr [20]. 9

Figure 1.10. Different types of collectors used in electrospinning which are a) solid collector, b) guide wires collector, c) rotating mandrel, d) rotating wire drum, e) rotating disk f) liquid bath collector [24]..... 10

Figure 1.11. SEM images of cellulose acetate-based polymeric nanofibers under different atmospheric conditions; temperatures and humidity [26] 11

Figure 1.12. Different applications of electrospun nanofibers in a variety of fields; textiles, electrical, sensors, energy storage, filtration, bio-medical [28].... 12

Figure 1.13. Representative wound healing process via multifunctional Janus electrospun nanofiber dressing [32]. 13

Figure 1.14. Representative filtration process through electreted PSA/PAN-B-based electrospun mats [37]. 14

Figure 1.15. Representative summary of biosensing of ZIKV Virus via electrospun crosslinked nanofiber mats [41]. 15

Figure 1.16. Schematic synthesis and manufacturing of dendrimer-based, brimonidine tartrate (BT) polymeric electrospun nanofibers for administering antiglaucoma [48]..... 16

Figure 1.17. Depicted scheme for fabrication of a woven electrospun scaffold and extraction of α-mangostin for cardiac patch applications [50]. 17

Figure 1.18. Scheme for how cellulose-based nanofibers (CNF-PEI) upon a change in a narrow pH range for antibacterial response [57]. 18

Figure 1.19. a) Representative scheme for NIR light initiated drug delivery system using PVA electrospun nanofibers with photocleavable polymer prodrug and water-dispersible UCNPs, b) Scheme for the structure of levofloxacin-conjugated PEG-photocleavable molecule.[60]. 19

Figure 1.20. General scheme for fabrication and applications of photo-thermally triggered nanofibers [8]. 20

Figure 1.21. a) Scheme for the chemical structure of graphene, graphene oxide, and reduced graphene oxide; b) Schematic route for reduction of graphite to reduced graphene oxide [69]. 21

Figure 1.22. Illustration of the depth to which wavelengths penetrate human skin [74]. 23

Figure 1.23. Diels-Alder cycloaddition reaction of furan and maleimide and reversibility of their endo-exo-cycloadducts [81]. 25

Figure 1.24. Biotin functionalized furan containing nanofibers attained through DA reaction and their fluorescence microscopy images [87]. 26

Figure 2.1. Depicted scheme of the aim of the project. 27

Figure 4.1. Schematic representation of the free radical polymerization to synthesize furan functionalized copolymer. 34

Figure 4.2. ^{1}H-NMR spectrum of PFMA-PMMA copolymer. 35

Figure 4.3. ^{13}C-NMR spectrum of PFMA-PMMA copolymer. 35

Figure 4.4. GPC trace of PFMA-PMMA copolymer. 36

Figure 4.5. On the left; a piece of PFMA-PMMA nanofibrous mat, on the right; SEM image of the manufactured nanofiber. 36

Figure 4.6. SEM images of the fabricated nanofibers at different concentrations; a) 275, b) 250, and c) 225 μL DMF, histogram results belonging to d) 275 e) 250 f) 225 μL DMF. 37

Figure 4.7. a) Schematic presentation of the preparation of r-GO-PFMA-PMMA polymer solution before applying electrospinning, b) Digital image of r-GO-PFMA-PMMA-NFs. 38

Figure 4.8. Temperature vs. time graph of the r-GO (1% w/w) containing functional nanofibrous mat under different beam powers..... 39

Figure 4.9. Schematic scheme for conjugation of F-Mal to r-GO-PFMA-PMMA-NFs. 40

Figure 4.10. Fluorescence microscopy images of functional nanofibers (r-GO-PFMA-PMMA); a) after activation via NIR laser irradiation with 5, 10, 15, 30, and 45 min. pulses; b) after passive release at 37 °C within the same time interval, c) non-functional nanofibers (r-GO-PMMA-NFs) UV spectra of F-Mal; d) after exposure to NIR laser, e) at 60 °C. 41

Figure 4.11. a) Reaction scheme for loading and photothermal release of E-Mal, b) Release profile of photothermally stimulated E-Mal from r-GO-PFMA-PMMA-NFs vs. non-triggered r-GO-PFMA-PMMA-NFs. 42

Figure 4.12. ^{1}H-NMR spectrum of FuMa cycloadduct. 43

Figure 4.13. ^{1}H-NMR spectrum of FuMa-Acid. 44

Figure 4.14. ^{1}H-NMR spectrum of Ma-Acid..... 44

Figure 4.15. ^{1}H-NMR spectrum of Mal-NHS linker. 45

Figure 4.16. ^{1}H-NMR spectrum of a) DOX•HCl, b) DOX-Mal..... 46

Figure 4.17. Mass spectra of DOX-Mal. 46

Figure 4.18. SEM images of r-GO-PFMA-PMMA-NFs after and before DOX-Mal loading, respectively. 47

Figure 4.19. Schematic illustration of DOX-Mal loading to r-GO-PMMA-NFs and r-GO-PFMA-PMMA-NFs, respectively. 48

Figure 4.20. The release profile of DOX-Mal upon on-off irradiation with NIR light. . 49

Figure A.1. Copyright for Figure 1.1. 63

Figure A.2. Copyright for Figure 1.2. 63

Figure A.3. Copyright for Figure 1.3. 63

Figure A.4. Copyright for Figure 1.4. 64

Figure A.5. Copyright for Figure 1.5. 64

Figure A.6. Copyright for Figure 1.6. 65

Figure A.7. Copyright for Figure 1.7. 65

Figure A.8. Copyright for Figure 1.8. 65

Figure A.9. Copyright for Figure 1.9. 66

Figure A.10. Copyright for Figure 1.10. 66

Figure A.11. Copyright for Figure 1.11. 66

Figure A.12. Copyright for Figure 1.12. 67

Figure A.13. Copyright for Figure 1.13. 67

Figure A.14. Copyright for Figure 1.14. 68

Figure A.15. Copyright for Figure 1.15. 68

Figure A.16. Copyright for Figure 1.16. 69

Figure A.17. Copyright for Figure 1.17. 69

Figure A.18. Copyright for Figure 1.18. 70

Figure A.19. Copyright for Figure 1.19. 70

Figure A.20. Copyright for Figure 1.20. 71

Figure A.21. Copyright for Figure 1.21. 71

Figure A.22. Copyright for Figure 1.22. 71

Figure A.23. Copyright for Figure 1.23. 72

Figure A.24. Copyright for Figure 1.24. 72

LIST OF ACRONYMS/ABBREVIATIONS

3D	3 dimensional
AIBN	2,2′-Azobis(2-methylpropionitrile)
Al_2O_3	Aliminum Oxide
$CDCl_3$	Chloroform
CH_2Cl_2	Dichloromethane
DA	Diels-Alder
DCC	N,N′-Dicyclohexylcarbodiimide
DCU	Dicyclohexylurea
DIPEA	N,N-Diisopropylethylamine
DMAP	4-(Dimethylamino)pyridine
DMF	Dimethylformamide
DOX	Doxorubicin
DOX•HCl	Doxorubicin hydrochloride
DOX-Mal	Maleimide conjugated doxorubicin
E-Mal	N-Ethyl Maleimide
EtOAc	Ethyl acetate
EtOH	Ethanol
F-Mal	N-(5-Fluoresceinyl)maleimide
FMA	Furfuryl methacrylate
FuMa	Furan protected maleic anhydride
FuMa-Acid	Furan protected maleimide acid
GPC	Gel Permeation Chromatography
GO	Graphene oxide
LC-MS	Liquid Chromotography-Mass Spectrescopy
Ma-Acid	4-Maleimidobutyric acid
Mal-NHS	4-Maleimidobutyric acid N-hydroxysuccinimide ester
MeOH	Methanol
MMA	Methyl Methacrylate
Na_2SO_4	Sodium sulfate

NF	Nanofiber
NHS	N-Hydroxysuccinimide
NMR	Nuclear Magnetic Resonance
NIR	Near-Infrared
PBS	Phosphate Buffer Saline
rDA	retro Diels-Alder
r-GO	Reduced Graphene Oxide
rpm	Revolutions per Minute
rt	Room Temperature
SEM	Scanning Electron Microscopy
THF	Tetrahydrofuran
TLC	Thin Layer Chromotography
UV	Ultraviolet
w/w	Weight per weight

1. INTRODUCTION

1.1. Nanofibers

Nanofibers are a unique class of bulk fibrous nanomaterials where the diameters of the fibers range from a few nanometers to a micron scale. These materials offer a tremendous surface-to-volume ratio compared to other bulk materials such as hydrogels, polymeric films, and microfibers. The high surface area provides a high degree of reactive space to encapsulate and/or conjugate bioactive molecules such as drugs, proteins, and growth factors for sensing [1], drug delivery [2], and tissue engineering [3] applications. Additionally, the choice of polymer utilized in the fabrication of nanofibers brings various other properties such as stiffness, porosity, and hydrophilicity. This freedom in the design of nanofibers has attracted considerable attention to these materials in recent years

Researchers have developed several techniques to fabricate nanofibrous mats to meet the increased demand for such materials, such as template synthesis [4], phase separation [5], self-assembly [6], drawing [7], and electrospinning [8]. The manufacturing techniques of ultrafine polymeric nanofibers can be categorized into two major groups: electrospinning and non-electrospinning methods. In the electrospinning method, the manufacturing of the polymeric nanofibers is based on electrical forces [9], while non-electrospinning techniques are based on mechanical forces [10].

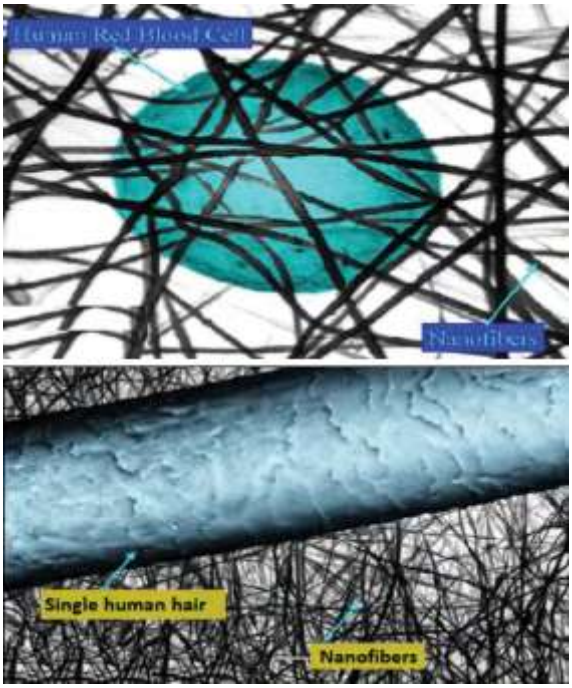

Figure 1.1. Depicted comparative diameters of a human red blood cell and single human hair with a diameter of electrospun nanofibers [11].

1.2. Electrospinning Technique

It has been known for over a century that electrostatic forces can be used to manufacture synthetic filaments. Namely, electrospinning is the process of producing of fibers under electrostatic forces. Electrospinning controls the morphological features of manufactured nanofibers, such as diameter and pattern. Fundamentally, electrospinning utilizes a high-voltage electric field to create electrically charged jets from polymer solutions or melts, which dry into nanofibers as the solvent is evaporated. The first patent related to the electrospinning process was obtained by Formhals, who reported electrospinning of cellulose acetate in the existence of acetone and monomethyl ether of ethylene glycol as solvents. In the late 1960s, Taylor studied jet formation during the electrospinning process and determined the geometry of the polymer droplet formed at the end of the needle's tip as an electric field is applied. Taylor defined the droplet's shape as a cone where the jets are released from the vertices of the cone. In the following studies, the conical shape has been called 'Taylor Cone' as the essential feature of the electrospinning process (Figure 1.2).

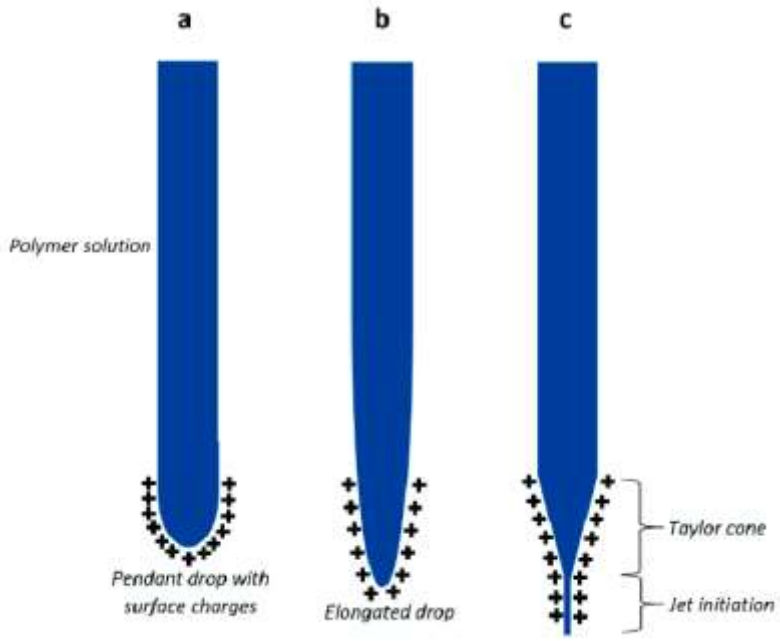

Figure 1.2. Schematic illustration of Taylor Cone formation [12].

A basic electrospinning setup involves a high voltage power source that consists of positively and negatively polarized electrodes (Figure 1.3). The setup also involves a syringe pump which could be placed either vertically or horizontally to transfer polymeric solutions through the spinneret onto a metal plate collector. The collector can be designed depending on the needs, such as a flat and rotating drum [13]. During the electrospinning progress, an electric field is applied to a polymer solution at the end of the spinneret to inject a charge that has a polarity. Afterward, the surface of the charged droplet transforms into the shape of a cone, described as the Taylor Cone.

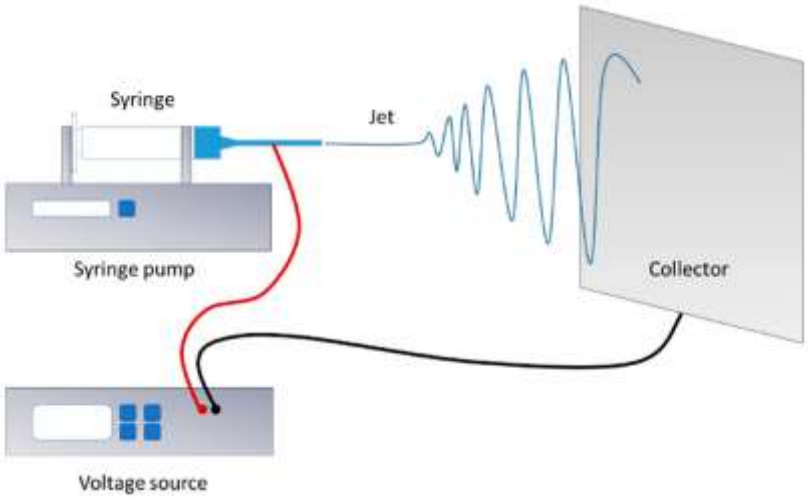

Figure 1.3. Schematic illustration of a traditional electrospinning setup [14]

Whenever the electrostatic forces generated via applied high voltages overcome the surface tension of the polymer solution droplet at the end of the needle's tip, charged jet begins to elongate and move towards the opposite electrode (metal collector). As a result, the elongated jet starts depositing on the collector. During the travel of a charged jet between the oppositely charged electrodes, the solvent evaporates, and nanofibers form.

The polymeric nanofibers can be produced using a solution with milliliter volumes on laboratory scales. In contrast, most of the industrial mass production of nanofibers can be supplied by continuous electrospinning of polymer solutions up to several liters. A conventional electrospinning setup generally has one spinneret to work on the laboratory scale. However, simply modifying via another spinneret (multi-spinneret) can enhance the total mass of polymeric nanofiber deposited on the collector. Inserted multi-spinnerets into an electrospinning setup can be placed in uniaxial or circular geometry [15]. In addition to increasing overall mass product, the thickness of manufactured nanofibers and deposition region is also enhanced thanks to utilizing multi-spinnerets. That's why electrospinning can be applied on two distinct immiscible polymer solutions inside separated spinnerets to attain composite nanofibers [15].

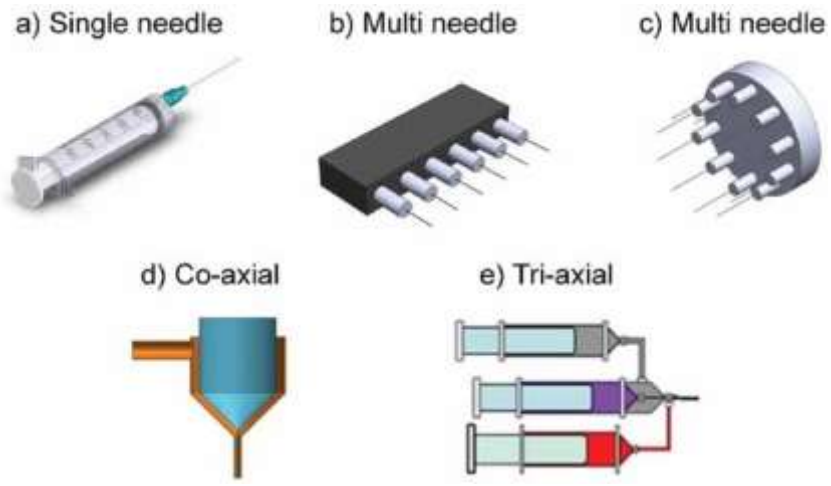

Figure 1.4. Schematic illustration of different types of electrospinning spinnerets [15].

1.3. Electrospinning Parameters

Since electrospinning is a versatile method to manufacture polymeric nanofibers on a lab scale and an industrial scale, the working parameters of the electrospinning process become crucial. Structural morphology of electrospun nanofibers that are diameter and arrangement of fibers can be controlled by altering the parameters like solution parameters, processing parameters, and ambient parameters [16].

1.3.1. Solution Parameters

Appropriate solution concentration of the polymer and molecular weight of the polymer in the electrospinning can be counted as ones of necessity to firstly be set before initiating an electrospinning process. Due to low polymer solution concentration, micro or nano-sized particles would be formed. That's why it is very likely to spectate electrospray instead of electrospinning at this moment. In addition, beads and nanofibers mixture were obtained with a slightly higher concentration. Even if the concentration of the solution has been further increased, almost bead-free or micron-scale nanofibers can be obtained [17]. As a literature example, SEM images of the nanofibers have indicated how the concentration affects the structural morphology of nanofibers (Figure 1.5).

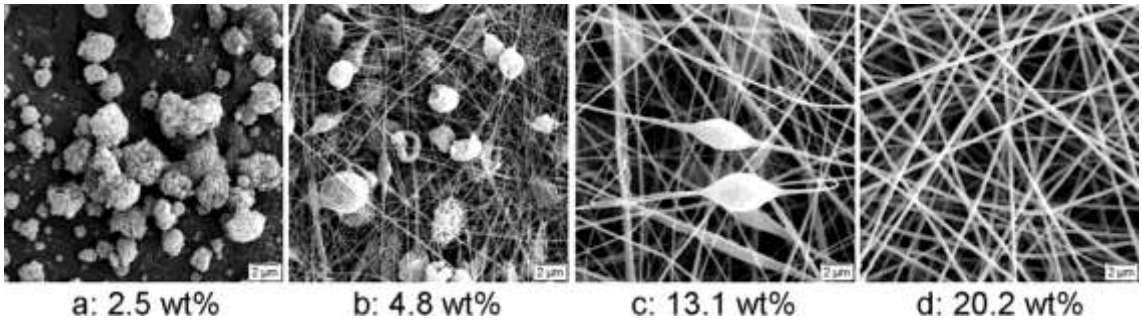

Figure 1.5. SEM images of polystyrene polymer-based nanofibers upon increasing concentration since other parameters are constant [17].

The molecular weight of the polymer also has a direct relationship with the viscosity of the polymer solution since molecular weight dictates the entanglements of polymer chains. Mostly, nanofiber formation is easier with the higher molecular weight polymers due to the high viscosity resistance, whereas the lower molecular weight causes a low polymer solution concentration. One of the literature examples of how molecular weight affects the morphological structure of nanofibers is shown by S. Shivkumar and his coworkers [18]. In this study, they exhibited a decrease in the number of beads and an increase in the diameter of the nanofibers upon increasing entanglements (Figure 1.6).

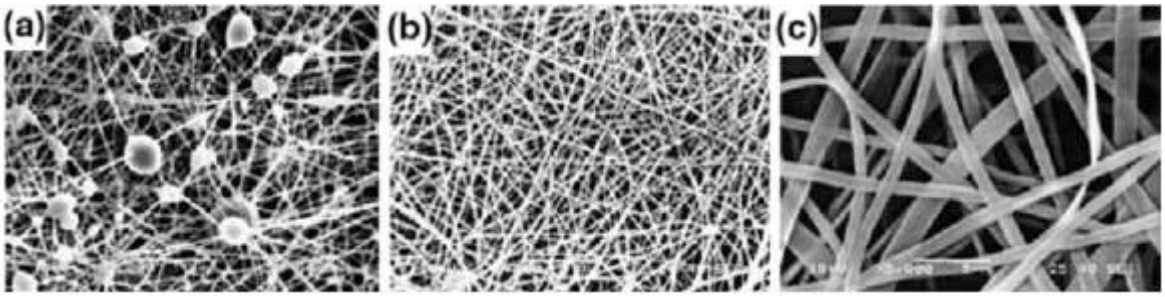

Figure 1.6. Photography of polymeric nanofibers produced from different molecular weights where a) 9000–10,000 g/mol, b) 13,000–23,000 g/mol and c) 31,000–50,000 g/mol (solution concentration: 25 wt. %) [18].

In addition to solution parameters, four other processing factors are directly related to the electrospinning process; applied voltage, the distance between the collector and the end of the needle's tip, type of collector, and flow rate of the polymer solution.

Supplying enough voltage to the system to generate charges on the polymer solution is highly important for manufacturing proper nanofibers. Mostly, the diameter of the formed nanofibers is related to the applied voltage. The structural morphology of electrospun polyvinyl acetate (PVAc) has been examined with changing various processing parameters [19]. This study has demonstrated that an increase in the applied voltage has ended up with an increase in the average diameter of fiber (Figure 1.7).

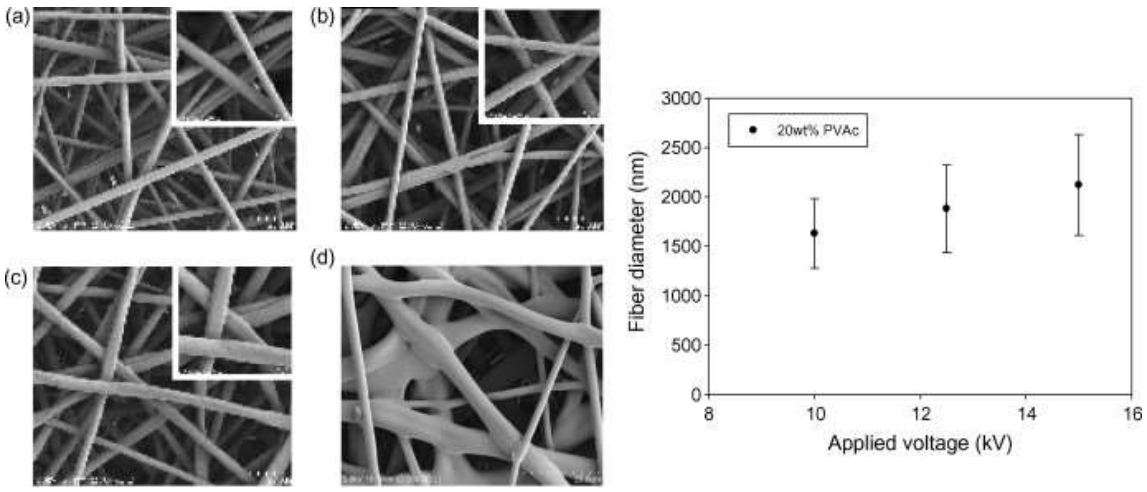

Figure 1.7. SEM images of 20 weight percent of PVAc nanofibers at different voltages on the left and on the right, the average diameter of electrospun nanofiber [19].

Another crucial processing parameter that directly impacts the morphology and diameter of the electrospun nanofiber is the distance between the collector and the end of the needle tip. The distance should be selected carefully to have sufficient flight time for solvent evaporation before reaching the collector. Fiber fibers with beads or smaller diameters can most likely be observed whenever the distance becomes greater than the optimum distance. Thus, providing ideal distance has great significance in terms of morphological perspective, particularly giving enough time to dryness of the formed nanofiber after leaving the tip of the spinneret. One of the literature examples has exhibited that the average diameter value of PVDF nanofibers becomes smaller with an increase in the distance (Figure 1.8) [20].

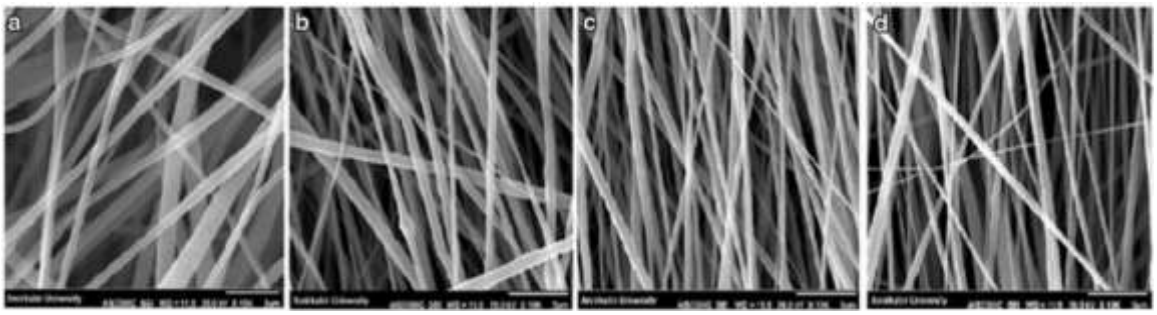

Figure 1.8. SEM images of PVDF nanofibers with the increase in distance between collector and the tip of spinneret: a) 18cm, b) 20 cm, c) 22 cm, and d) 24 cm [21].

The pump rate (flow rate) of the polymer solution in the syringe is also an essential processing parameter. In general, feed rate controls the flight time of the polymer solution between polarized electrodes. That's why the time required for solvent evaporation can be controlled via flow rate. In other words, the optimum flow rate has to be defined and provided through the electrospinning system. Higher flow rates lead to the formation of thick diameter, and if the flow rate becomes larger than the optimum high flow rate, bead formations can be observed, whereas if the flow rate is set to a low flow rate, thinner nanofibers can be observed. For example, Shamim Zargham and his coworkers have demonstrated the effect of flow rate on the structural morphology of Nylon 6 electrospun nanofibers [20]. SEM analysis clearly showed bead formation upon increasing flow rate, and also fewer defects on nanofibers were observed (Figure 1.9).

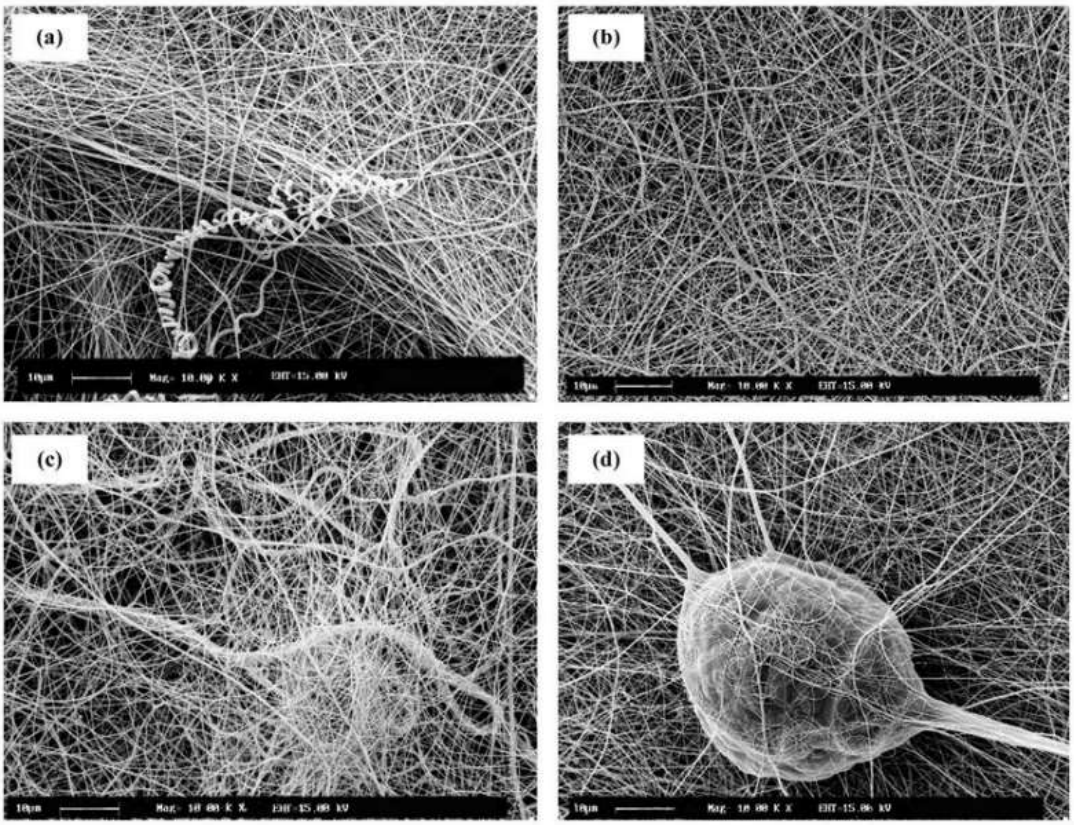

Figure 1.9. SEM images of Nylon 6 nanofibers upon increase in flow rate where (a) 0.1mL/hr, (b) 0.5 mL/hr, (c) 1 mL/hr, (d) 1.5 mL/hr [20].

Since the grounded collectors behave as conductive substrates in the electrospinning, they are all used for collecting produced nanofibers. In most cases, the collector has covered with aluminum foil as a conductive surface. It is a fact that handling the collected nanofibers for various purposes could be challenging. In order to overcome this difficulty, different types of collectors have been developed by researchers like wire mesh [22], pin [23], rotated bar, disk or grid, and wire collector. It is critical to emphasize that the properties of the electric field generated in the have affected nanofibers structural morphology and distribution. Various receiving devices can be used to get randomly distributed fibers, patterned fibers, organized fibers, and three-dimensional structure fibers [24] For example; fibers are usually randomly oriented when employing a grounded solid collector [25]. To produce aligned nanofibers, a rotating collector (rotating wire drum, rotating mandrel, rotating disk (Figure 1.10) with adjustable rotation speed is required [24].

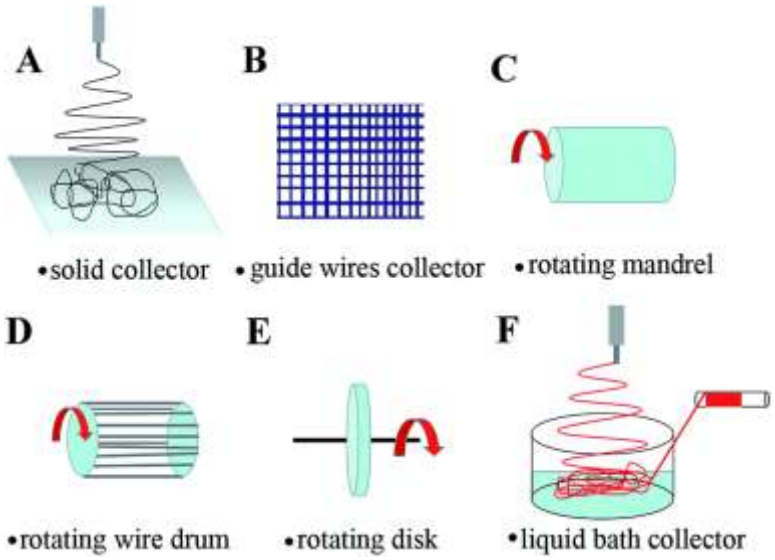

Figure 1.10. Different types of collectors used in electrospinning which are a) solid collector, b) guide wires collector, c) rotating mandrel, d) rotating wire drum, e) rotating disk f) liquid bath collector [24].

1.3.2. Ambient Parameters

In addition, morphological control over synthetic polymeric nanofiber can be affected by changes in environmental conditions such as temperature and humidity. G Bracewell and coworkers have demonstrated the impacts of controlled ambient parameters on cellulose acetate (CA) nanofibers [26]. Their study has deduced that the produced fiber's diameter is directly proportional to the ambient humidity since the evaporation rate of the solvent has increased under low humidity conditions. On the other hand, an increase in the humidity level has caused the wet deposition of nanofibers on the collector. Furthermore, the findings revealed that when the temperature rises, the diameter of the fibers reduces (Figure 1.11). They claim this phenomenon is related to the viscosity change due to high temperature.

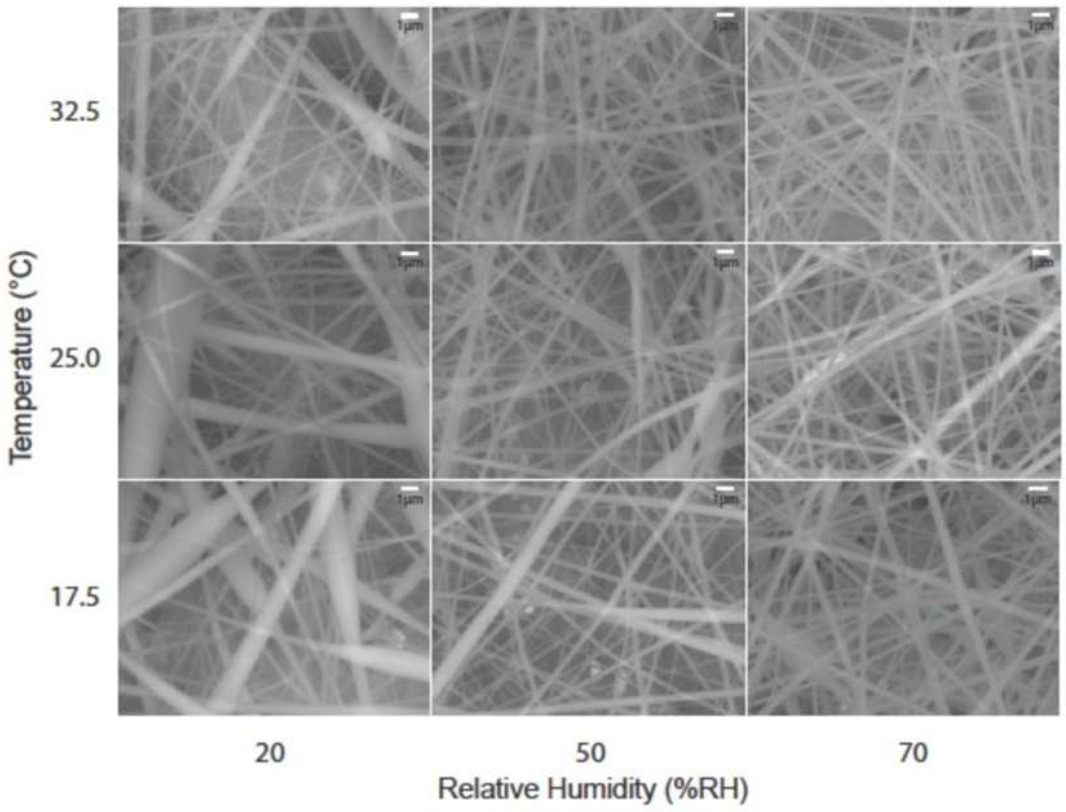

Figure 1.11. SEM images of cellulose acetate-based polymeric nanofibers under different atmospheric conditions; temperatures and humidity [26]

1.4. Applications of Electrospun Nanofibers

Electrospinning is a valuable and convenient method for producing ultrathin fibers. This technique has been used in different applications due to its simple fabrication process. These application areas involve filtration, controlled release, bio-sensing, self-cleaning, tissue engineering, self-healing, filtration, affinity membrane, protective clothing, solar cells, immobilization of enzymes, energy storage, and drug delivery, among others (Figure 1.12). As compared with the other applications, electrospun nanofibers are particularly well-suited to biomedical applications.

Several polymers have been successfully evaluated for electrospinning, including synthetic and natural polymers. PCL, poly(lactic acid) (PLA), and poly(lactic-co-glycolic acid) (PLGA) are the most common biocompatible and biodegradable synthetic polymers

that have been used as the precursor for electrospinning in biomedical purposes. Natural polymers such as DNA, proteins, nucleic acids, chitosan, collagen, and gelatin, can be attractive materials in the electrospinning process [27].

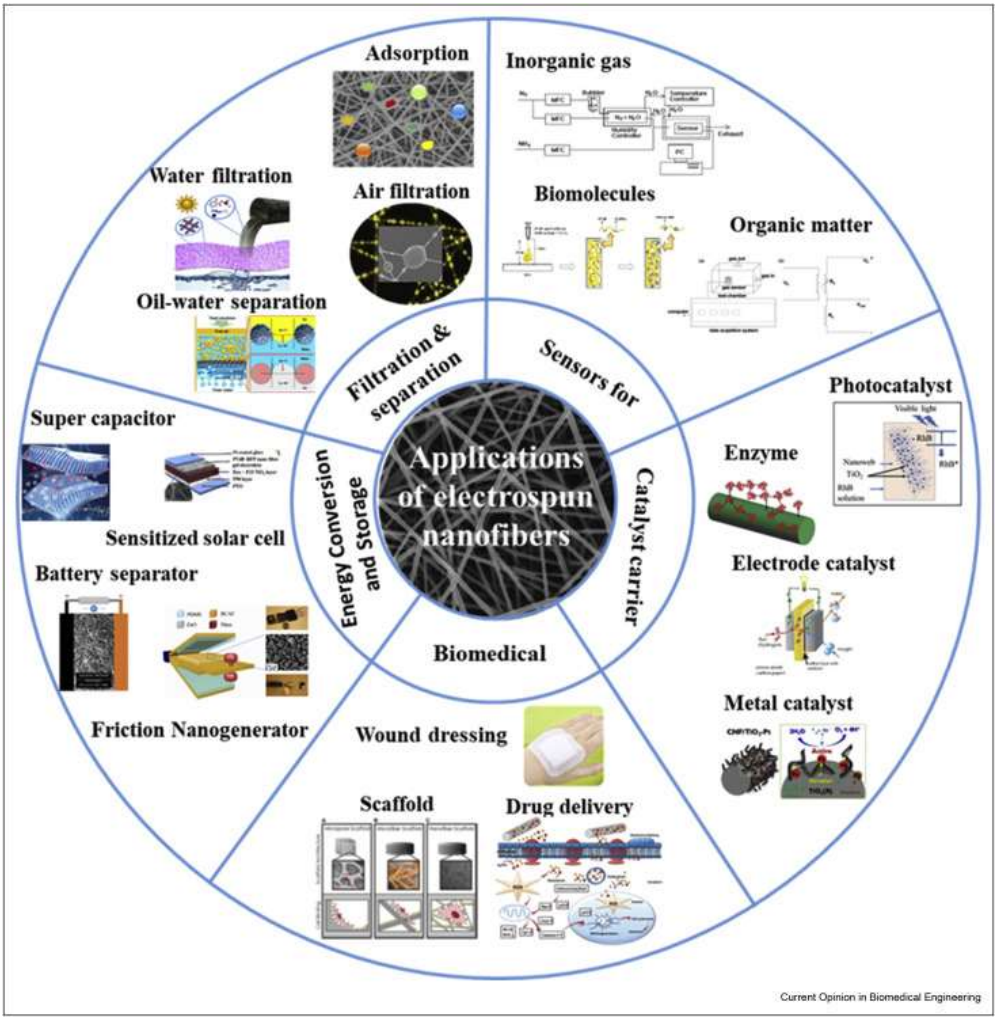

Figure 1.12. Different applications of electrospun nanofibers in a variety of fields; textiles, electrical, sensors, energy storage, filtration, bio-medical [28].

Electrospinning is a comprehensive technique for creating fibrous scaffolds that mimic biological tissue. Recently, these materials attracted much interest in developing bioactive dressing materials for treating chronic and acute wounds [29]. Since it is both economical and easily accessible, dry gauze is now the most often used wound dressing. However, it has significant drawbacks, including a high absorbent capacity that stimulates wound dehydration and promotes bacterial development. Additionally, the removal of these

bandages can be excruciating. At this point, nanofibrous scaffolds made of a wide range of synthetic and natural polymers offer flexibility in the design for suitable chemical and physical properties [30,31]. For example, Qi and coworkers have developed an antibacterial electrospun nanofiber dressing that can drain biofluid [32]. Briefly, they designed an electrospun nanofiber dressing to restrain methicillin-resistant Staphylococcus aureus (MRSA) and to drain unnecessary biofluids (Figure 1.13).

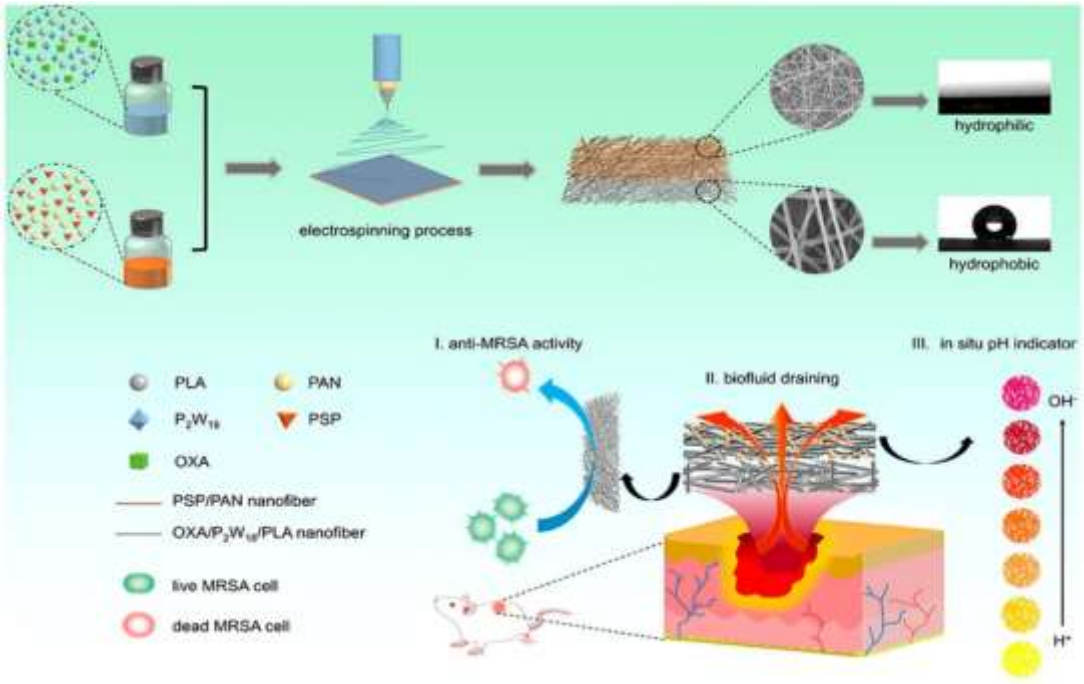

Figure 1.13. Representative wound healing process via multifunctional Janus electrospun nanofiber dressing [32].

As a result of the globalization of industry and urbanization, air pollution has become one of the environmental issues. That's why air filtration materials have attracted great interest recently. However, plenty of air filtration materials present low filtration efficiency compared to their manufacturing cost and pressure drop. Fundamentally, a filter must involve an appropriate porous size that allows successful filtration. At this point, electrospun nanofibrous membranes offer high performance at filtering since they have a high surface area to volume ratio, adjustable porous size, and easy production process [33,34,35,36]. As a particular instance of electrospun nanofiber-based filtration, Yuan and coworkers have developed novel electrospun nanofibers based on electreted

polysulfonamide/polyacrylonitrile-boehmite (PSA/PAN-B) composite, at the same time, high-temperature air filtration for dust removal (Figure 1.14) [37].

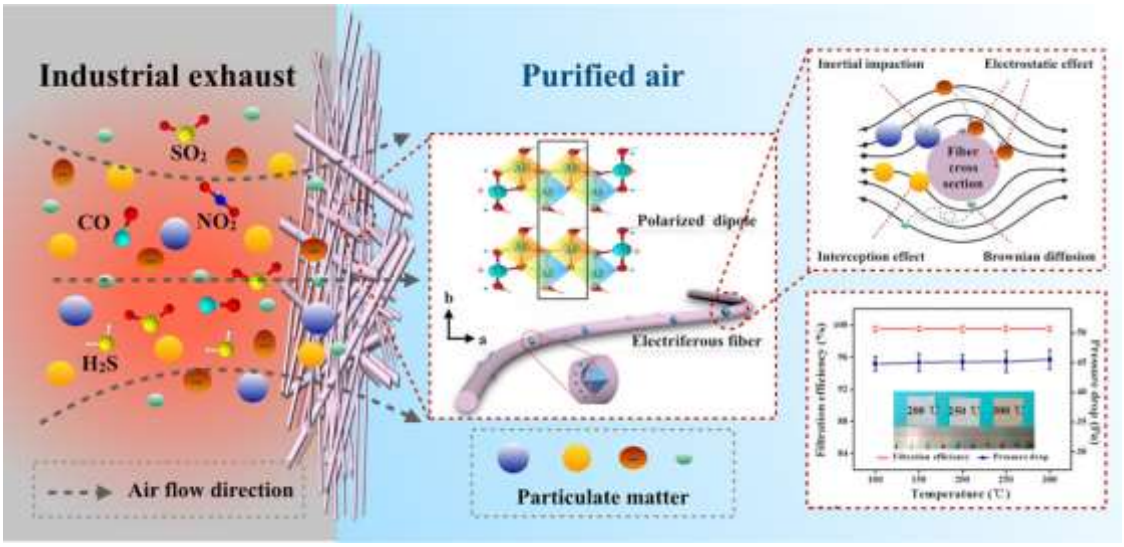

Figure 1.14. Representative filtration process through electreted PSA/PAN-B-based electrospun mats [37].

The polymeric electrospun nanofibers have enabled the investigation of single-molecule or transport of bulk ions through a sensor surface because electrospun nanofibers exhibit the promising feature owing to 3D porous morphology. Additionally, producing nanofibers from biocompatible and biodegradable synthetic or natural polymers, high surface area, and low production cost may be highlighted the importance of their role [38,39,40]. One of the literature example [41] has demonstrated that electrospun nanofiber mats manufactured through electrospinning of biocompatible materials such as alginate and considerably hygroscopic PVA, have been successfully utilized for capturing Zika Virus (Figure 1.15). As a crosslinking agent, glutaraldehyde has been used to enhance the water mat's stability. Functional carboxylic acid groups have been used to tether anti-ZIKV PAbs. Indeed, the mats were employed as a label-free electrochemical transducer for biosensing with a large surface area.

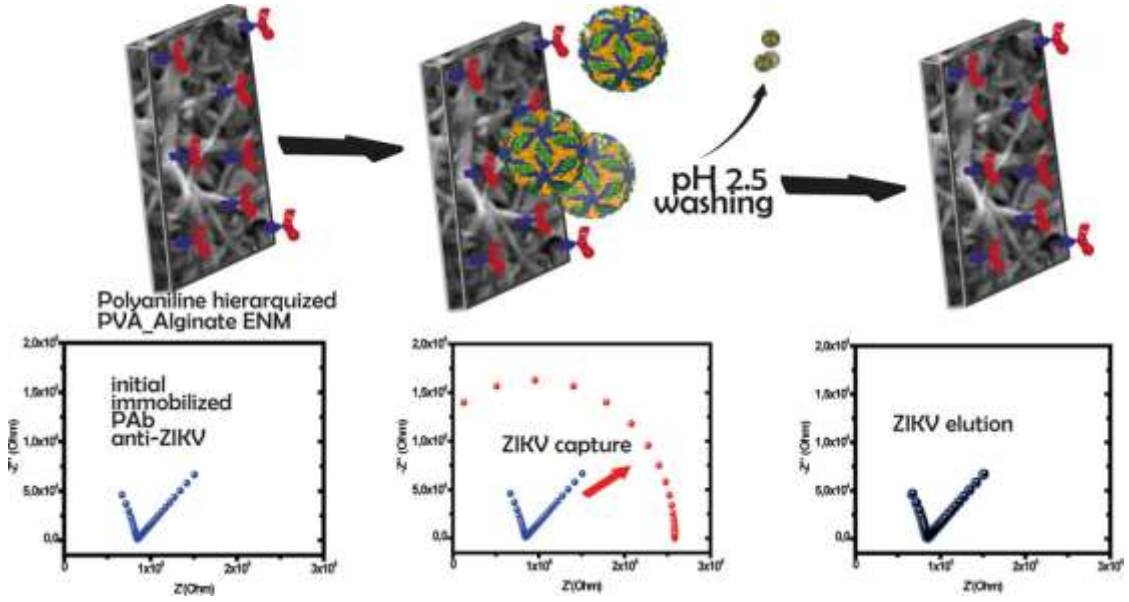

Figure 1.15. Representative summary of biosensing of ZIKV Virus via electrospun crosslinked nanofiber mats [41].

In the last decades, electrospun nanofiber scaffolds have been highlighted as a promising therapeutic platform for drug delivery systems due to their characteristic features such as controllable surface morphology and modification, biocompatibility, and large surface area [8,42,43,44]. Moreover, electrospun nanofiber mats provide enhanced loading capacity. Although natural polymers have gained interest for drug delivery due to their biocompatibility, there are also many examples of nanofiber scaffolds produced from synthetic polymers [45,46]. The corporation of a therapeutic drug or antibiotic can be achieved through either an encapsulation via physical interactions or conjugation via chemical bonding to functionalized polymeric nanofiber [8,47]. For an example of a physically loaded drug into polymeric electrospun nanofibers, Yang and coworkers have designed fast-dissolving dendrimer-based nanofibers which provide a large delivery surface scaffold for anti-glaucoma drug; brimonidine tartrate (Figure 1.16) [48].

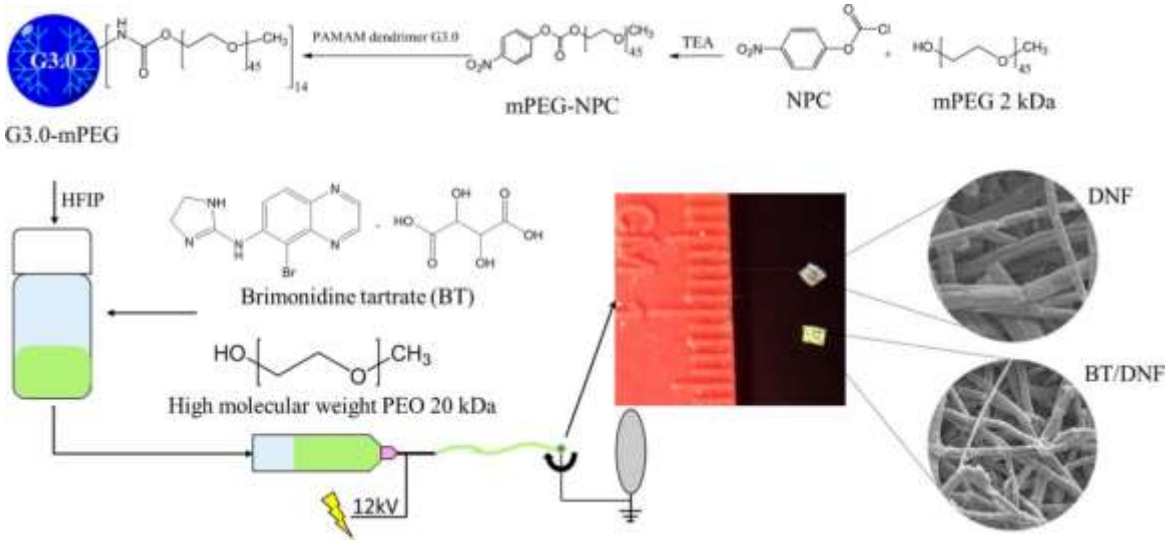

Figure 1.16. Schematic synthesis and manufacturing of dendrimer-based, brimonidine tartrate (BT) polymeric electrospun nanofibers for administering antiglaucoma [48].

In recent years, scaffolds based on electrospun nanofibers have been widely employed in tissue engineering due to their promising features as their tunable nature and superb nanoscale 3D construction while providing outstanding structural rigidity and porosity. Cellular matrixes as a substrate for the delivery of drugs to targeted tissues can be generated through synthetic and natural materials to repair damaged tissues [49]. Such that, in one of the recent studies in cardiac showed that the fabricated woven nanofibrous scaffolds via an ideal network have enhanced angiogenesis and increased tissue compatibility in vivo (Figure 1.17) [50].

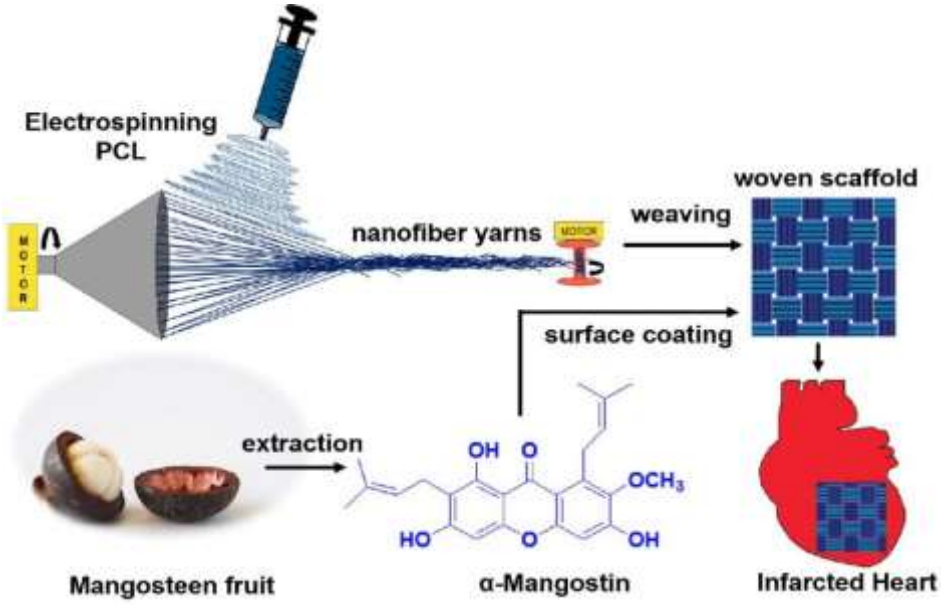

Figure 1.17. Depicted scheme for fabrication of a woven electrospun scaffold and extraction of α-mangostin for cardiac patch applications [50].

1.5. Stimuli-Responsive Nanofibers

Electrospun nanofibers have been empowered with "smart" qualities to make various applications throughout the last decade. Since electrospun nanofibrous materials have been produced using natural or synthetic polymers, stimuli-responsive polymers experience chemical or structural (conformational) alternation upon an external stimulus [27]. Such responsive nanofibers can be triggered in various ways; pH [51,52], temperature [53], light [54], electric field [55]. As the outstanding properties of electrospun nanofibers like having a great surface area to volume ratio, involving high porous structure, and cost-effectiveness in manufacturing have been combined with the stimuli-responsive systems, their applications have been mainly explored in controlled drug release, bio-sensing, self-cleaning and self-healing.

Stimuli-responsive nanofibers have emerged to succeed in drug release at a constant rate over a sustained time interval. In other words, stimuli-responsive nanofibers have been used as characteristic controlled delivery systems that release entrapped contents through different extra- and intracellular biological stimuli [56]. For drug delivery systems, it is

significant to design appropriate variables; size, surface characteristics, chemistry, chemical components, and degradability. That's why various smart responsive materials for drug delivery are designed in response to a stimulus that causes a reversible change in the features of the material structure. Since most of the designed materials are synthetic and non-biodegradable, bio-based (natural) polymer composites have been utilized for manufacturing smart responsive systems. For example, Zhu and his coworkers have designed intelligent cellulose-based nanofibers in order to enable sustained antibacterial and drug release with a pH-responsive mechanism [57]. In this study, they have manufactured pH-sensitive cellulose nanofibers (CNF-PEI), where polyethylenimine (PEI) has been grafted onto TEMPO-oxidized cellulose nanofibers through three different carboxyl groups on the cellulose to enhance biocompatibility (Figure 1.18). Fundamentally, conformational change in the side chains in a restricted pH range has been observed upon protonation and deprotonation of amino groups and also intermolecular physical interactions such as hydrogen bonding. That's why CNF-PEI-based nanofibers have responded to changes in pH by converting wettability properties. Such CNF-PEI nanofibers present hydrophilic and superoleophobic properties under acidic conditions, while hydrophobic and superoleophilic behavior has been observed under alkaline conditions.

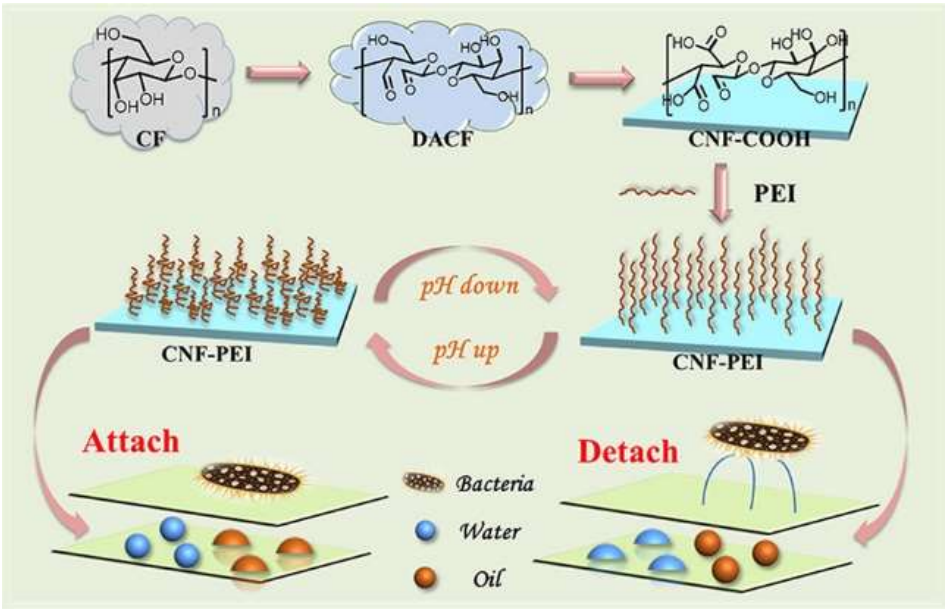

Figure 1.18. Scheme for how cellulose-based nanofibers (CNF-PEI) upon a change in a narrow pH range for antibacterial response [57].

In addition to the pH-responsivity of nanofibers, light is also one of the external stimuli because of its noninvasive nature, controlled localization, and irradiation dose. Ultraviolet (UV) light can be commonly used as an external light stimulus [58]. However, the fact is that exposing human tissues and cells to UV irradiation can damage [59]. When designing a safe wound dressing material, near-infrared (NIR) light can be preferred as stimuli since it shows no damage on human skin, whereas it is not enough to cleave any chemical bond since NIR light has lower energy than UV light. Therefore, Vetrone and his coworkers have utilized lanthanide-doped upconverting nanoparticles (UCNPs) to convert NIR to UV light in order to decrease the impact of UV light on tissues [60]. In their study, a sophisticated platform to manufacture electrospun PVA nanofibers where UCNPs have been embedded as NIR-UV transducers for wound dressing. To improve colloidal stability and dispersibility in the PVA fiber matrix, $LiYbF_4:Tm^{3+}/LiYF_4$ UCNPs were coated with hydrophilic crosslinked polymer. Levofloxacin conjugates as the model drug have chemically conjugated through o-nitrobenzyl (ONB) linkages to poly(ethylene glycol) (PEG) (Figure 1.19). Finally, levofloxacin was released once the ONB linkages in the drug conjugates were broken down by either direct UV irradiation or that caused by the UCNPs after NIR excitation.

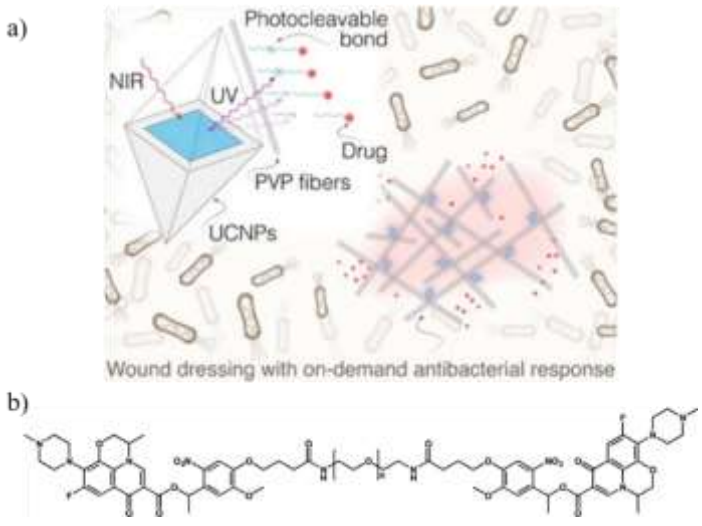

Figure 1.19. a) Representative scheme for NIR light initiated drug delivery system using PVA electrospun nanofibers with photocleavable polymer prodrug and water-dispersible UCNPs, b) Scheme for the structure of levofloxacin-conjugated PEG-photocleavable molecule.[60]

Alteration of temperature among the other modulations of stimuli has unique advancement like behaving and affecting as either internal stimuli for some infections that can be eliminated at high temperatures or external stimuli for generating heat through nanostructures. Thus, certain photothermal active nanofibers can be generated from the participation of gold nanorods [61], carbon nanotubes [62], and carbon nanoparticles [63]. More recently, many articles about the photothermal properties of graphene oxide (GO) embedded nanofibers have been published [64,65,66]. However, few studies exist regarding controlled drug release from reduced graphene oxide (r-GO) containing stimuli-responsive electrospun nanofibers. Specifically, a recent study by Szunerits, Sanyal, and coworkers reported photo-thermally triggered and r-GO embedded polymeric fibrous mats for on-demand release of antibiotics by exposing the mats to near-infrared light (NIR)[8]. In the study, physically loaded or entrapped antibiotic drugs were successfully controlled-released after exposing nanofibrous mat to NIR light thanks to an increase in temperature, ending up enhancing in average kinetic energy of molecules since r-GO converts the absorbed light into heat (Figure 1.20).

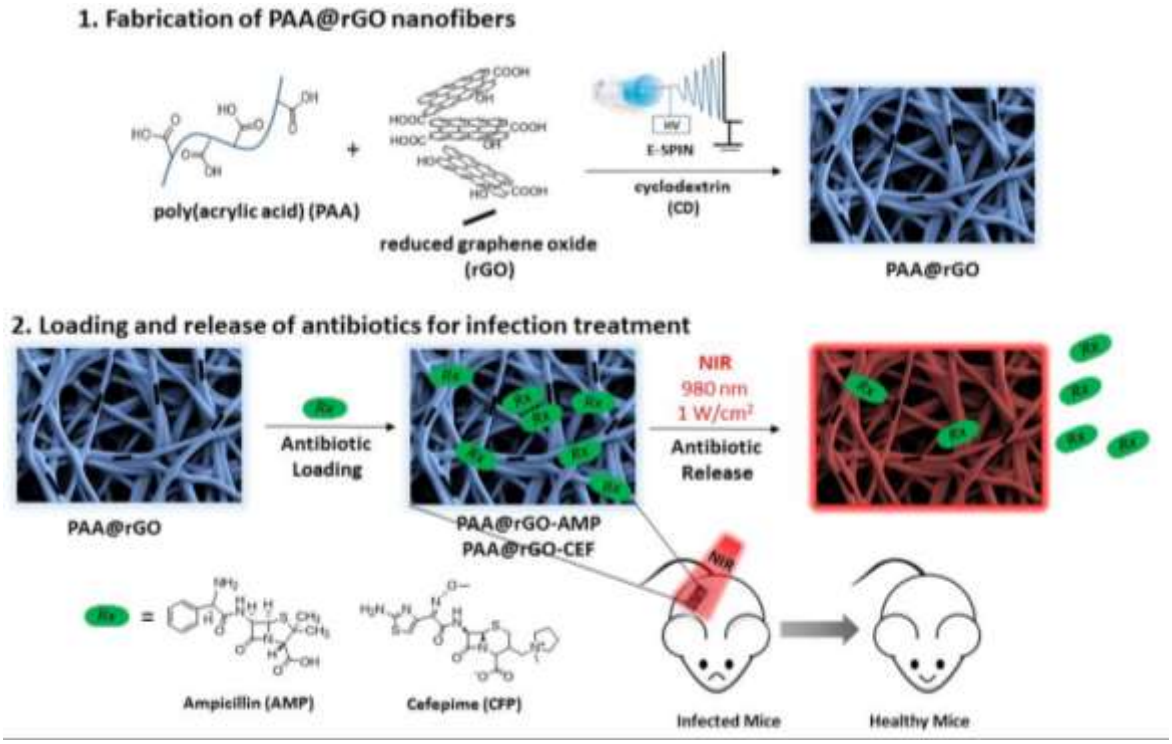

Figure 1.20. General scheme for fabrication and applications of photo-thermally triggered nanofibers [8]

1.6. Reduced Graphene Oxide (r-GO)

Graphene is a monatomic thin layer of sp^2 hybridized carbon atoms organized in the form of a hexagonal lattice structure. Graphene provides intended features such as physical durability, electrical conductivity, and photothermal property. However, its low solubility and complex synthetic patterns cause limitations in the application area. That's why the derivatives of graphene, such as graphene oxide (GO) and reduced graphene oxide (r-GO), are most commonly used in polymer-based nanomaterials design. Fundamentally, GO is a water-dispersible derivative of a multilayered structure of oxidized graphene bearing different functional groups like carboxy, hydroxyl, alkoxy, and carboxylic acid groups, while the reduction of GO [67] attains r-GO. Oxidizing graphene provides improved dispersity in water, whereas it ruins electrical conjugation enabling the heating property (Figure 1.21). To overcome this challenge, GO is reduced to r-GO containing fewer functional groups and having better electrical conjugation with ideal water dispersity. Besides, characteristic features of reduced graphene oxide can be used for various applications in different ways [67,68].

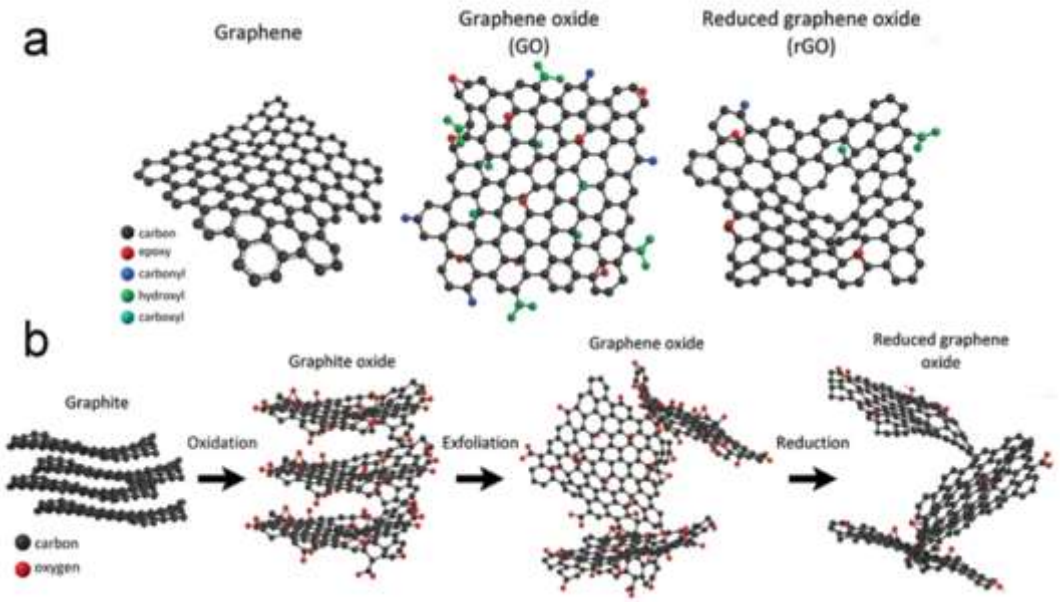

Figure 1.21. a) Scheme for the chemical structure of graphene, graphene oxide, and reduced graphene oxide; b) Schematic route for reduction of graphite to reduced graphene oxide [69].

The number of studies related to r-GO in recent years has remarkably increased in several areas like sensors [70], biomedical applications [71], and absorbers [72]. Selective and proper functionalization of r-GO is vital for biomedical applications. Such that Yan Wu and his coworkers have developed a mesoporous silica (MS) coated polydopamine functionalized reduced graphene oxide (pRGO). Particles were further modified with hyaluronic acid (HA) (pRGO@MS-HA) for synergistic targeted chemo-photothermal therapy against cancer [73]. In this study, simultaneous reduction and noncovalent modification have provided advanced biocompatibility and photothermal effect. Targeting property and enhanced doxorubicin (DOX) loading has been provided by respectively HA modification and MS coating. In vitro studies has affirmed that pRGO@MS(DOX)-HA demonstrates good dispersibility, great photothermal property, spectacular killing efficiency of tumor cell, and specificity in targeting tumor cells. Moreover, in vivo antitumor experiments of this nanoplatform showed remarkable synergistic antitumor efficiency compared to any monotherapy method.

In addition to the characteristic conjugation property of graphene/GO/r-GO, the photothermal feature of graphene and its derivatives have been concerned in biomedical applications. For example, Amitav Sanyal and his coworkers have designed a photothermally activated platform relying on physically caged r-GO into polymeric nanofiber mats to achieve on-demand antibiotic release by irradiation via near-infrared (NIR) laser [8]. In detail, crosslinked polymeric nanofibers were manufactured by using hydrophilic poly(acrylic acid) (PAA) and r-GO in the electrospinning method. Then, antibiotics were loaded into nanofiber mats by immersing them in antibiotic solutions. Since the passive release of the entrapped antibiotics from nanofiber mats was dramatically low, triggering the platform with irradiation of NIR has caused a significant increase in the rate of the released drug. Besides, they proved control over the active release rates of antibiotics through alternating laser power density.

1.7. Near-Infrared (NIR) Activation

Numerous studies about photo-triggered on-demand drug-release systems have appeared to enhance therapeutic efficiency and control over drug administration [66]. It is

challenging to administer chemotherapeutic medications and other treatments to tumor locations in a controlled and targeted delivery. That’s why external light sources such as UV light, NIR, and even visible light are utilized to trigger on-demand releases. Before processing photo-triggered drug release, impacts of the utilized light source must be considered. The skin's response to light irradiation is strongly dependent on wavelength (Figure 1.22). Moreover, providing enough optical energy to the target is frequently challenging due to the skin's absorption properties [74]. For example, NIR light can reach subcutaneous fat, located approximately 6 mm beneath the skin's surface, whereas UV light barely penetrates the skin. However, light in the UV (10–400 nm) and visible (390–700 nm) areas cannot feasibly be employed for deep-tissue triggering due to their considerable absorption through the skin and other tissues. Considering that penetration depth is not a concern in such circumstances, near-surface tissues like the skin, the ear, the back of the eye, and delivery approaches such as transdermal administration are possible options for light-triggering devices.

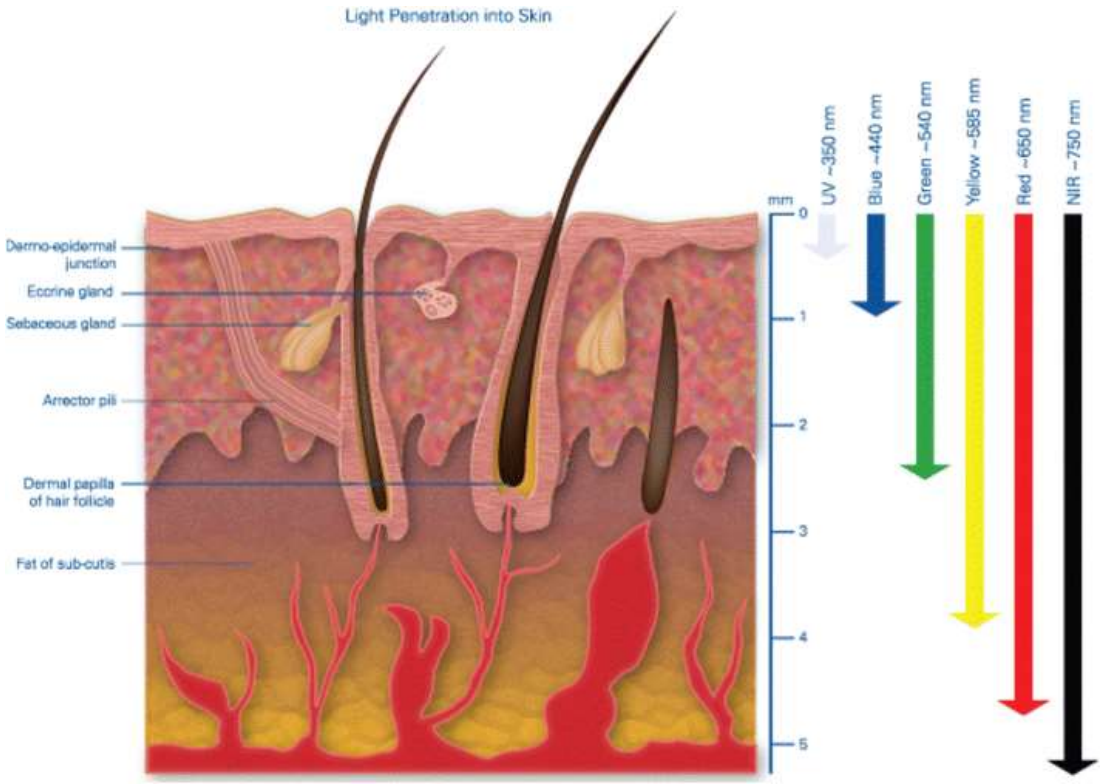

Figure 1.22. Illustration of the depth to which wavelengths penetrate human skin [74].

As an example of NIR-triggered drug release, Lim and coworkers designed NIR-responsive interface crosslinked micelles using Diels-Alder (DA) click reaction between poly(D,L-lactide)-b-poly(furfurylmethacrylate)-b-poly(N-acryloylmorpholine) (PLA-b-PFMA-b-PNAM) triblock copolymers where furan containing monomer has used as the short mid-blocks and cross-linker bis(maleimidoethyl) 3,3′-diselanediyldipropionoate (BMEDSeDP) [75]. Then, this synthesized copolymer was self-assembled into micelles in aqueous media. Subsequently, furfuryl groups undergo a DA click reaction with the maleimide groups at the end of the diselenide cross-linker to form ICL micelles. Doxorubicin (DOX) and indocyanine green (ICG) have been loaded into ICL micelles, which have caused an increase in micellar size. Reactive oxygen species (ROS) were created by NIR irradiation, which then caused the disassembly of ICL and considerably increased the quantity of drug release by cleaving the diselenide link. Moreover, they have performed the cytotoxicity and cellular internalization of DOX-loaded ICL micelles.

1.8. Click Chemistry as a Tool for Functionalization

In synthetic chemistry, rapid reactions involving the three primary characteristics of an ideal synthesis: efficiency, adaptability, and selectivity, have received much attention in the previous decade. The 'click' chemistry is essentially built on the properties of the reactions. In other words, click reactions occur in a one-pot with a high yield in mild conditions without forming offensive byproducts. These click reactions are classified into four groups [76]; cycloaddition reactions (Huisgen 1,3-dipolar cycloaddition, Diels-Alder reactions, nucleophilic ring-opening reactions of strained heterocyclic electrophiles) [77], non-aldol carbonyl chemistry [78], and carbon-carbon double/triple bonds reactions (thiol-ene chemistry, Michael addition reaction) [79].

1.8.1. Diels-Alder Reaction

The 'Diels-Alder' (DA) reaction is based on [4 + 2] cycloaddition between an electron-rich diene and an electron-poor dienophile, which Otto Diels and Kirk Alder discovered the DA reaction in 1928 [80]. The occurrent electrocyclic reaction yields a six-membered ring by generating new stable σ-bonds. Over the years, the DA reaction has been

extensively utilized in developing diverse polymeric structures owing to its reagent-free reaction mechanism, high yield, and thermo-reversibility. Mainly, the DA reactions produce two diastereoisomers: '*endo*' adduct, where the dienophile's substituent is oriented according to the diene π system and '*exo*' adduct where the dienophile's substituent is localized away from diene π system. In the transition state of the cycloaddition reaction, the endo product is controlled as a kinetic product, while the *exo* product is a more stable thermodynamic product (Figure 1.24). In other words, the reaction generates the endo-adduct at low temperatures, whereas the exo-adduct becomes the dominant transition product at high temperatures. Even though the endo product is the sterically hindered product, it has adapted as a preferred transition state, which has been named as Alder endo rule.

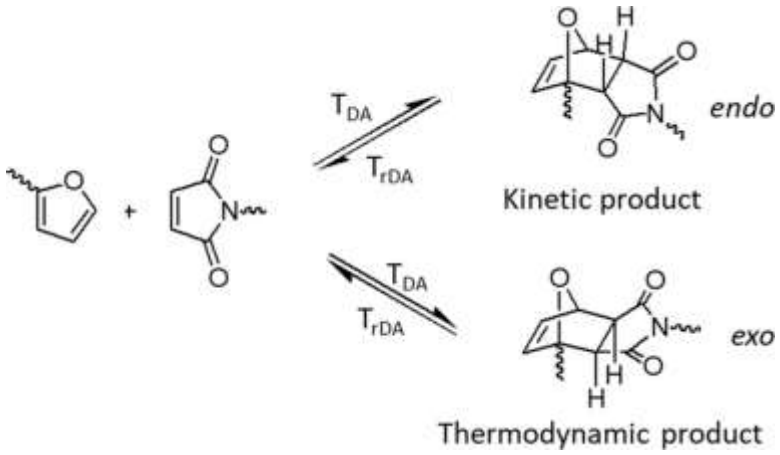

Figure 1.23. Diels-Alder cycloaddition reaction of furan and maleimide and reversibility of their endo-exo-cycloadducts [81].

Since the structural nature of substituents affects the reactivity of the cycloaddition and isomeric ratio [82], choosing appropriate dienes and dienophiles according to the desired design is essential. The typical dienes are allene, isoprene, butadiene, norbornadiene, cyclopentadiene, and furan. On the other hand, maleimide has been most commonly used as a dienophile because of its high reactivity. Furan has generally been employed to manufacture thermoresponsive materials in conjunction with the maleimide group. The furan-based exo-cycloadducts are thermoreversible around 110 °C, whereas other cycloadducts require a temperature above 200 °C for thermal reversibility [83].

DA chemistry has been used in polymeric materials such as hydrogels [84], micelles [85], surface coating [86], and nanofibers [87] for conjugating biomolecules, dyes, and drugs.

Furan groups on the polymeric material's side chains can also be generated by either incorporating furan with small molecules or using furan-containing monomers. Specifically, a commercially available monomer, furfuryl methacrylate (FMA), has been excessively used to fabricate polymer chains. This furan-containing monomer is ready for functionalization with a dienophile using the DA reaction. For example, Sanyal and coworkers have designed furan-based hydrophilic polymeric electrospun nanofibers for functionalization with different maleimide-containing molecules and ligands to mediate the immobilization of protein streptavidin [87]. In their study, they demonstrated the effective functionalization of furan-based nanofibers in a manner of reagent-free conditions in aqueous media (Figure 1.24).

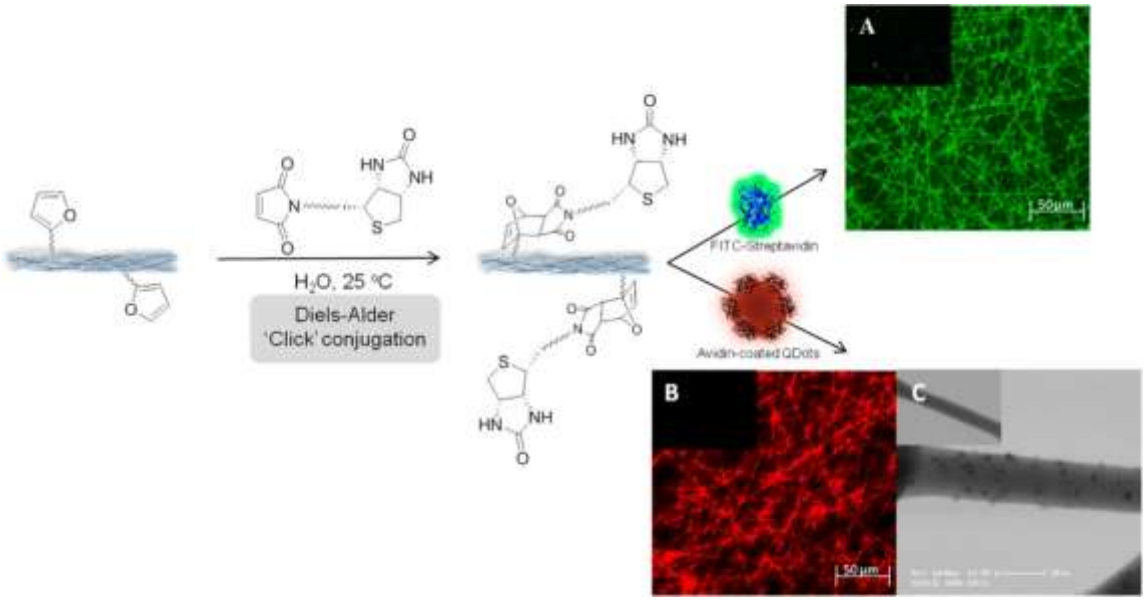

Figure 1.24. Biotin functionalized furan containing nanofibers attained through DA reaction and their fluorescence microscopy images [87].

2. AIM OF THE STUDY

The primary goal of this study is to design a stimuli-responsive drug delivery for the release of a chemically conjugated drug through irradiation of photothermally activable polymeric nanofibers. The thermoresponsive system needed to accomplish such a delivery system is based on the combination of the Diels-Alder/retro-Diels Alder reaction between furan and maleimide. To design a photothermal nanofiber-based drug delivery system, furan-functionalized copolymers were synthesized using free radical polymerization of furfuryl methacrylate and methyl methacrylate. The electrospinning technique was utilized for the production of nanofibers. Reduced graphene oxide was loaded into the furan-bearing nanofibers to provide photothermally responsive property. For heating, a near-infrared laser was utilized to irradiate the furan-functionalized reduced graphene oxide embedded nanofibers. After modifying the parent drug molecule, doxorubicin-maleimide was conjugated onto the nanofibers using the Diels-Alder 'click' chemistry between the maleimide group on the drug and the furan group on the fibers. This reaction provides a thermosensitive conjugation on nanofibrous mats where drug release can be triggered upon heating induced by irradiation with a NIR laser. Retro Diels-Alder reaction will occur upon increasing temperature, and the conjugated drug will be released.

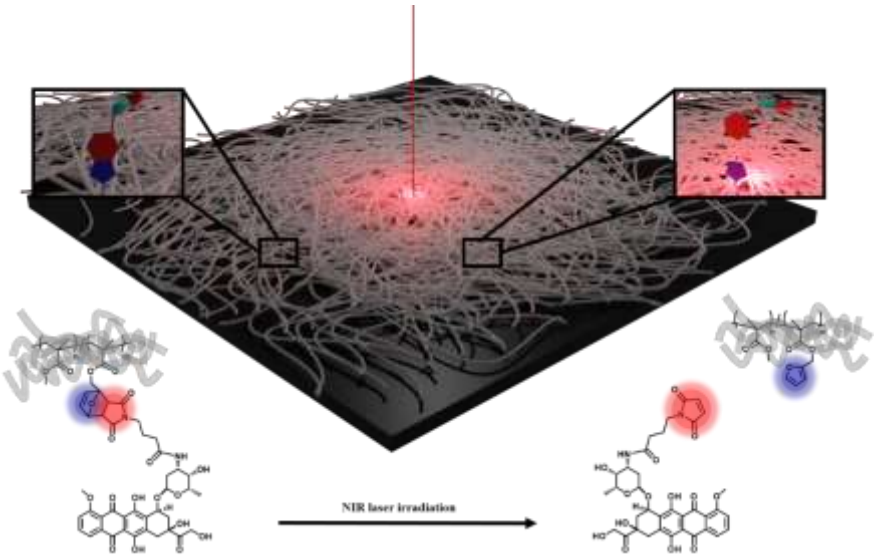

Figure 2.1. Depicted scheme of the aim of the project

3. EXPERIMENTAL

3.1.1. Materials

Dimethylformamide (DMF), tetrahydrofuran (THF), dichloromethane (DCM), and ethyl acetate (EtOAc) and also methyl methacrylate and maleic anhydride were purchased from Merck. Furfuryl methacrylate, 2,2′-azobis(2-methylpropionitrile) (AIBN) and *N*-(5-fluoresceinyl)-maleimide (F-Mal) were obtained from Sigma-Aldrich. Methyl methacrylate, 4-aminobutyric acid, furan, *N*-ethylmaleimide, *N*-hydroxysuccinimide (NHS) and *N*,*N*-dicyclohexylcarbodiimide (DCC) were purchased from Alfa Aesar. Anhydrous solvents such as CH_2Cl_2, THF, and toluene was obtained from ScimatCo Purification System.

3.1.2. Instrumentation

The synthesized copolymer was characterized using ^{1}H-NMR and ^{12}C-NMR spectroscopy (Varian 400 MHz). The molecular weight of the synthesized copolymer was identified with gel permeation chromatography (GPC) using Shimadzu PSSSDV (length/ID 8 × 300 mm, 10 μm particle size) mixed-C column. Micromorphology of produced nanofibers was characterized with JEOL NeoScope JCM-5000 scanning electron microscopy (SEM) that involves an accelerating voltage of 10 kV. Fluorescence images of the modified polymeric nanofibers were taken on a Zeiss Observer Z1 fluorescence microscope linked to a Zeiss Observer Z1 fluorescence microscope connected to Axiocam MRc5 using a Zeiss Filter set 38 (Excitation BP 470/40, Emission BP 525/50) for screening the functionalized nanofibrous mats. r-GO-PFMA-PMMA-NFs were irradiated with the usage of a 980 nm-continuous wave laser. Characterization of F-Mal upon irradiation with NIR light was provided via Varian Cary-100 UV-Vis Spectrophotometer. The concentration of released N-ethylmaleimide and DOX-Mal from r-GO-PFMA-PMMA-NFs was determined by an HPLC system (Shimadzu, Tokyo, Japan).

3.1.3. Synthesis of Furan Containing Copolymers

Commercially purchased furfuryl methacrylate (FMA) and methyl methacrylate (MMA) monomers were passed through the basic aluminum oxide to remove residual inhibitors. FMA (500.0 mg, 3.01 mmol), MMA (162.2 mg, 1.62 mmol), and AIBN (2.30 mg, 0.014 mmol) as an initiator of the polymerization were dissolved in DMF (1.4 mL) in a 25 mL round-bottom flask. Reaction media was purged with nitrogen gas for half an hour before starting the reaction. Afterward, the round bottom flask was left in an oil bath set to 80 °C and stirred for 24h to complete polymerization. After the reaction was completed, the solvent was evaporated under a vacuum. Lastly, thus obtained residue was dissolved in a small amount of CH_2Cl_2 and then added to cold ethanol (EtOH) solution drop by drop to obtain a precipitate, which was dried under a high vacuum for 24 hours. ^{1}H-NMR (400 MHz, $CDCl_3$, δ, ppm): 7.35 (s, 1H furan), 6.32 (s, 1H furan), 6.27 (s, 1H furan), 4.85 (br s, 2H, –O*CH*$_2$–furan), 3.49 (s, 3H, O*CH*$_3$).

3.1.4. Preparation of r-GO-PFMA-PMMA

r-GO containing nanofibers were obtained by adding 1 mg r-GO (1% w/w) into the 100 mg furan-functionalized copolymer solution in 250 μL DMF. To enhance the solubility of r-GO content in the polymeric solution, 30 minutes of sonication was applied to the mixture. After the sonication, the mixture was stirred for 24 hours at room temperature.

3.1.5. Preparation of r-GO-PMMA

Non-functionalized r-GO containing nanofibers as control were produced by simply stirring and solving 100 mg MMA containing 1 mg r-GO (1% w/w) in a mixture of 600 μL DMF and 600 μL THF for 24 hours.

3.1.6. Electrospinning of r-GO-PFMA-PMMA Copolymer

r-GO-PFMA-PMMA polymer solution was electrospun by utilizing a 1 mL syringe fitted with a 14-gauge blunt needle using a flow rate of 0,008 mL.min^{-1}. During the

electrospinning process, the applied voltage was set up to 15 kW, while the distance between the tip of the needle and the aluminum foil-coated metal plate collector was 20 cm.

3.1.7. Electrospinning of r-GO-PMMA

Electrospinning was applied to the polymeric solution of r-GO-PMMA to generate nanofibers. For this purpose, the polymeric solution was taken into a 1 mL syringe fitted with a 14-gauge blunt needle via a flow rate of 0.01 $mL.min^{-1}$ while the applied voltage was 15 kV, and the distance between the electrodes was 15 cm.

3.1.8. Fluorescent Dye Conjugation to r-GO-PFMA-PMMA-NFs

To proceed with the conjugation, initially, N-(5-Fluoresceinyl)maleimide (1 mg/mL) solution was prepared in 1 mL of 1×PBS. Loading of F-Mal dye into r-GO-PFMA-PMMA-NFs was achieved by dropping the dye solution onto electrospun nanofibers that were formerly collected on the glass slide and after shaking (150 rpm) at 37 °C for 24 h. Control experiments of the conjugation of the dye were performed by dropping of the same concentration of F-Mal solution onto merely r-GO-PMMA-NFs and shaking the glass slide with environmentally same conditions of r-GO-PFMA-PMMA-NFs. After the loading period, nanofibers on the glass slides were rinsed with an excess amount of 1xPBS to get rid of either physically caged or loaded fluorescent dye. Nanofibers chemically conjugated with F-Mal were examined and characterized under fluorescence microscopy.

3.1.9. Release of Chemically Bonded F-Mal from r-GO-PFMA-PMMA-NFs

To achieve rDA reaction by the help of photothermal responsivity of r-GO, r-GO-PFMA-PMMA-NFs were heated to 60 °C with a NIR laser (1.5 W, 3 cm, 980 nm) for 15-minute intervals five times. Then, the nanofibers were washed with excess 1xPBS for three times to remove the released F-Mal. Lastly, characterization and monitoring of these nanofibers were performed and recorded by fluorescence microscopy.

3.1.10. Synthesis of Furan Protected Maleic Anhydride (FuMa)

This product was prepared according to previous reports. Firstly, maleic anhydride (10.4 g, 0.153 mol) was dissolved entirely in the presence of toluene at 80°C. Subsequently, furan (10 g, 0.102 mol) was cautiously added to the reaction media since it was volatile. Under reflux media, the mixture was kept for 6 hours. As the reaction completed, the reaction flask was left in a -20 °C fridge for overnight to yield the product. The formed white-yellow residue was washed with 20 ml of hexane to eliminate possible impurities. Before the characterization of the product, the obtained residue was dried under a high vacuum for 24 hours.

3.1.11. Synthesis of Furan Protected Maleimide Acid (FuMa-Acid)

This product was prepared according to previous reports. To synthesize FuMa-Acid, FuMa (1.5 g, 0.009 mol) was dissolved in 11.25 mL tetrahydrofuran (THF) and 11.25 mL methanol (MeOH) in a round bottom flask. After complete dissolving with the help of sonication, 4-aminobutyric acid (2.78 g, 0.027 mol) was added to the reaction flask. Then, the reaction was refluxed for 12 hours at 50 °C. To purify the product, solvent was evaporated, followed by extraction by dissolving the product with a small amount of d.H_2O and an excess amount of CH_2Cl_2. Then, the organic phase was collected and dried over Na_2SO_4 to remove residual water in the organic phase. Lastly, filtration was done to separate the salt from the organic phase, and CH_2Cl_2 was evaporated. The attained residue after evaporation was dried under a high vacuum. ^{1}H-NMR (400 MHz, $CDCl_3$, δ, ppm): 6.54 (m, 2H, -*HC*=*CH*-furan), 5.30 (br s, 2H, –O*CH*–furan), 3.59 (m, 3H, -CH_3), 2.87 (m, 2H, -HC-*CH*-C=O-maleimide), 2.38 (m, 3H, -CH_3), 1.94 (m, 2H, -CH_2).

3.1.12. Synthesis of Maleimide Acid (Mal-Acid)

Unprotected Mal-Acid was synthesized by following rDA reaction. FuMa-Acid (200 mg, 0.843 mmol) and 250 mL dry toluene were mixed under reflux at 110 °C for 6 hours. ^{1}H-NMR (400 MHz, DMSO, δ, ppm): 12.10 (br s, 1H, *HO*-C=O), 7.01 (s, 2H, -*HC*=*CH*-maleimide), 3.43 (m, 3H, -CH_3), 2.21 (m, 3H, -CH_3), 1.71 (m, 2H, -CH_2).

3.1.13. Synthesis of Maleimide-NHS (Mal-NHS)

Mal-NHS was prepared by separately dissolving Mal-Acid (150 mg, 0.82 mmol) and N-hydroxysuccinimide (NHS) (94.3 mg, 0.82 mmol) in 1.5 mL dry CH_2Cl_2 and dissolving DCC (170 mg, 0.82 mmol) in 1.5 mL dry CH_2Cl_2. After complete dissolution of Mal-NHS, the temperature of the reaction flask was lowered to 0 °C while stirring. DCC solution was added drop by drop into the flask. The reaction flask was carried to room temperature after 10 minutes at 0 °C and subsequently left for 20 hours. ^{1}H-NMR (400 MHz, DMSO, δ, ppm): 7.06 (s, 2H, -*HC=CH*- maleimide), 3.55 (m, 3H, -CH_3), 2.87 (s, -N-C=O-CH_2), 2.78 (m, 3H, -CH_3), 1.90 (m, 2H, -CH_2).

3.1.14. Synthesis of Doxorubicin-Maleimide (DOX-Mal)

DOX-Mal was synthesized according to the literature [88]. Briefly, Doxorubicin HCl salt (DOX•HCl) (87 mg, 0.15 mmol) was dissolved in 9.22 mL DMF. Then, wholly dissolved doxorubicin salt was treated with diisopropylethylamine (DIPEA) (130 μL, 0.75 mmol), and the reaction flask was covered with aluminum foil. The mixture was stirred and purged with nitrogen at 25 °C to attain a dark red and transparent solution. Mal-NHS was dissolved in 2.24 mL DMF and subsequently added to reaction media drop by drop. The reaction flask was left at 25 °C for stirring for 24 hours. After the completed reaction, to get all DOX-Mal content in the solution, firstly solvent was evaporated with the help of the route at 37-38 °C. The obtained reddish residue was mixed with anhydrous ether (50 mL) to attain an unclear solution. This suspension was sonicated for 15 minutes and was collected by using suction filtration. It was then washed with cold ether. The resulting product was purified by following the procedure three times; the acquired solid was dissolved in CH_2Cl_2 via sonication to eliminate all unreacted DOX since it is insoluble in CH_2Cl_2. Suction filtration was applied to this solution to remove solid DOX. Then, the reddish solution was concentrated to one-tenth of its original volume by evaporating CH_2Cl_2. Anhydrous ether was drop by drop added to yield the product as a precipitate. Lastly, the solid was collected and dried with a high vacuum.

3.1.15. Conjugation of DOX-Mal to r-GO-PFMA-PMMA-NFs

A solution of DOX-Mal (1 mg/mL) was prepared in 1xPBS. Then, a 20 mg piece of a fibrous mat of r-GO-PFMA-PMMA-NFs was dipped into 1 mL of the Doc-containing solution and stirred in dark for 24 hours at 25 °C. After loading of DOX-Mal chemically, the mat was rinsed nine times with 1 mL portions of EtOH to get rid of both physically encapsulated and interacted DOX-Mal into the nanofibers. To ensure there was no physically entrapped DOX-Mal before exposing the nanofibers to NIR Laser, the process was followed with liquid chromatography-mass spectrometry (LC-MS). As a control experiment, a mat of r-GO-PMMA-NFs was stirred within 1 mL of DOX-Mal (1 mg/mL) solution. After 24 hours, r-GO-PMMA-NFs were rinsed nine times with 1 mL of EtOH. Again, all of the collected solutions from the rinsing process were analyzed with LC-MS.

3.1.16. Release of DOX-Mal from r-GO-PFMA-PMMA-NFs

DOX-Mal loaded r-GO-PFMA-PMMA-NFs over the surface of 1 mL 1xPBS solution were irradiated with NIR laser (980 nm, 1.5 W) for 15 min. pulses. A photothermal camera was utilized to monitor the temperature of the irradiated area. At the end of 15 minutes of irradiation above 60 °C, the release solution was refreshed with another 1 mL portion of 1xPBS. Then, the passive release was done for 30 minutes without irradiation with NIR light at 37 °C. Following NIR light on-off release system for DOX-Mal from r-GO-PFMA-PMMA-NFs was operated four consecutive times. Attained release solutions were examined and characterized with liquid chromatography-mass spectrometry-mass spectrometry (LC-MS/MS).

4. RESULTS AND DISCUSSION

4.1.1. Synthesis and Characterization of PFMA-PMMA Copolymer

Furan-functionalized, MMA-containing copolymers were synthesized through a free radical polymerization. In the polymer chain, furan groups were used as diene (electron-rich) reactive groups for further functionalization. At the same time, the MMA group was used to enhance hydrophobicity and also fiber-making tendency. Before polymerization, FMA and MMA monomers were passed through basic Al_2O_3 to remove inhibitors. Polymerization was completed under a nitrogen atmosphere in DMF at 80°C using AIBN as the initiator (Figure 4.1). Purification of the obtained copolymers was provided with precipitation in cold EtOH. At the end of purification, the yield of the free radical polymerization was 89 %. The ratio of FMA and MMA units in the copolymer was calculated as 1:1. Characterization of the synthesized polymer was done by using ^{1}H-NMR spectroscopy (Figure 4.2), ^{13}C-NMR spectroscopy (Figure 4.3), and gel permeation chromatography (GPC) (Figure 4.4).

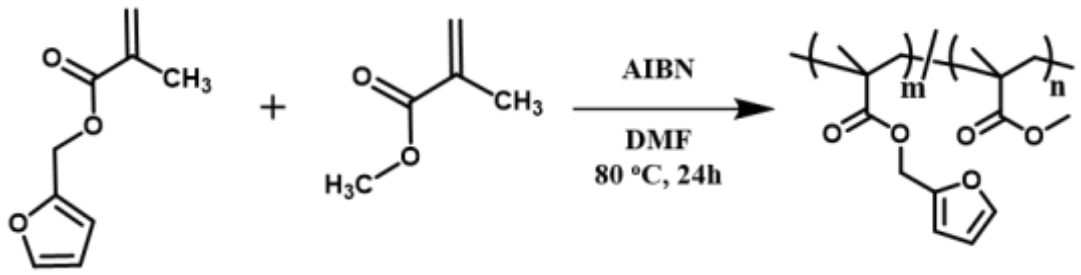

Figure 4.1. Schematic representation of the free radical polymerization to synthesize furan functionalized copolymer.

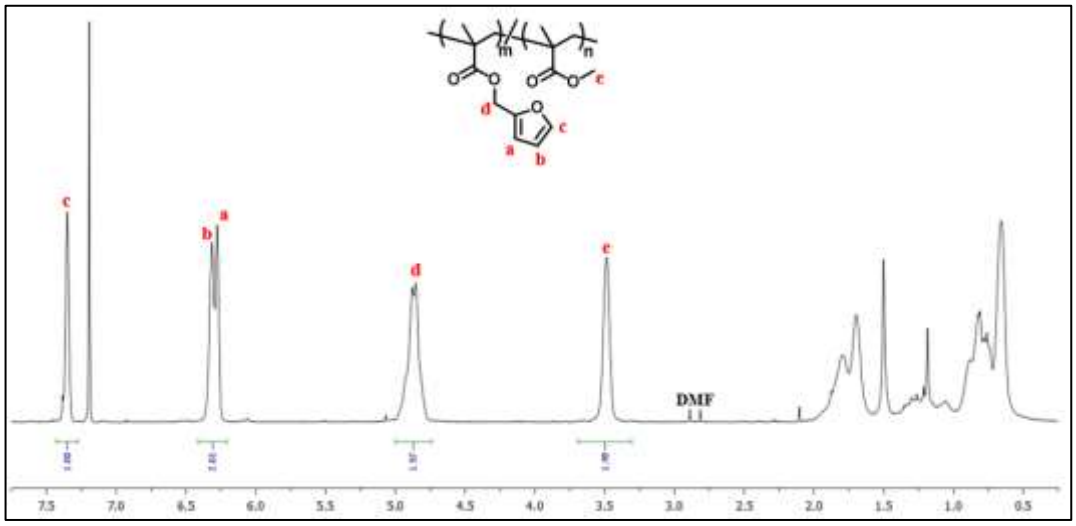

Figure 4.2. [1]H-NMR spectrum of PFMA-PMMA copolymer

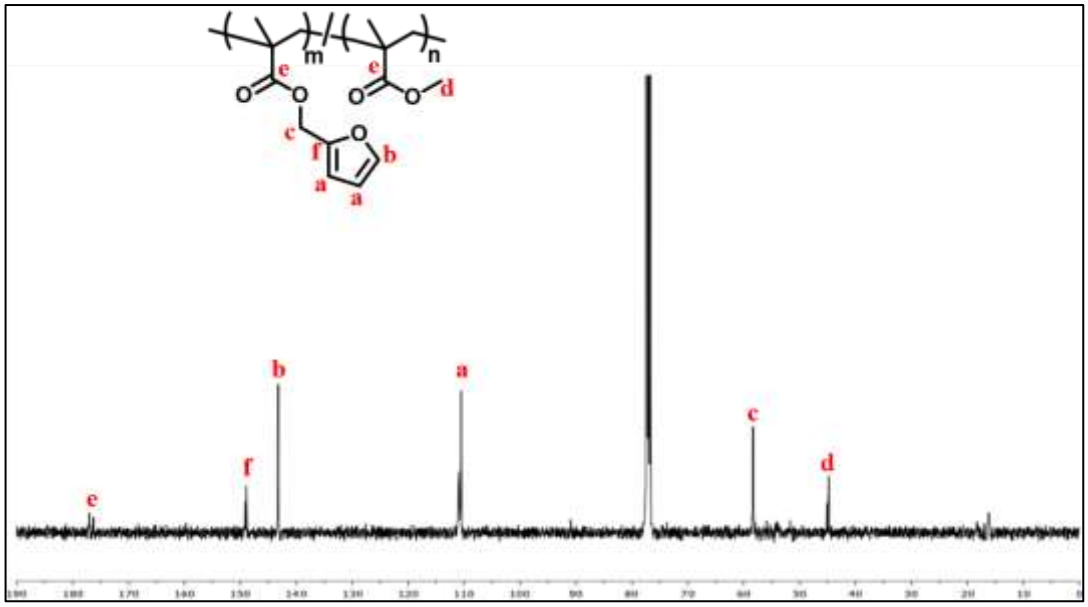

Figure 4.3. [13]C-NMR spectrum of PFMA-PMMA copolymer.

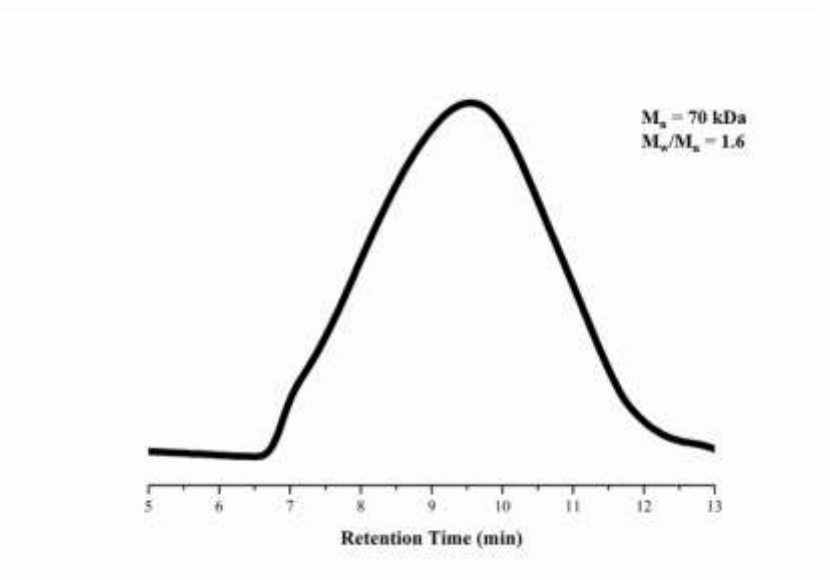

Figure 4.4. GPC trace of PFMA-PMMA copolymer.

4.1.2. Fabrication and Characterization of PFMA-PMMA-NFs

After successfully synthesizing the PFMA-PMMA copolymer, furan-functionalized nanofiber was generated by using electrospinning of the polymer solution in DMF (Figure 4.5). Optimum electrospinning conditions to produce a nanofiber with minimum bead and appropriate diameter were obtained as the applied voltage was 15 kV, the distance between the end of the needle's tip and collector was 20 cm, and the pump rate was set to 8 μL/min. The fabricated functional polymeric nanofibers were characterized using SEM.

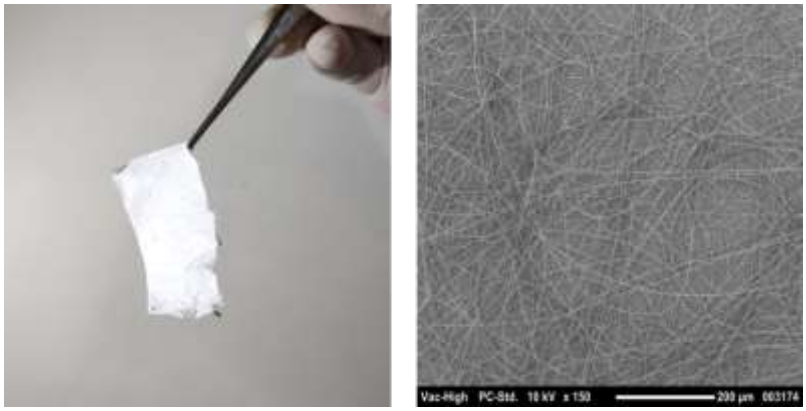

Figure 4.5. On the left; a piece of PFMA-PMMA nanofibrous mat, on the right; SEM image of the manufactured nanofiber.

In order to optimize the physical morphology of fabricated nanofibers, r-GO-PFMA-PMMA copolymer solutions were prepared at different concentrations when other parameters were constant. Such that the most promising nanofibers that had the minimum number of beads and proper diameter were obtained with the solvent of 250 µL DMF. As the concentration of the polymer was increased (225 µL DMF), less bead formation was observed, whereas thicker fibers were obtained. Thicker nanofibers were not preferable since they had less surface area for further conjugation. In the contrary, whenever the electrospinning was applied to diluted polymer solution (275 µL DMF), there existed an absolute increase in the number and the size of beads and also thinner nanofibers were observed (Figure 4.6). As a numeric characterization for nanofibers diameter, histogram results also presented the increase in average diameter of 347.44±90.40 nm, 475.87±94.28 nm, 1157.62±155.19 nm from the most diluted to the most concentrated environment respectively.

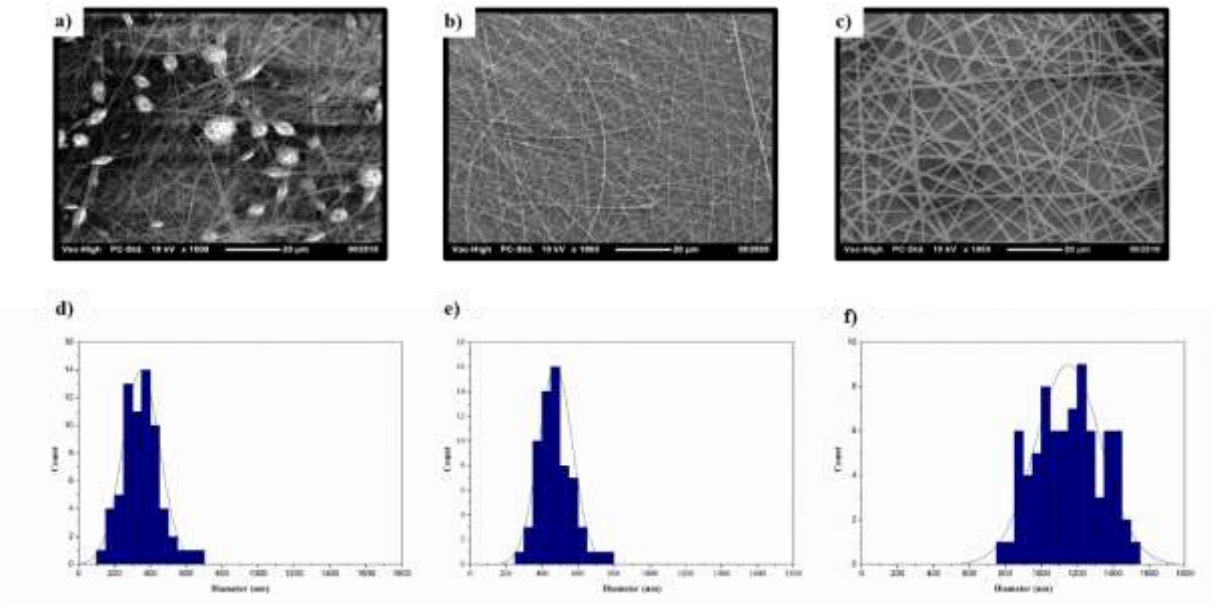

Figure 4.6. SEM images of the fabricated nanofibers at different concentrations; a) 275, b) 250, and c) 225 µL DMF, histogram results belonging to d) 275 e) 250 f) 225 µL DMF.

4.1.3. Functionalization of PFMA-PMMA-NFs

Functionalization of furan-containing nanofibers has been achieved in various ways in this project. First, a corporation of 1 mg r-GO (1% w/w) was done by mixing it with PFMA-PMMA polymer solution in DMF to give PFMA-PMMA-NFs a heatable property since r-GO converts the absorbed light energy into heat. Electrospinning was applied on r-GO-PFMA-PMMA (black colored solution in Figure 4.7) to fabricate photothermal nanofibers. To identify r-GO-PFMA-PMMA-NF, an excellent digital picture was taken. (Figure 4.7).

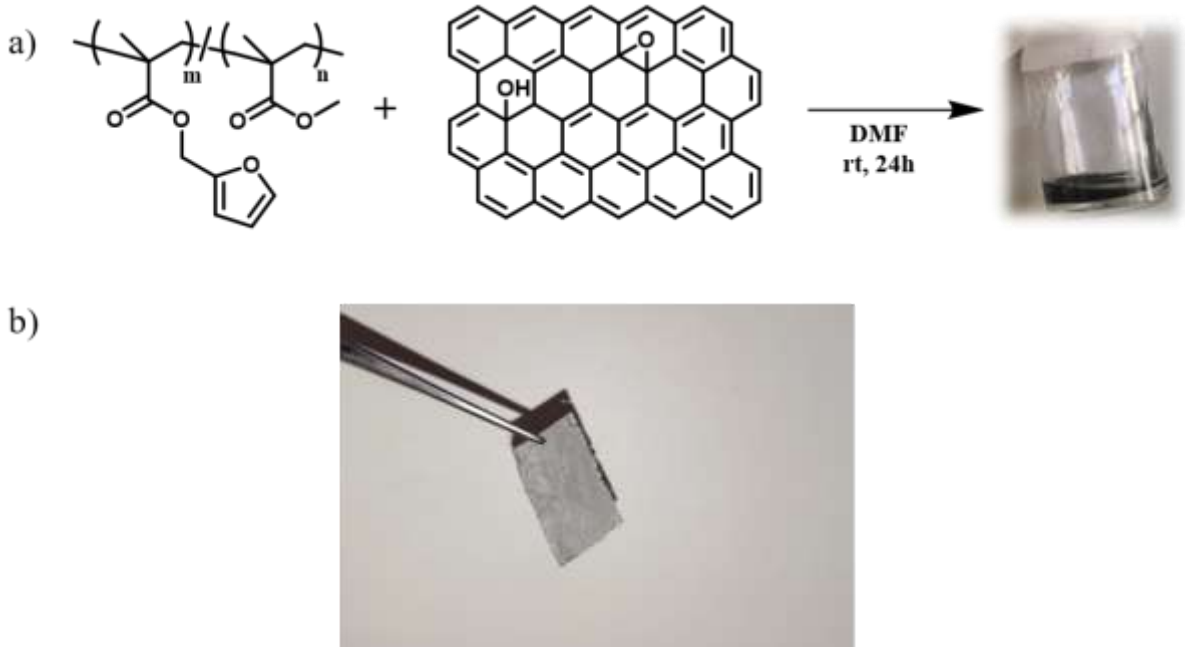

Figure 4.7. a) Schematic presentation of the preparation of r-GO-PFMA-PMMA polymer solution before applying electrospinning, b) Digital image of r-GO-PFMA-PMMA-NFs.

It is crucial to control over temperature on the surface of the nanofibers since rDA of furan-maleimide adduct requires at least 60 °C. Besides, optimum distance and power density are required to prevent skin damage over the applied region during irradiation. That's why the characterization of the heating property of the nanofibrous material has been achieved under different beam powers as other radiation parameters like distance between laser source and the surface of the r-GO-PFMA-PMMA-NFs (3 cm) and wavelength of the

light (980 nm) are held constant. (Figure 4.8). The attained results indicate that as the distance between the surface of the nanofiber and the end of the laser column becomes shorter, reached maximum temperature increases. When the power density of the applied laser increases, acquired temperature increases as well.

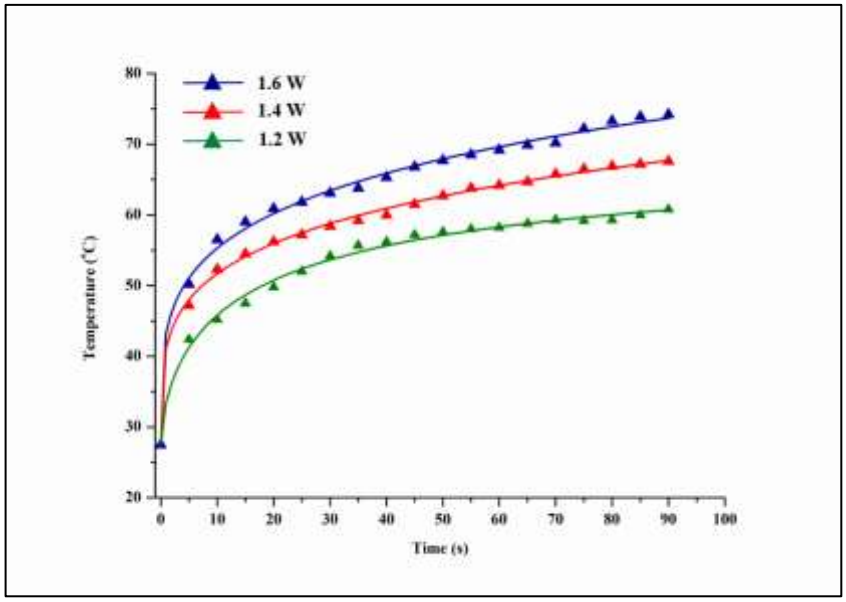

Figure 4.8. Temperature vs. time graph of the r-GO (1% w/w) containing functional nanofibrous mat under different beam powers.

To gain an insight into nanofiber functionalization, r-GO-PFMA-PMMA-NFs was modified with F-Mal, a furan reactive fluorescent dye. Fluorescent labeling of maleimide enables imaging of r-GO-PFMA-PMMA-NFs after and before loading (Figure 4.9).

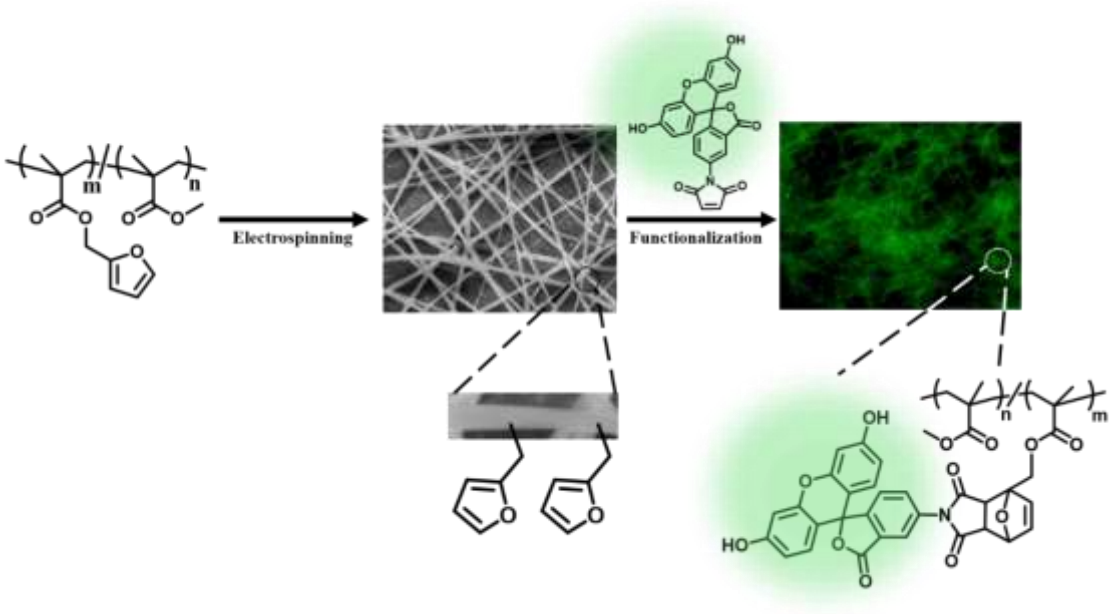

Figure 4.9. Schematic scheme for conjugation of F-Mal to r-GO-PFMA-PMMA-NFs.

The DA reaction occurred between furan groups on polymer side chains and the maleimide group on the molecule. Subsequently, physically bonded or encapsulated molecules were removed by simply washing the material with portions of 1xPBS solution five times in a row. UV spectroscopy was used to ensure there was no left unbonded or physically entrapped F-Mal inside the nanofibers. After successfully conjugating the fluorescent dye on the surface of the nanofiber, the rDA reaction was performed by exposing dye-conjugated nanofibers to NIR laser with 980 nm wavelength and 1.2 W power density. The required energy to achieve rDA was supplied with embedded r-GO content inside nanofibers since it converts the irradiation energy of NIR to heat. In addition, the passive release was carried out at 37 °C within identical time pulses. As a control experiment, r-GO-PMMA-NFs were used, but the non-functional nanofibers did not undergo conjugation with F-Mal. Monitoring the process of loading and release of F-Mal was done with fluorescence microscopy. The results show that the fluorescence intensity of F-Mal decreased in each pulse while remaining constant in a passive release. In the case of non-functional nanofibers (r-GO-PMMA-NFs), images indicated no F-Mal loading (Figure 4.10). In addition, UV spectroscopy was utilized to confirm the photostability of dye that no quenching or degradation is owing to either reaching high temperatures like 60 °C or irradiating with a NIR laser (Figure 4.10).

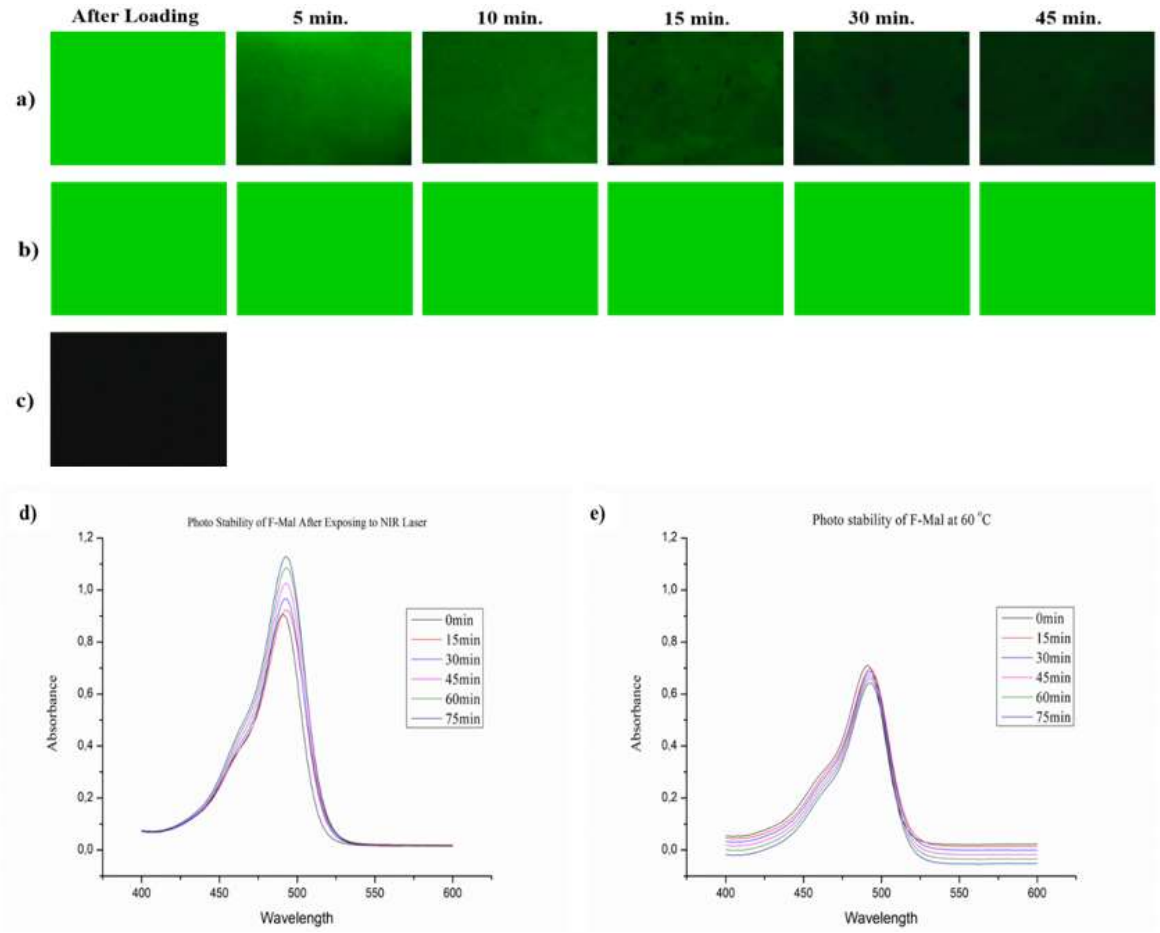

Figure 4.10. Fluorescence microscopy images of functional nanofibers (r-GO-PFMA-PMMA); a) after activation via NIR laser irradiation with 5, 10, 15, 30, and 45 min. pulses; b) after passive release at 37 °C within the same time interval, c) non-functional nanofibers (r-GO-PMMA-NFs), UV spectra of F-Mal; d) after exposure to NIR laser, e) at 60 °C.

Another functionalization of r-GO-PFMA-PMMA-NFs was done with N-ethylmaleimide (E-Mal) as another model molecule. The loading capacity for r-GO-PFMA-PMMA-NFs was calculated from the amount of E-Mal content in the solution before and after loading with LS-MS. The loading was achieved by simply immersing the nanofibers into the solution of 2 mg/mL of E-Mal in 1xPBS for 1 day at 37 °C shaker. As 2 mg/mL E-Mal loading solution was utilized, 1.482±0.153 mg/mL (79.23%) of E-Mal was loaded onto the surface of the nanofibers. In another expression, 0.272±0.006 mg E-Mal were loaded per 1 mg of r-GO-PFMA-PMM-NFs. As a control experiment, r-GO-PMMA-NFs were loaded with E-Mal, whereas LS-MS results after rinsing studied r-GO-PMMA-NFs indicated a trace

amount of E-Mal was determined as loaded. The fundamental reason is that there is no functional group on r-GO-PMMA-NFs that E-Mal can conjugate.

To release the conjugated E-Mal, rDA was performed through irradiation with a NIR laser. When E-Mal-loaded r-GO-PMMA-PFMA-NFs were exposed to NIR laser, the temperature on the surface of the nanofibers increased over 60 °C, which caused cycloreversion to reform the initial diene (r-GO-PMMA-PFMA) and dienophile (E-Mal). Collected released solutions were analyzed with LCMS. Results indicated that the amount of passively released E-Mal from nanofibers was negligible compared with the amount of active release. A dramatic increase in the concentration of released E-Mal was observed. The difference is based on the temperature over the surface of r-GO-PFMA-PMMA-NFs that rDA reaction does not occur at 37 °C. It is also important to mention that half of the released E-Mal proceeded from the first 15 minutes (Figure 4.11).

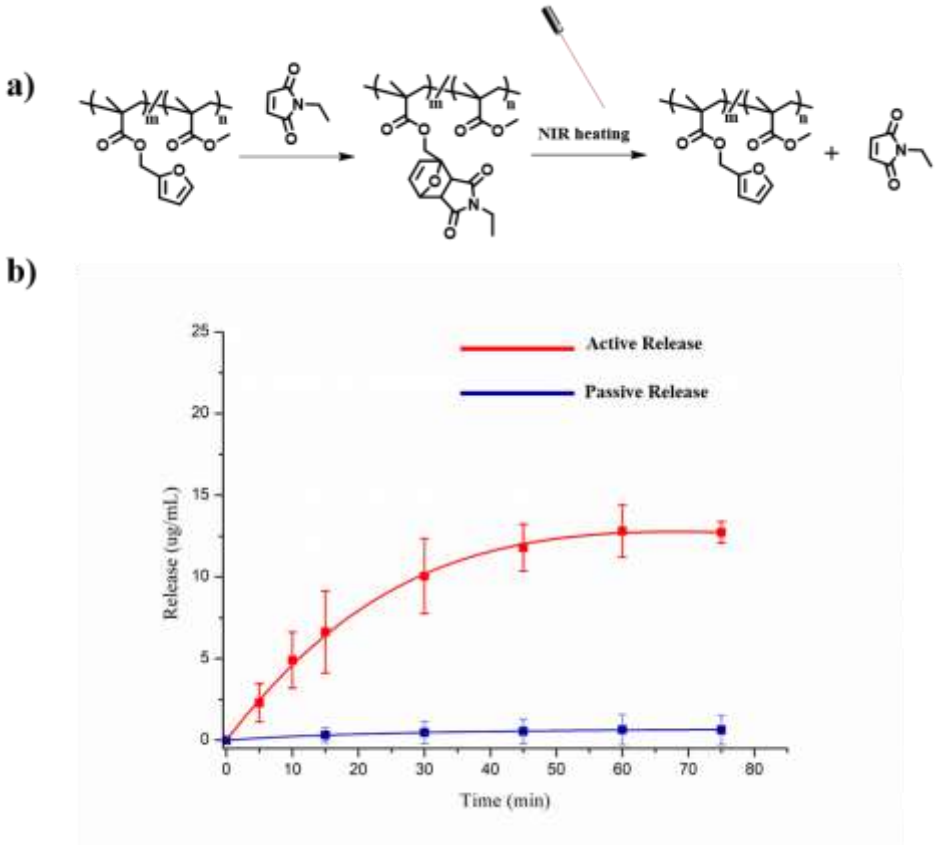

Figure 4.11. a) Reaction scheme for loading and photothermal release of E-Mal, b) Release profile of photothermally stimulated E-Mal from r-GO-PFMA-PMMA-NFs vs. non-triggered r-GO-PFMA-PMMA-NFs.

4.1.4. Drug Modification and Characterization

Doxorubicin (DOX) was preferred as the model drug molecule of choice in this project. However, it needed to be modified to perform DA click chemistry between the drug and fabricated nanofibers. Hence, DOX was modified through amine group (-NH_2) with an activated ester containing maleimide linker (Mal-NHS).

The reaction of maleimide with the furan group is one of the well-known DA reactions to deactivate the maleimide group. In order to synthesize furan protected maleic anhydride, maleic anhydride and furan was refluxed with toluene under 80 °C for 6h. It is important to note that furan was added to reaction media as the temperature reached 80 °C since furan has a low evaporation point. As a purification process, the completed reaction media was left at 0 °C for one day to precipitate the product to take out the exo-product. The obtained product was characterized with ^{1}H-NMR spectroscopy (Figure 4.12).

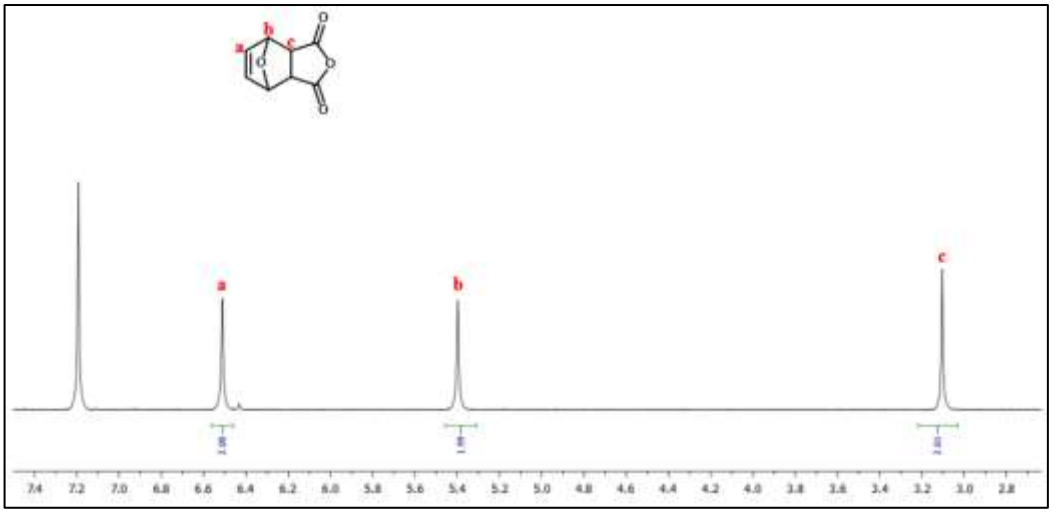

Figure 4.12. ^{1}H-NMR spectrum of FuMa cycloadduct.

After the successful synthesis of FuMa adduct, 4-aminobutyric acid was added to previously dissolved FuMa in THF and CH_3OH under reflux at 65 °C for 12 hours. Identification of the obtained product, furan-protected maleimide acid (FuMa-Acid), was achieved with ^{1}H-NMR spectroscopy (Figure 4.13).

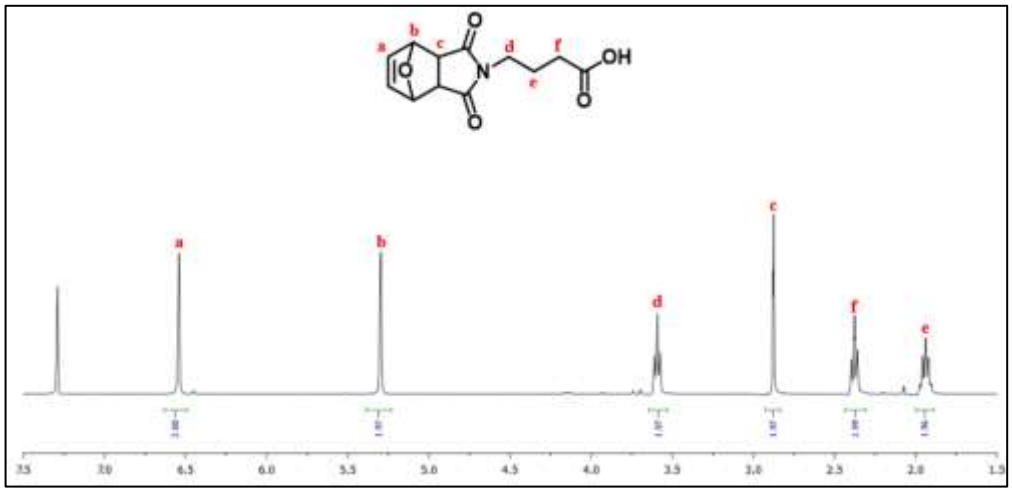

Figure 4.13. ^{1}H-NMR spectrum of FuMa-Acid.

As the next step, the rDA reaction of synthesized FuMa-Acid was undertaken. The temperature of the reaction media was set to 110 °C under reflux since rDA reactions become more convenient at high temperatures. Ma-Acid's retro product characterization was undertaken using ^{1}H-NMR spectroscopy (Figure 4.14).

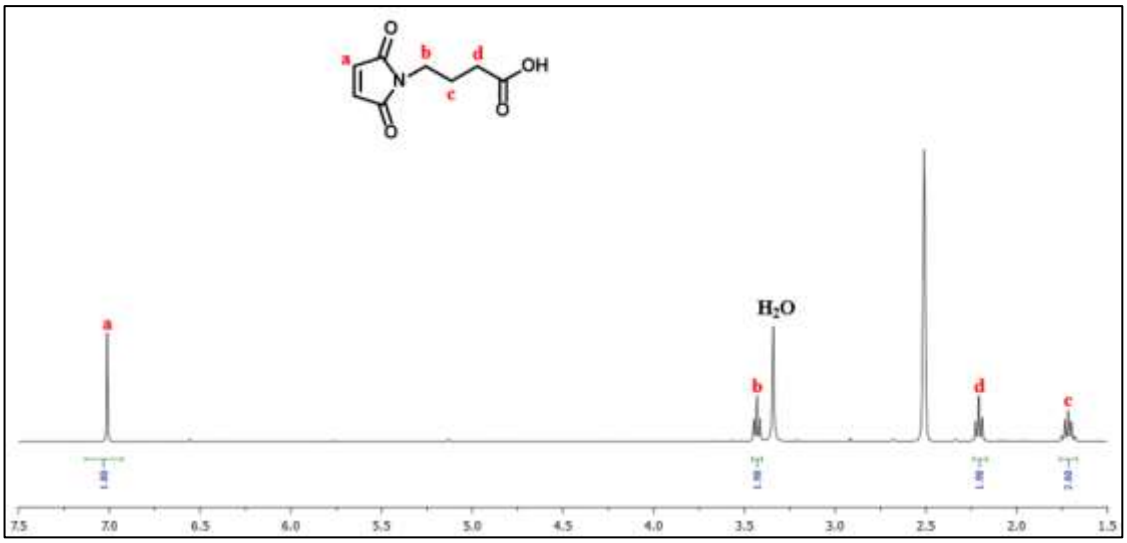

Figure 4.14. ^{1}H-NMR spectrum of Ma-Acid.

Synthesized Ma-Acid involves functionlizable groups such as a maleimide group that shows electron-poor (dienophile) characteristics for DA reactions and an acid group that

can undergo a reaction with the NHS group to generate an activated ester. Since we were planning to modify our parent drug, DOX, through an amine group on its structure, attaining an activated ester was required. That's why NHS group as an activating reagent was preferred. DCC was used as a coupling reagent to generate an excellent leaving group from acid to provide more reactive and activated reaction media DMAP was used as a catalytic base due to its good basicity for esterification. During the esterification of Ma-Acid via DCC/NHS coupling, DCC was converted into DCU, which is hard to eliminate even the last traces since almost insoluble in any organic solvent and aqueous media. Hence filtration was done to eliminate insoluble precipitate DCC and to isolate Mal-NHS. Then, the filtered product was concentrated with the evaporation of the solvent. The remaining solution was added to cold ethyl acetate (EtOAc) dropwise to purify further and obtain the product as a residue. The attained precipitate was collected with the help of a centrifuge and dried under a high vacuum. Obtained Mal-NHS product was characterized with ^{1}H-NMR spectroscopy (Figure 4.15).

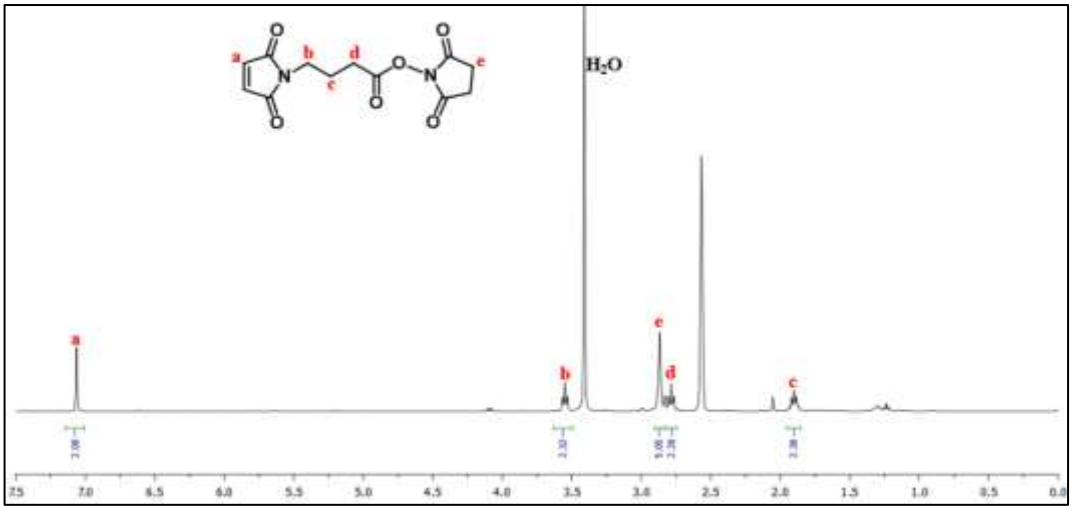

Figure 4.15. ^{1}H-NMR spectrum of Mal-NHS linker.

The formation of amine-reactive NHS-activated ester favors further nucleophilic attack of any amine group in order to generate an amide. In this case, amine groups on DOX were utilized to form maleimide-functionalized doxorubicin (DOX-Mal) through an amide bond. The reaction was conducted simply by mixing DOX and Mal-NHS in the DMF at room temperature, while media was covered with aluminum foil since DOX is sensitive to

light. After following purification processes[88], DOX-Mal was characterized with ^{1}H-NMR spectroscopy. Characteristic peaks indicating the successful synthesis for DOX-Mal appeared at 6.98 ppm and 3.19 ppm belonging to maleimide and alkyl groups between maleimide and amide, respectively. To identify characteristic peaks belonging to DOX-Mal from the spectra, both ^{1}H-NMR spectroscopies of DOX•HCl and DOX-Mal were compared (Figure 4.16). In addition to ^{1}H-NMR spectroscopy, the synthesized drug can be identified by using LCMS. Ion fragments for the corresponding peak to DOX-Mal were recorded as 731 m/z, indicating DOX-Mal's coupling with Na^{+} (23 m) ions. The peak that appeared at 295 m/z belongs to the most dominant ion fragment, which is the base peak for the mass spectra (Figure 4.17).

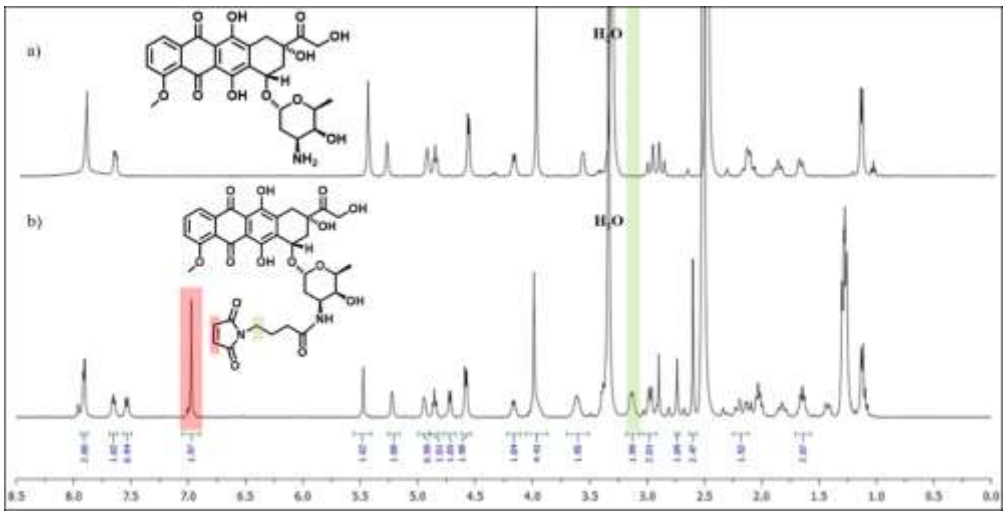

Figure 4.16. ^{1}H-NMR spectrum of a) DOX•HCl, b) DOX-Mal.

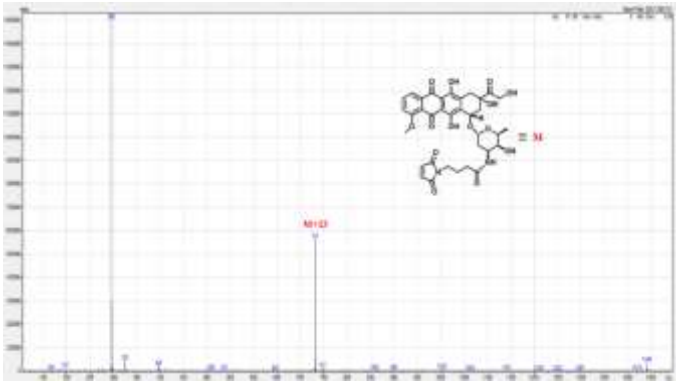

Figure 4.17. Mass spectra of DOX-Mal.

4.1.5. DOX-Mal Conjugation to r-GO-PFMA-PMMA-NFs and Characterization

DOX-Mal was covalently linked to r-GO-PFMA-PMMA-NFs through incubation at room temperature for 24 hours. LC-MS results of rinsing solutions indicated no trace of unbonded or physically entrapped DOX-Mal content. Loading capacity of DOX-Mal was determined from the amount of DOX-Mal in solution after and before loading onto r-GO-PFMA-PMMA-NFs using LS-MS. The loading amount of DOX-Mal was calculated as 0.124±0.017 mg for 1 mg r-GO-PFMA-PMMA-NFs. Imaging of DOX-Mal loaded nanofibers was accomplished using SEM (Figure 4.18). Results showed no evidence of deformation or disruption in the physical morphology of r-GO-PFMA-PMMA-NFs.

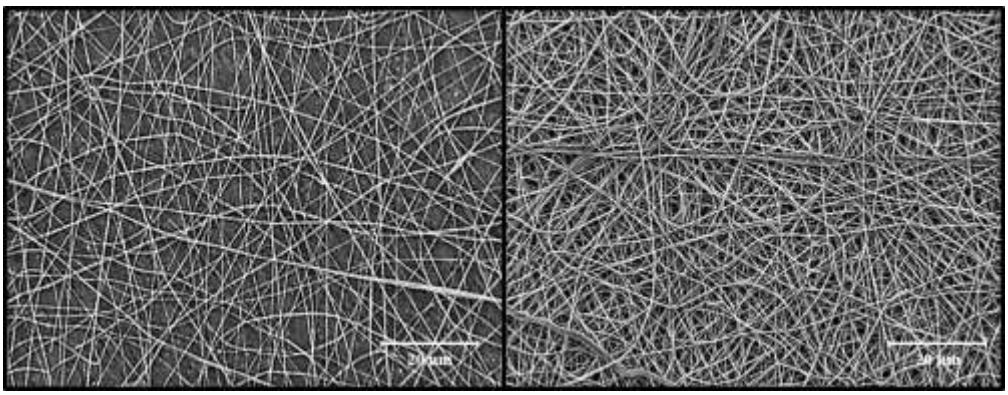

Figure 4.18. SEM images of r-GO-PFMA-PMMA-NFs after and before DOX-Mal loading, respectively.

As a control experiment, 0.01 mg/mL DOX-Mal was loaded into r-GO-PMMA-NFs and r-GO-PFMA-PMMA-NFs simultaneously and incubated at 25 °C for one day. After sufficiently rinsing both nanofibrous mats, r-GO-PMMA-NFs remained white while r-GO-PFMA-PMMA-NFs exhibited reddish-orange color (Figure 4.19). The main reason for the coloration is that r-GO-PFMA-PMMA-NFs involve the furan group in its structure, enabling DA reaction with maleimide on the modified drug. On the other hand, r-GO-PMMA nanofibers have no functional group to be conjugated with DOX-Mal.

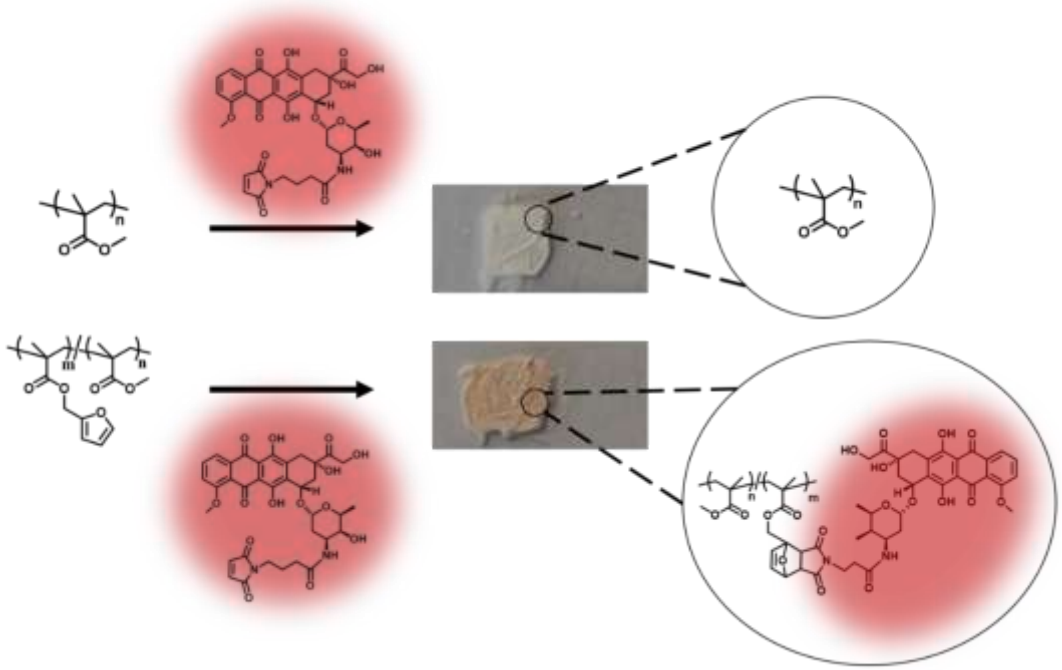

Figure 4.19. Figure 4.19. Schematic illustration of DOX-Mal loading to r-GO-PMMA-NFs and r-GO-PFMA-PMMA-NFs, respectively.

4.1.6. Photothermally Triggered Release of Chemically Conjugated DOX-Mal

The fibrous mat was irradiated with NIR laser (980 nm, 1.5 W) for 15 min. Irradiation was done with a 2 cm distance between the light source and the surface of the fibrous. Control experiments were done on the same mat in a cabin at 37 °C before photothermal activation. Quantitative analysis of the released drug was carried out with LC-MS/MS. Attained results were quite promising that r-GO-PFMA-PMMA-NFs demonstrate no significant amount of release was determined as NIR light was off and DOX-Mal release passively. On the other hand, a considerable amount of released DOX-Mal was obtained as r-GO-PFMA-PMMA-NFs actived upon irradiation with NIR light (Figure 4.20). Numerically, 0.055±0.064 ng of DOX-Mal was released per mg of r-GO-PFMA-PMMA-NFs in passive release within the determined time interval, whereas 0.376±0.384 ng was released from 1 mg of r-GO-PFMA-PMMA-NFs upon irradiation. The chemistry behind this is based on DA ‘click chemistry’ since DA adducts have a thermosensitive bond. As exposing r-GO-PFMA-PMMA-NFs to NIR light, the temperature on the surface of the nanofiber increases, and rDA reaction takes place to release DOX-Mal content.

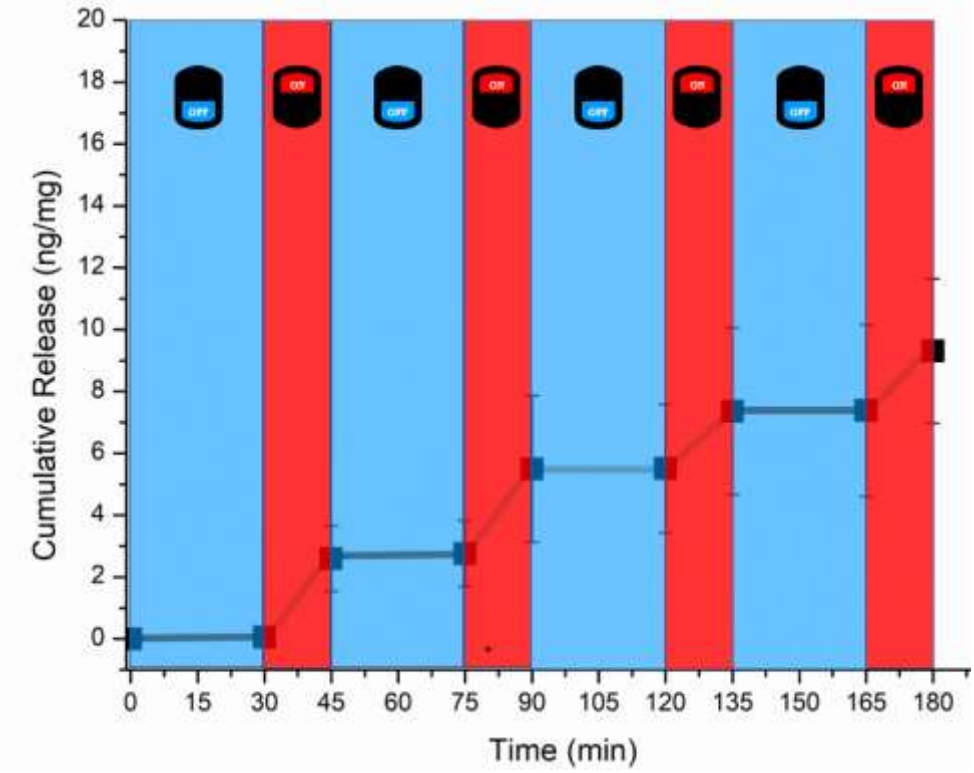

Figure 4.20. The release profile of DOX-Mal upon on-off irradiation with NIR light.

5. CONCLUSION

In this thesis, photothermally activated functional nanofibers were designed for obtaining a drug delivery system based on the Diels-Alder/retro Diels-Alder chemistry. Furan-containing copolymers embedded with r-GO were synthesized via free radical polymerization to generate photothermally responsive electrospun nanofibers, which heat up upon irradiation with NIR light. Then, r-GO-PFMA-PMMA-NFs were conjugated with F-Mal fluorescent dye and E-Mal molecule as models for upcoming reactions. Fluorescence imaging enabled to monitor DA 'click' chemistry between r-GO-PFMA-PMMA-NFs and F-Mal. Besides, ethyl-maleimide was conjugated to r-GO-PFMA-PMMA-NFs as a model cargo to demonstrate photothermally activated release. Nanofibers functionalized with the fluorescent dye and ethylmaleimide were irradiated with NIR light to raise the local temperature, and achieve their release through the retro Diels-Alder reaction. Subsequently, conjugation of DOX-Mal to r-GO-PFMA-PMMA-NFs was undertaken, and photothermal drug release was demonstrated. While passive drug release was minimal, active drug release occurred in a reproducible and repetitive controlled manner. In summary, photothermally activable nanofibers that could undergo conjugation and release of bioactive therapeutic molecules were achieved. One can envision that the modular system obtained here can act as a viable drug delivery device for various diseases.

REFERENCES

1. Sarhan, W.A., H.M.E. Azzazy, and I.M. El-Sherbiny, "Honey/Chitosan Nanofiber Wound Dressing Enriched with Allium Sativum and Cleome Droserifolia: Enhanced Antimicrobial and Wound Healing Activity", *ACS Applied Materials and Interfaces*, Vol. 8, No. 10, pp. 6379–6390, 2016.

2. Nouri, A., B. Faraji Dizaji, N. Kianinejad, A. Jafari Rad, S. Rahimi, M. Irani, and F. Sharifian Jazi, "Simultaneous Linear Release of Folic Acid and Doxorubicin from Ethyl Cellulose/Chitosan/G-C3N4/MoS2 Core-Shell Nanofibers and Its Anticancer Properties", *Journal of Biomedical Materials Research - Part A*, Vol. 109, No. 6, pp. 903–914, 2021.

3. Yoshimoto, H., Y.M. Shin, H. Terai, and J.P. Vacanti, "A Biodegradable Nanofiber Scaffold by Electrospinning and Its Potential for Bone Tissue Engineering", *Biomaterials*, Vol. 24, No. 12, pp. 2077–2082, 2003.

4. Yan, J., H. Yuhui, X. Shuhui, W. Xiao, Y. Zhang, Y. Jianyong, D. Bin, J. Yan, Y. Han, S. Xia, Y.Y. Zhang, J. Yu, B. Ding, and X. Wang, "Polymer Template Synthesis Of Flexible BaTiO 3 Crystal Nanofibers", *Advanced Functional Materials*, Vol. 29, No. 51, p. 1907919, 2019.

5. Ding, F., H. Deng, Y. Du, X. Shi, and Q. Wang, "Emerging Chitin and Chitosan Nanofibrous Materials for Biomedical Applications", *Nanoscale*, Vol. 6, No.16, pp. 9477-9493, 2014.

6. Zhang, C., X. Xue, Q. Luo, Y. Li, K. Yang, X. Zhuang, Y. Jiang, J. Zhang, J. Liu, G. Zou, and X.-J. Liang, "Self-Assembled Peptide Nanofibers Designed as Biological Enzymes for Catalyzing Ester Hydrolysis", *ACS Nano*, Vol. 8, No. 11, pp. 11715–11723, 2014.

7. Xing, X., Y. Wang, and B. Li, “Nanofibers Drawing and Nanodevices Assembly in Poly(Trimethylene Terephthalate)”, *Optics Express*, Vol. 16, No. 14, p. 16815, 2008.

8. Altinbasak, I., R. Jijie, A. Barras, B. Golba, R. Sanyal, J. Bouckaert, D. Drider, R. Bilyy, T. Dumych, S. Paryzhak, V. Vovk, R. Boukherroub, A. Sanyal, and S. Szunerits, “Reduced Graphene-Oxide-Embedded Polymeric Nanofiber Mats: An ‘On-Demand’ Photothermally Triggered Antibiotic Release Platform”, *ACS Applied Materials & Interfaces*, Vol. 10, No. 48, pp. 41098–41106, 2018.

9. Nayak, R., R. Padhye, I.L. Kyratzis, Y.B. Truong, and L. Arnold, “Recent Advances in Nanofibre Fabrication Techniques”, *Textile Research Journal*, Vol. 82, No. 2, pp. 129–147, 2012.

10. Beachley, V., and X. Wen, “Polymer Nanofibrous Structures: Fabrication, Biofunctionalization, and Cell Interactions”, *Progress in Polymer Science*, Vol. 35, No. 7, pp. 868–892, 2010.

11. Mishra R., and L. Sravanthi, “Modern Chemistry & Applications Fabrication Techniques of Micro/Nano Fibres Based Nonwoven Composites: A Review”, *Modern Chemistry & Applications*, Vol. 5, No. 2, p. 1, 2017.

12. Nauman, S., G. Lubineau, and H.F. Alharbi, “Post Processing Strategies for The Enhancement of Mechanical Properties of Enms (Electrospun Nanofibrous Membranes): A Review”, *Membranes*, Vol. 11, No. 1, pp. 1–38, 2021.

13. Subbiah, T., G.S. Bhat, R.W. Tock, S. Parameswaran, and S.S. Ramkumar, “Electrospinning Of Nanofibers”, *Journal of Applied Polymer Science*, Vol. 96, No. 2, pp. 557–569, 2005.

14. Aliheidari, N., N. Aliahmad, M. Agarwal, and H. Dalir, “Electrospun Nanofibers for Label-Free Sensor Applications”, *Sensors*, Vol. 19, No. 16, p. 3587, 2019.

15. Persano, L., A. Camposeo, C. Tekmen, and D. Pisignano, “Industrial Upscaling of Electrospinning and Applications of Polymer Nanofibers: A Review”, *Macromolecular Materials and Engineering*, Vol. 298, No. 5, pp. 504–520, 2013.

16. Li, Z., and C. Wang, “Effects of Working Parameters on Electrospinning”, *SpringerBriefs in Materials*, pp. 15–28, 2013.

17. T. M., S., A. Bin Arshad, P.T. Lin, J. Widakdo, H. K. Makari, H.F.M. Austria, C.C. Hu, J.Y. Lai, and W.S. Hung, “A Review of Recent Progress in Polymeric Electrospun Nanofiber Membranes in Addressing Safe Water Global Issues”, *RSC Advances*, Vol. 11, No. 16, pp. 9638–9663, 2021.

18. Koski, A., K. Yim, and S. Shivkumar, “Effect of Molecular Weight on Fibrous PVA Produced by Electrospinning”, *Materials Letters*, Vol. 58, No. 3-4, pp. 493–497, 2004.

19. Park, J.Y., I.H. Lee, and G.N. Bea, “Optimization of The Electrospinning Conditions for Preparation of Nanofibers from Polyvinylacetate (PVAc) in Ethanol Solvent”, *Journal of Industrial and Engineering Chemistry*, Vol. 14, No. 6, pp. 707–713, 2008.

20. Zargham, S., S. Bazgir, A. Tavakoli, A.S. Rashidi, and R. Damerchely, “The Effect of Flow Rate on Morphology and Deposition Area of Electrospun Nylon 6 Nanofiber”, *Journal of Engineered Fibers and Fabrics*, Vol. 7, No. 4, pp. 42–49, 2012.

21. Motamedi, A.S., H. Mirzadeh, F. Hajiesmaeilbaigi, S. Bagheri-Khoulenjani, and M.A. Shokrgozar, “Effect of Electrospinning Parameters on Morphological Properties of PVDF Nanofibrous Scaffolds”, *Progress in Biomaterials*, Vol. 6, pp. 113–123, 2017.

22. Wang, X., I.C. Um, D. Fang, A. Okamoto, B.S. Hsiao, and B. Chu, “Formation of Water-Resistant Hyaluronic Acid Nanofibers by Blowing-Assisted Electro-Spinning and Non-Toxic Post Treatments”, *Polymer*, Vol. 46, No. 13, pp. 4853–4867, 2005.

23. Sundaray, B., V. Subramanian, T.S. Natarajan, R.Z. Xiang, C.C. Chang, and W.S. Fann, "Electrospinning of Continuous Aligned Polymer Fibers", *Applied Physics Letters*, Vol. 84, No. 7, pp. 1222–1224, 2004.

24. Sun, Y., S. Cheng, W. Lu, Y. Wang, P. Zhang, and Q. Yao, "Electrospun Fibers and Their Application in Drug Controlled Release, Biological Dressings, Tissue Repair, and Enzyme Immobilization", *RSC Advances*, Vol. 9, No. 44, pp. 25712–25729, 2019.

25. Zhang, P., X. Jiao, and D. Chen, "Fabrication of Electrospun Al2O3 Fibers with CaO–SiO2 Additive", *Materials Letters*, Vol. 91, pp. 23–26, 2013.

26. Hardick, O., B. Stevens, and D.G. Bracewell, "Nanofibre Fabrication in A Temperature and Humidity Controlled Environment for Improved Fibre Consistency", *Journal of Materials Science*, Vol. 46, No. 11, pp. 3890–3898, 2011.

27. Xue, J., T. Wu, Y. Dai, and Y. Xia, "Electrospinning and Electrospun Nanofibers: Methods, Materials, and Applications", *Chemical Reviews*, Vol. 119, No. 8, pp. 5298–5415, 2019.

28. Liu, Y., M. Hao, Z. Chen, L. Liu, Y. Liu, W. Yang, and S. Ramakrishna, "A Review on Recent Advances in Application of Electrospun Nanofiber Materials as Biosensors", *Current Opinion in Biomedical Engineering*, Vol. 13, pp. 174–189, 2020.

29. Memic, A., T. Abudula, H.S. Mohammed, K. Joshi Navare, T. Colombani, and S.A. Bencherif, "Latest Progress in Electrospun Nanofibers for Wound Healing Applications", *ACS Applied Bio Materials*, Vol. 2, No. 3, pp. 952–969, 2019.

30. Greiner, A., and J.H. Wendorff, "Electrospinning: A Fascinating Method for The Preparation of Ultrathin Fibers", *Angewandte Chemie - International Edition*, Vol. 46, No. 30, pp. 5670–5703, 2007.

31. Boateng, J.S., K.H. Matthews, H.N.E. Stevens, and G.M. Eccleston, “Wound Healing Dressings and Drug Delivery Systems: A Review”, *Journal of Pharmaceutical Sciences*, Vol. 97, No. 8, pp. 2892–2923, 2008.

32. Zhang, X., R. Lv, L. Chen, R. Sun, Y. Zhang, R. Sheng, T. Du, Y. Li, and Y. Qi, “A Multifunctional Janus Electrospun Nanofiber Dressing with Biofluid Draining, Monitoring, and Antibacterial Properties for Wound Healing”, *ACS Applied Materials and Interfaces*, Vol. 14, No. 11, pp. 12984–13000, 2022.

33. Lee, S., A.R. Cho, D. Park, J.K. Kim, K.S. Han, I.J. Yoon, M.H. Lee, and J. Nah, “Reusable Polybenzimidazole Nanofiber Membrane Filter for Highly Breathable PM 2.5 Dust Proof Mask”, *ACS Applied Materials and Interfaces*, Vol. 11, No. 3, pp. 2750–2757, 2019.

34. Roche, R., and F. Yalcinkaya, “Electrospun Polyacrylonitrile Nanofibrous Membranes for Point-of-Use Water and Air Cleaning”, *ChemistryOpen*, Vol. 8, No. 1, pp. 97–103, 2019.

35. Jiang, Z., H. Zhang, M. Zhu, D. Lv, J. Yao, R. Xiong, and C. Huang, “Electrospun Soy-Protein-Based Nanofibrous Membranes for Effective Antimicrobial Air Filtration”, *Journal of Applied Polymer Science*, Vol. 135, No. 8, p. 45766, 2018.

36. Chen, S., S. Jiang, and H. Jiang, “A Review On Conversion of Crayfish-Shell Derivatives to Functional Materials and Their Environmental Applications”, *Journal of Bioresources and Bioproducts*, Vol. 5, No. 4, pp. 238–247, 2020.

37. Yang, X., Y. Pu, S. Li, X. Liu, Z. Wang, D. Yuan, and X. Ning, “Electrospun Polymer Composite Membrane with Superior Thermal Stability and Excellent Chemical Resistance for High-Efficiency PM2.5 Capture”, *ACS Applied Materials and Interfaces*, Vol. 11, No. 46, pp. 43188–43199, 2019.

38. Seong, D.Y., M.S. Choi, and Y.J. Kim, “Fluorescent Chemosensor for The Detection of Histamine Based On Dendritic Porphyrin-Incorporated Nanofibers”, *European Polymer Journal*, Vol. 48, No. 12, pp. 1988–1996, 2012.

39. Wang, H., W. Tang, H. Wei, Y. Zhao, S. Hu, Y. Guan, W. Pan, B. Xia, N. Li, and F. Liu, “Integrating Dye-Intercalated DNA Dendrimers with Electrospun Nanofibers: A New Fluorescent Sensing Platform for Nucleic Acids, Proteins, and Cells”, *Journal of Materials Chemistry B*, Vol. 3, No. 17, pp. 3541–3547, 2015.

40. Zhou, C., Y. Shi, X. Ding, M. Li, J. Luo, Z. Lu, and D. Xiao, “Development of A Fast and Sensitive Glucose Biosensor Using Iridium Complex-Doped Electrospun Optical Fibrous Membrane”, *Analytical Chemistry*, Vol. 85, No. 2, pp. 1171–1176, 2013.

41. Frias, I.A.M., L.H. Vega Gonzales Gil, M.T. Cordeiro, M.D.L. Oliveira, and C.A.S. Andrade, “Self-Enriching Electrospun Biosensors for Impedimetric Sensing of Zika Virus”, *ACS Applied Materials and Interfaces*, Vol. 14, No. 1, pp. 41–48, 2022.

42. Huang, C., S.J. Soenen, J. Rejman, B. Lucas, K. Braeckmans, J. Demeester, and S.C. De Smedt, “Stimuli-Responsive Electrospun Fibers and Their Applications”, *Chemical Society Reviews*, Vol. 40, No. 5. pp. 2417–2434, 2011.

43. Chan, Z., Z. Chen, A. Zhang, J. Hu, X. Wang, and Z. Yang, “Electrospun Nanofibers for Cancer Diagnosis and Therapy”, *Biomaterials Science*, Vol. 4, No. 6, pp. 922–932, 2016.

44. Sharma, A., A. Gupta, G. Rath, A. Goyal, R.B. Mathur, and S.R. Dhakate, “Electrospun Composite Nanofiber-Based Transmucosal Patch for Anti-Diabetic Drug Delivery”, *Journal of Materials Chemistry B*, Vol. 1, No. 27, pp. 3410–3418, 2013.

45. Celebioglu, A., and T. Uyar, “Hydrocortisone/Cyclodextrin Complex Electrospun Nanofibers for A Fast-Dissolving Oral Drug Delivery System”, *RSC Medicinal Chemistry*, Vol. 11, No. 2, pp. 245–258, 2020.

46. Li, L., and Y. Lo Hsieh, “Ultra-Fine Polyelectrolyte Fibers from Electrospinning of Poly(Acrylic Acid)”, *Polymer*, Vol. 46, No. 14, pp. 5133–5139, 2005.

47. Li, W., T. Luo, Y. Yang, X. Tan, and L. Liu, “Formation of Controllable Hydrophilic/Hydrophobic Drug Delivery Systems by Electrospinning of Vesicles”, *Langmuir*, Vol. 31, No. 18, pp. 5141–5146, 2015.

48. Lancina, M.G., S. Singh, U.B. Kompella, S. Husain, and H. Yang, “Fast Dissolving Dendrimer Nanofiber Mats as Alternative to Eye Drops for More Efficient Antiglaucoma Drug Delivery”, *ACS Biomaterials Science and Engineering*, Vol. 3, No. 8, pp. 1861–1868, 2017.

49. Breitbach, M., T. Bostani, W. Roell, Y. Xia, O. Dewald, J.M. Nygren, J.W.U. Fries, K. Tiemann, H. Bohlen, J. Hescheler, A. Welz, W. Bloch, S.E.W. Jacobsen, and B.K. Fleischmann, “Potential Risks of Bone Marrow Cell Transplantation into Infarcted Hearts”, *Blood*, Vol. 110, No. 4, pp. 1362-1369, 2007.

50. Sunil Richard, A., and R.S. Verma, “Antioxidant α-Mangostin Coated Woven Polycaprolactone Nanofibrous Yarn Scaffold for Cardiac Tissue Repair”, *ACS Applied Nano Materials*, Vol. 5, No. 4, pp. 5075–5086, 2022.

51. Son, Y.J., Y. Kim, W.J. Kim, S.Y. Jeong, and H.S. Yoo, “Antibacterial Nanofibrous Mats Composed Of Eudragit For PH-Dependent Dissolution.”, *Journal of Pharmaceutical Sciences*, Vol. 104, No. 8, pp. 2611–2618, 2015.

52. Demirci, S., A. Celebioglu, Z. Aytac, and T. Uyar, “PH-Responsive Nanofibers With Controlled Drug Release Properties.”, *Polym. Chem.*, Vol. 5, No. 6, pp. 2050–2056, 2014.

53. Abdalkarim, S.Y.H., H. Yu, C. Wang, Y. Chen, Z. Zou, L. Han, J. Yao, and K.C. Tam, "Thermo And Light-Responsive Phase Change Nanofibers With High Energy Storage Efficiency for Energy Storage And Thermally Regulated On–Off Drug Release Devices", *Chemical Engineering Journal*, Vol. 375, pp. 121979, 2019.

54. Lin, S., X. Huang, R. Guo, S. Chen, J. Lan, and P. Theato, "UV-triggered CO 2 -responsive Behavior of Nanofibers And Their Controlled Drug Release Properties", *Journal of Polymer Science Part A: Polymer Chemistry*, Vol. 57, No. 14, pp. 1580–1586, 2019.

55. Yun, J., J.S. Im, Y.S. Lee, and H. Il Kim, "Electro-Responsive Transdermal Drug Delivery Behavior of PVA/PAA/MWCNT Nanofibers", *European Polymer Journal*, Vol. 47, No. 10, pp. 1893–1902, 2011.

56. Chen, M., Y.-F. Li, and F. Besenbacher, "Electrospun Nanofibers-Mediated On-Demand Drug Release", *Advanced Healthcare Materials*, Vol. 3, No. 11, pp. 1721–1732, 2014.

57. He, H., M. Cheng, Y. Liang, H. Zhu, Y. Sun, D. Dong, and S. Wang, "Intelligent Cellulose Nanofibers with Excellent Biocompatibility Enable Sustained Antibacterial and Drug Release via A PH-Responsive Mechanism", *Journal of Agricultural and Food Chemistry*, Vol. 68, No. 11, pp. 3518–3527, 2020.

58. Pang, Q., X. Zheng, Y. Luo, L. Ma, and C. Gao, "A Photo-Cleavable Polyprodrug-Loaded Wound Dressing with UV-Responsive Antibacterial Property", *Journal of Materials Chemistry B*, Vol. 5, No. 45, pp. 8975–8982, 2017.

59. Hockberger, P.E., "A History Of Ultraviolet Photobiology For Humans, Animals And Microorganisms.", *Photochemistry and photobiology*, Vol. 76, No. 6, pp. 561–579, 2002.

60. Huang, H.Y., A. Skripka, L. Zaroubi, B.L. Findlay, F. Vetrone, C. Skinner, J.K. Oh, and L.A. Cuccia, "Electrospun Upconverting Nanofibrous Hybrids with Smart NIR-Light-Controlled Drug Release for Wound Dressing", *ACS Applied Bio Materials*, Vol. 3, No. 10, pp. 7219–7227, 2020.

61. Cheng, M., H. Wang, Z. Zhang, N. Li, X. Fang, and S. Xu, "Gold Nanorod-Embedded Electrospun Fibrous Membrane as A Photothermal Therapy Platform", *ACS Applied Materials & Interfaces*, Vol. 6, No. 3, pp. 1569–1575, 2014.

62. Zhang, Z., S. Liu, H. Xiong, X. Jing, Z. Xie, X. Chen, and Y. Huang, "Electrospun PLA/MWCNTs Composite Nanofibers for Combined Chemo- and Photothermal Therapy", *Acta Biomaterialia*, Vol. 26, No. 23, pp. 115–123, 2015.

63. Li, Y., Y. Fu, Z. Ren, X. Li, C. Mao, and G. Han, "Enhanced Cell Uptake of Fluorescent Drug-Loaded Nanoparticles via An Implantable Photothermal Fibrous Patch for More Effective Cancer Cell Killing", *Journal of Materials Chemistry B*, Vol. 5, No. 36, pp. 7504–7511, 2017.

64. Qi, K., J. He, H. Wang, Y. Zhou, X. You, N. Nan, W. Shao, L. Wang, B. Ding, and S. Cui, "A Highly Stretchable Nanofiber-Based Electronic Skin With Pressure-, Strain-, And Flexion-Sensitive Properties for Health and Motion Monitoring", *ACS Applied Materials & Interfaces*, Vol. 9, No. 49, pp. 42951–42960, 2017.

65. Luo, Y., H. Shen, Y. Fang, Y. Cao, J. Huang, M. Zhang, J. Dai, X. Shi, and Z. Zhang, "Enhanced Proliferation and Osteogenic Differentiation of Mesenchymal Stem Cells On Graphene Oxide-Incorporated Electrospun Poly(Lactic- Co -Glycolic Acid) Nanofibrous Mats", *ACS Applied Materials & Interfaces*, Vol. 7, No. 11, pp. 6331–6339, 2015.

66. Wang, S.-D., Q. Ma, K. Wang, and H.-W. Chen, "Improving Antibacterial Activity and Biocompatibility of Bioinspired Electrospinning Silk Fibroin Nanofibers Modified by Graphene Oxide", *ACS Omega*, Vol. 3, No. 1, pp. 406–413, 2018.

67. Smith, A.T., A.M. LaChance, S. Zeng, B. Liu, and L. Sun, “Synthesis, Properties, and Applications of Graphene Oxide/Reduced Graphene Oxide and Their Nanocomposites”, *Nano Materials Science*, Vol. 1, No. 1, pp. 31–47, 2019.

68. Tarcan, R., O. Todor-Boer, I. Petrovai, C. Leordean, S. Astilean, and I. Botiz, “Reduced Graphene Oxide Today”, *Journal of Materials Chemistry C*, Vol. 8, No. 4, pp. 1198–1224, 2020.

69. Amieva, E.J., J. López-Barroso, A.L. Martínez-Hernández, and C. Velasco-Santos, “Graphene-Based Materials Functionalization with Natural Polymeric Biomolecules”, *Recent Advances in Graphene Research*, Vol. 12, p. 308, 2016.

70. Saha, B., S. Baek, and J. Lee, “Highly Sensitive Bendable and Foldable Paper Sensors Based On Reduced Graphene Oxide”, *ACS Applied Materials and Interfaces*, Vol. 9, No. 5, pp. 4658–4666, 2017.

71. Choudhary, P., T. Parandhaman, B. Ramalingam, N. Duraipandy, M. Syamala Kiran, and S.K. Das, “Fabrication of Nontoxic Reduced Graphene Oxide Protein Nanoframework as Sustained Antimicrobial Coating for Biomedical Application”, Vol. 9, No. 44, pp. 38255-38269, 2017.

72. Liu, Y., Z. Chen, Y. Zhang, R. Feng, X. Chen, C. Xiong, and L. Dong, “Broadband and Lightweight Microwave Absorber Constructed by In Situ Growth of Hierarchical CoFe2O4/Reduced Graphene Oxide Porous Nanocomposites”, *ACS Applied Materials and Interfaces*, Vol. 10, No. 16, pp. 13860–13868, 2018.

73. Shao, L., R. Zhang, J. Lu, C. Zhao, X. Deng, and Y. Wu, “Mesoporous Silica Coated Polydopamine Functionalized Reduced Graphene Oxide for Synergistic Targeted Chemo-Photothermal Therapy”, *ACS Applied Materials and Interfaces*, Vol. 9, No. 2, pp. 1226–1236, 2017.

74. Clement, M., G. Daniel, and M. Trelles, “Optimising The Design Of A Broad-band Light Source for The Treatment of Skin”, *Journal of Cosmetic and Laser Therapy*, Vol. 7, No. 3-4, pp. 177–189, 2009.

75. Ramesh, K., S. Yadav, A.K. Mishra, S.H. Jo, S.H. Park, C.W. Oh, and K.T. Lim, “Interface-Cross-Linked Micelles of Poly(D,L-Lactide)-B-Poly(Furfuryl Methacrylate)-B-Poly(N-Acryloylmorpholine) for Near-Infrared-Triggered Drug Delivery Application”, *Polymers for Advanced Technologies*, Vol. 33, No. 7, pp. 2137–2148, 2022.

76. Tasdelen, M.A., “Diels-Alder ‘Click’ Reactions: Recent Applications in Polymer and Material Science”, *Polymer Chemistry*, Vol. 2, No. 10, pp. 2133–2145, 2011.

77. Bao, W., Y. Liu, X. Lv, and W. Qian, “Cu 2 O-Catalyzed Tandem Ring-Opening / Coupling Cyclization Process for The 2 , 3-Dihydro-1 , 4-Benzodioxins”, *Organic Letters*, Vol. 10, No. 17, pp. 3899-3902, 2008.

78. Heredia, K.L., Z.P. Tolstyka, and H.D. Maynard, “Aminooxy End-Functionalized Polymers Synthesized by ATRP for Chemoselective Conjugation to Proteins”, *Macromolecules*, Vol. 40, No. 14, pp. 4772–4779, 2007.

79. Cengiz, N., T.N. Gevrek, R. Sanyal, and A. Sanyal, “Orthogonal Thiol-Ene ‘click’ Reactions: A Powerful Combination for Fabrication and Functionalization of Patterned Hydrogels”, *Chemical Communications*, Vol. 53, No. 63, pp. 8894–8897, 2017.

80. Diels, O., and K. Alder, “Synthesen In Der Hydroaromatischen Reihe.”, *Justus Liebigs Annalen der Chemie*, Vol. 460, No. 1, pp. 98–122, 1928.

81. Gevrek, T.N., and A. Sanyal, “Furan-Containing Polymeric Materials: Harnessing The Diels-Alder Chemistry for Biomedical Applications”, *European Polymer Journal*, Vol. 153, p. 110514, 2021.

82. Froidevaux, V., M. Borne, E. Laborbe, R. Auvergne, A. Gandini, and B. Boutevin, "Study of The Diels-Alder and Retro-Diels-Alder Reaction Between Furan Derivatives and Maleimide for The Creation of New Materials", *RSC Advances*, Vol. 5, No. 47, pp. 37742–37754, 2015.

83. Gevrek, T.N., R.N. Ozdeslik, G.S. Sahin, G. Yesilbag, S. Mutlu, and A. Sanyal, "Functionalization of Reactive Polymeric Coatings via Diels-Alder Reaction Using Microcontact Printing", *Macromolecular Chemistry and Physics*, Vol. 213, No. 2, pp. 166–172, 2012.

84. Arrizabalaga, J.H., M. Smallcomb, M. Abu-Laban, Y. Liu, T.J. Yeingst, A. Dhawan, J.C. Simon, and D.J. Hayes, "Ultrasound-Responsive Hydrogels for On-Demand Protein Release", *ACS Applied Bio Materials*, Vol. 5, No. 7, pp. 3212-3218, 2022.

85. Pramanik, N.B., and N.K. Singha, "Amphiphilic Functional Block Copolymers Bearing A Reactive Furfuryl Group via RAFT Polymerization; Reversible Core Cross-Linked Micelles via A Diels–Alder 'Click Reaction'", *RSC Advances*, Vol. 6, No. 3, pp. 2455–2463, 2015.

86. Turkenburg, D.H., Y. Durant, and H.R. Fischer, "Bio-Based Self-Healing Coatings Based On Thermo-Reversible Diels-Alder Reaction", *Progress in Organic Coatings*, Vol. 111, pp. 38–46, 2017.

87. Kalaoglu-Altan, O.I., R. Sanyal, and A. Sanyal, "'Clickable' Polymeric Nanofibers Through Hydrophilic–Hydrophobic Balance: Fabrication of Robust Biomolecular Immobilization Platforms", *Biomacromolecules*, Vol. 16, No. 5, pp. 1590–1597, 2015.

88. Ling, Y., Y. Gao, C. Shu, Y. Zhou, W. Zhong, and B. Xu, "Using A Peptide Segment to Covalently Conjugate Doxorubicin and Taxol for The Study of Drug Combination Effect", *RSC Advances*, Vol. 5, No. 123, pp. 101475–101479, 2015.

APPENDIX: COPYRIGHT NOTICES

Copyrights notices for the figures used are provided in this section.

Figure A.1. Copyright for Figure 1.1.

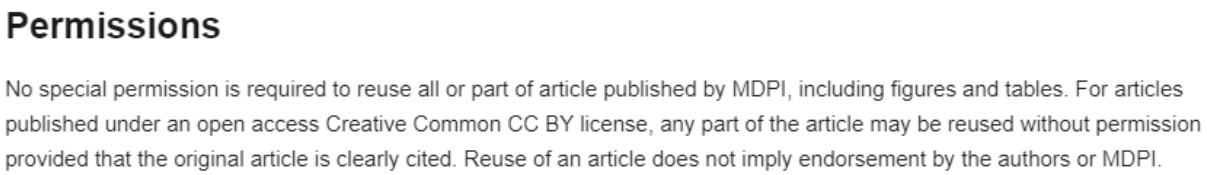

Figure A.2. Copyright for Figure 1.2.

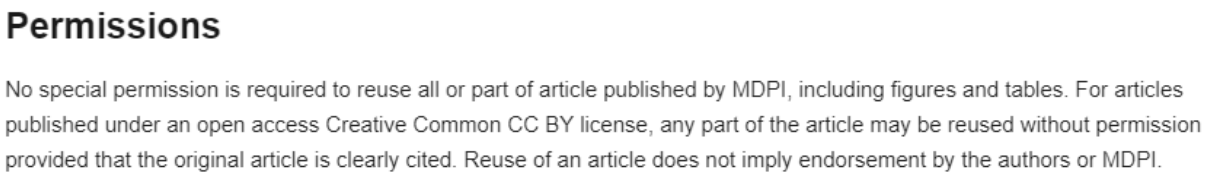

Figure A.3. Copyright for Figure 1.3.

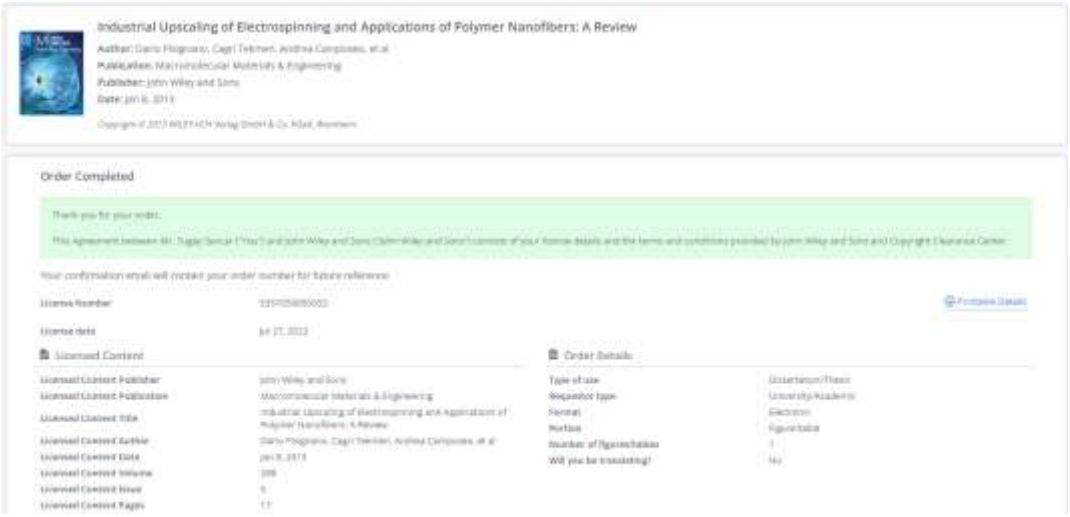

Figure A.4. Copyright for Figure 1.4.

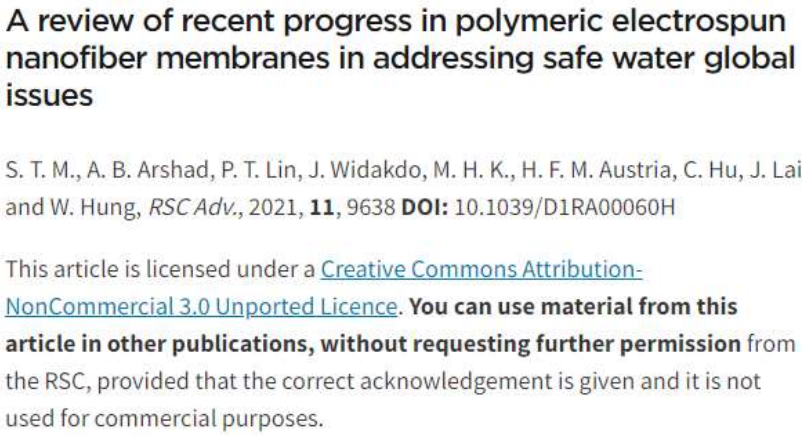

A review of recent progress in polymeric electrospun nanofiber membranes in addressing safe water global issues

S. T. M., A. B. Arshad, P. T. Lin, J. Widakdo, M. H. K., H. F. M. Austria, C. Hu, J. Lai and W. Hung, *RSC Adv.*, 2021, **11**, 9638 **DOI:** 10.1039/D1RA00060H

Figure A.5. Copyright for Figure 1.5.

Figure A.6. Copyright for Figure 1.6.

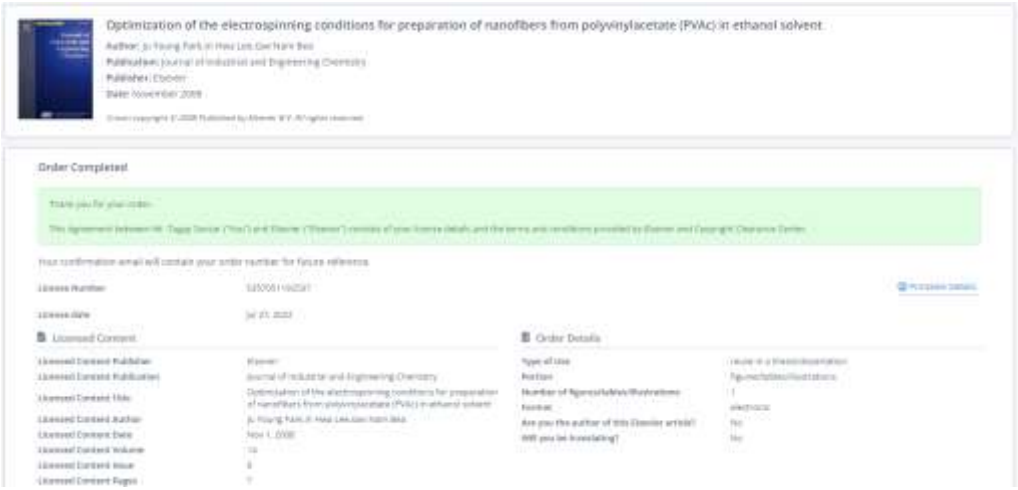

Figure A.7. Copyright for Figure 1.7.

Figure A.8. Copyright for Figure 1.8.

Figure A.9. Copyright for Figure 1.9.

Figure A.10. Copyright for Figure 1.10.

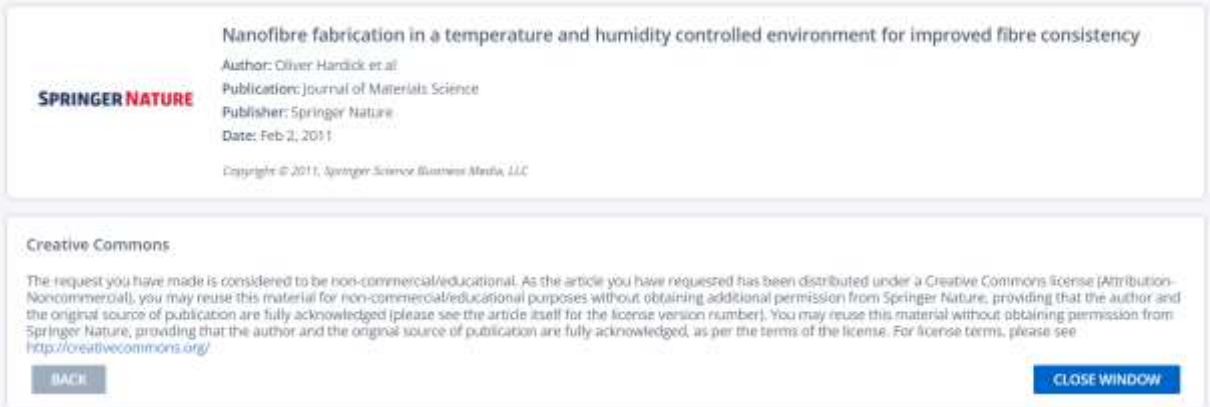

Figure A.11. Copyright for Figure 1.11.

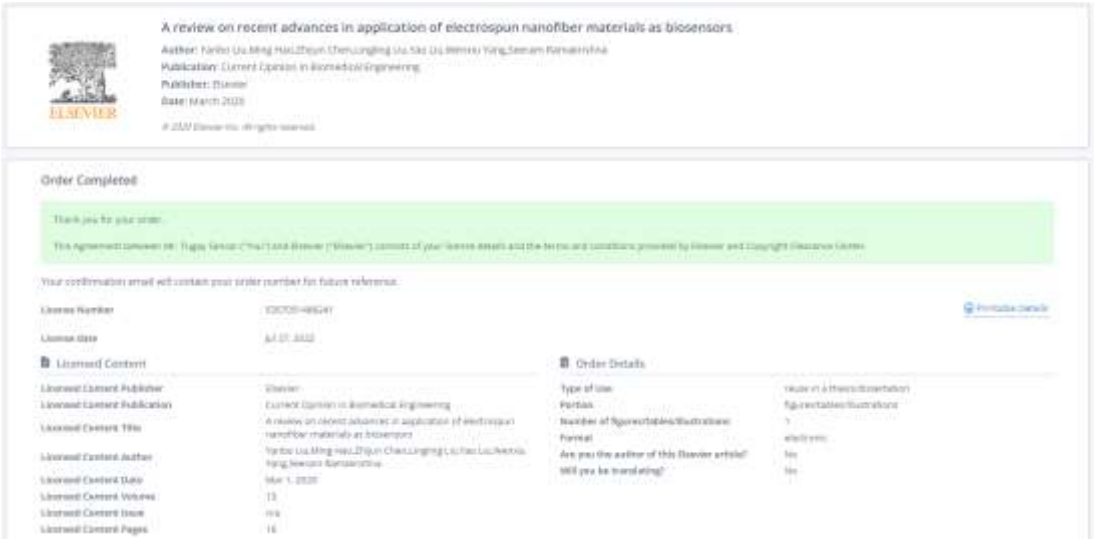

Figure A.12. Copyright for Figure 1.12.

Figure A.13. Copyright for Figure 1.13.

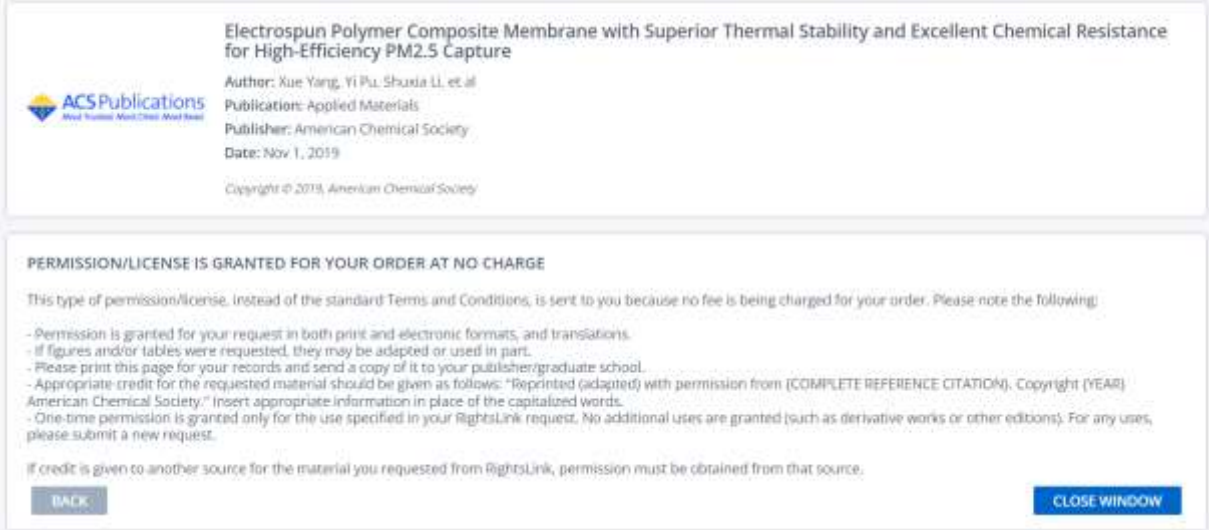

Electrospun Polymer Composite Membrane with Superior Thermal Stability and Excellent Chemical Resistance for High-Efficiency PM2.5 Capture

Author: Xue Yang, Yi Pu, Shuxia Li, et al
Publication: Applied Materials
Publisher: American Chemical Society
Date: Nov 1, 2019

Figure A.14. Copyright for Figure 1.14.

Self-Enriching Electrospun Biosensors for Impedimetric Sensing of Zika Virus

Author: Isaac A. M. Frias, Laura Helena Vega Gonzales Gil, Marli T. Cordeiro, et al
Publication: Applied Materials
Publisher: American Chemical Society
Date: Jan 1, 2022

Figure A.15. Copyright for Figure 1.15.

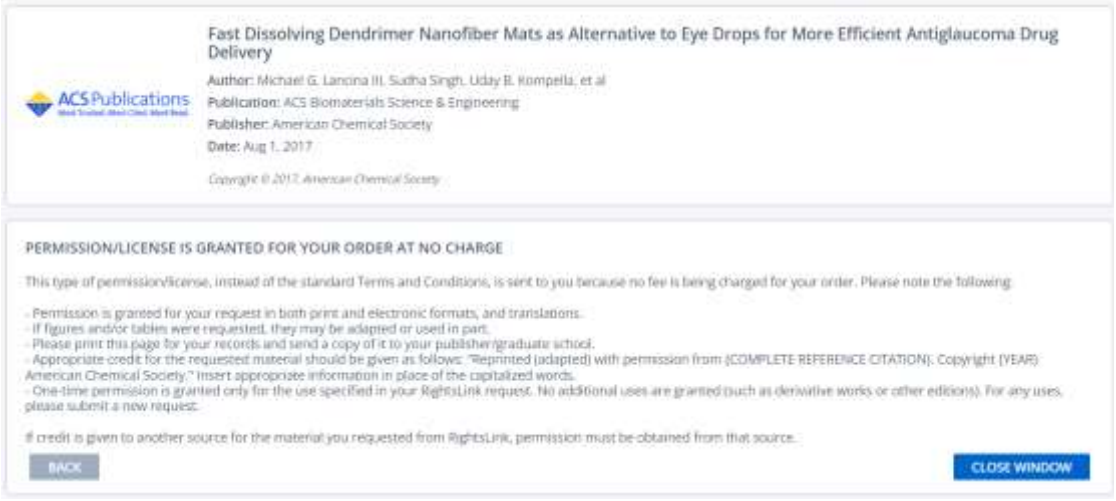

Fast Dissolving Dendrimer Nanofiber Mats as Alternative to Eye Drops for More Efficient Antiglaucoma Drug Delivery

Author: Michael G. Lancina III, Sudha Singh, Uday B. Kompella, et al
Publication: ACS Biomaterials Science & Engineering
Publisher: American Chemical Society
Date: Aug 1, 2017

Figure A.16. Copyright for Figure 1.16.

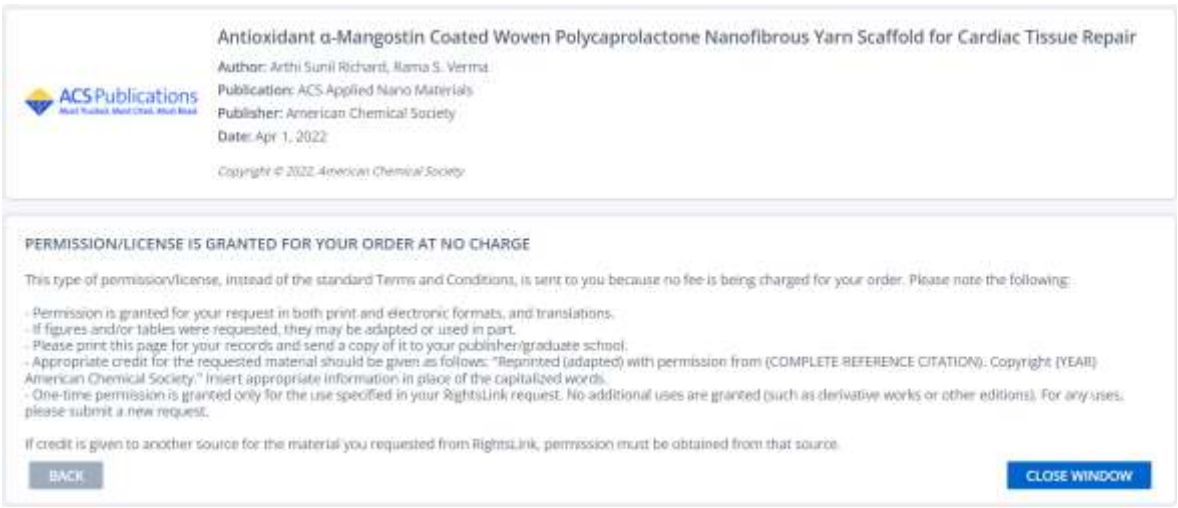

Antioxidant α-Mangostin Coated Woven Polycaprolactone Nanofibrous Yarn Scaffold for Cardiac Tissue Repair

Author: Arthi Sunil Richard, Rama S. Verma
Publication: ACS Applied Nano Materials
Publisher: American Chemical Society
Date: Apr 1, 2022

Figure A.17. Copyright for Figure 1.17.

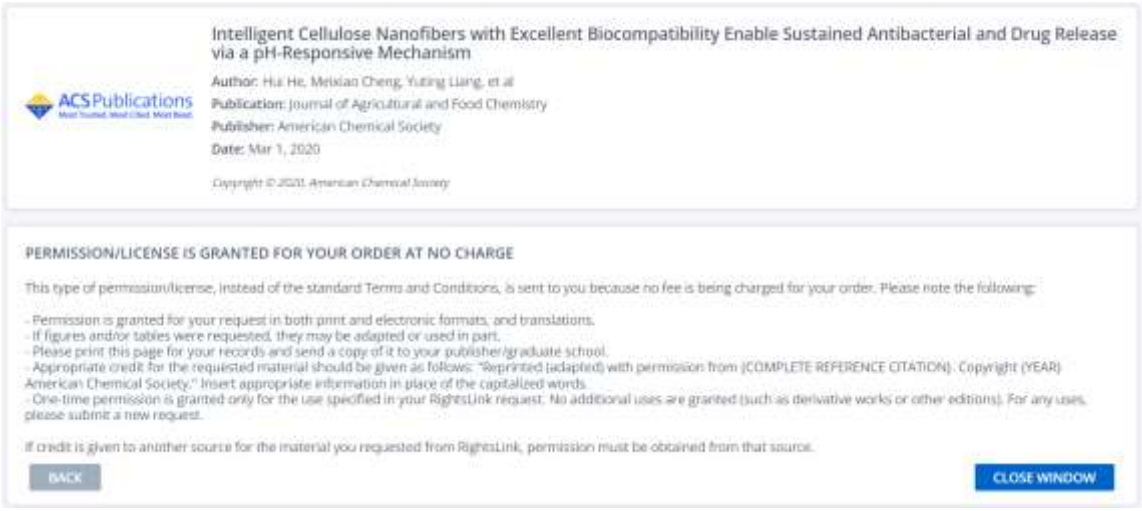

Intelligent Cellulose Nanofibers with Excellent Biocompatibility Enable Sustained Antibacterial and Drug Release via a pH-Responsive Mechanism

Author: Hui He, Meixian Cheng, Yuting Liang, et al
Publication: Journal of Agricultural and Food Chemistry
Publisher: American Chemical Society
Date: Mar 1, 2020

PERMISSION/LICENSE IS GRANTED FOR YOUR ORDER AT NO CHARGE

This type of permission/license, instead of the standard Terms and Conditions, is sent to you because no fee is being charged for your order. Please note the following:

- Permission is granted for your request in both print and electronic formats, and translations.
- If figures and/or tables were requested, they may be adapted or used in part.
- Please print this page for your records and send a copy of it to your publisher/graduate school.
- Appropriate credit for the requested material should be given as follows: "Reprinted (adapted) with permission from (COMPLETE REFERENCE CITATION). Copyright (YEAR) American Chemical Society." Insert appropriate information in place of the capitalized words.
- One-time permission is granted only for the use specified in your RightsLink request. No additional uses are granted (such as derivative works or other editions). For any uses, please submit a new request.

If credit is given to another source for the material you requested from RightsLink, permission must be obtained from that source.

BACK CLOSE WINDOW

Figure A.18. Copyright for Figure 1.18.

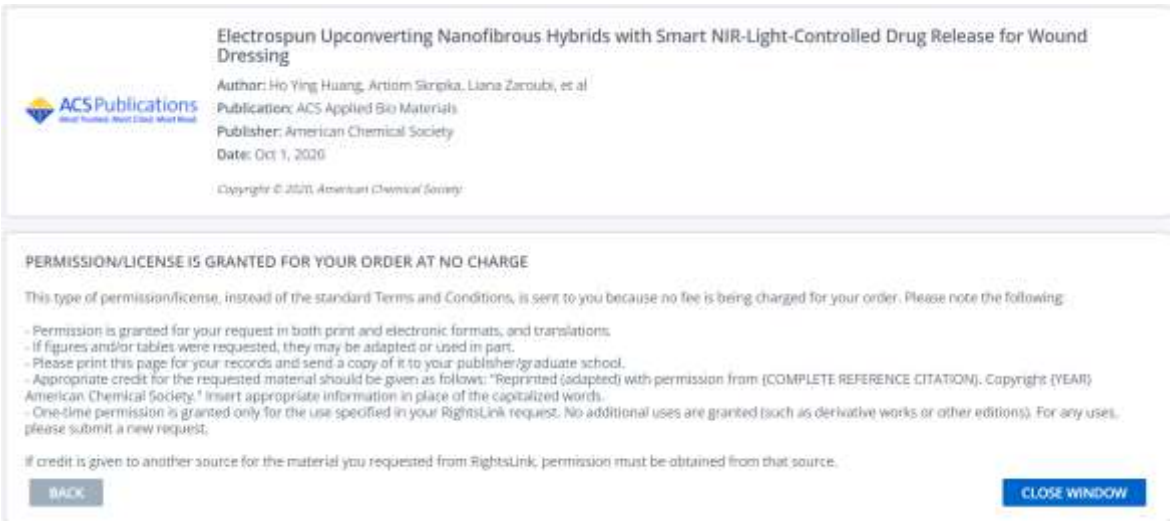

Electrospun Upconverting Nanofibrous Hybrids with Smart NIR-Light-Controlled Drug Release for Wound Dressing

Author: Ho Ying Huang, Artiom Skripka, Liana Zaroubi, et al
Publication: ACS Applied Bio Materials
Publisher: American Chemical Society
Date: Oct 1, 2020

PERMISSION/LICENSE IS GRANTED FOR YOUR ORDER AT NO CHARGE

This type of permission/license, instead of the standard Terms and Conditions, is sent to you because no fee is being charged for your order. Please note the following:

- Permission is granted for your request in both print and electronic formats, and translations.
- If figures and/or tables were requested, they may be adapted or used in part.
- Please print this page for your records and send a copy of it to your publisher/graduate school.
- Appropriate credit for the requested material should be given as follows: "Reprinted (adapted) with permission from (COMPLETE REFERENCE CITATION). Copyright (YEAR) American Chemical Society." Insert appropriate information in place of the capitalized words.
- One-time permission is granted only for the use specified in your RightsLink request. No additional uses are granted (such as derivative works or other editions). For any uses, please submit a new request.

If credit is given to another source for the material you requested from RightsLink, permission must be obtained from that source.

BACK CLOSE WINDOW

Figure A.19. Copyright for Figure 1.19.

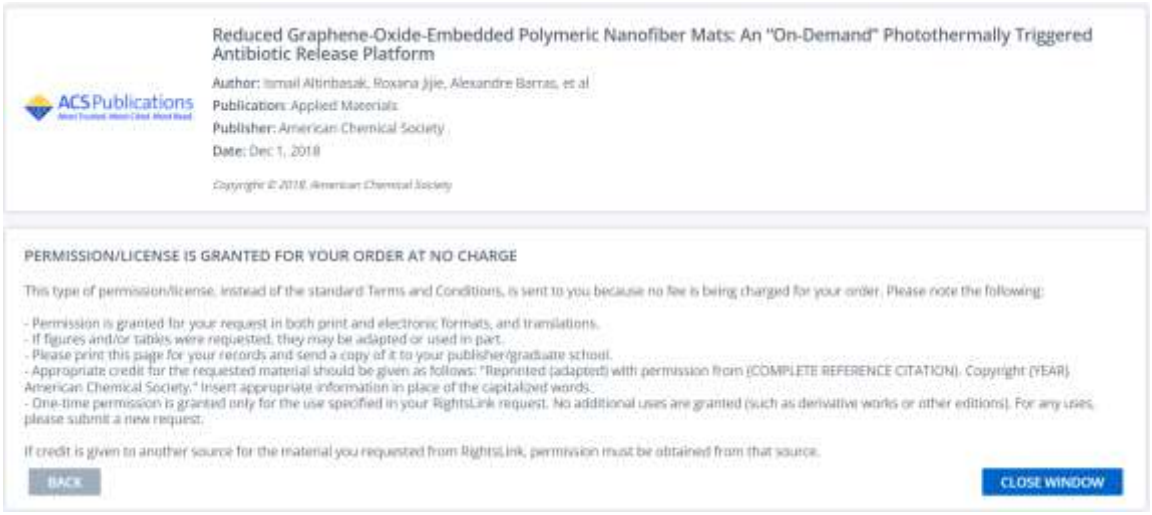

Figure A.20. Copyright for Figure 1.20.

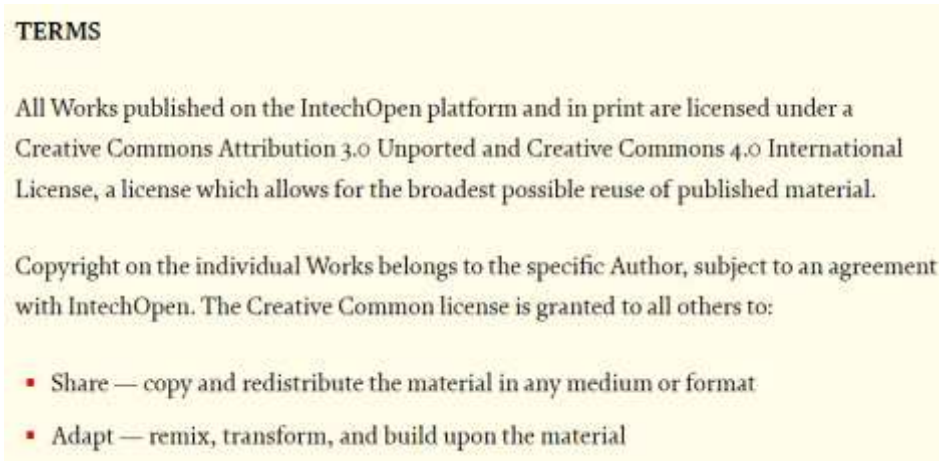

Figure A.21. Copyright for Figure 1.21.

Figure A.22. Copyright for Figure 1.22.

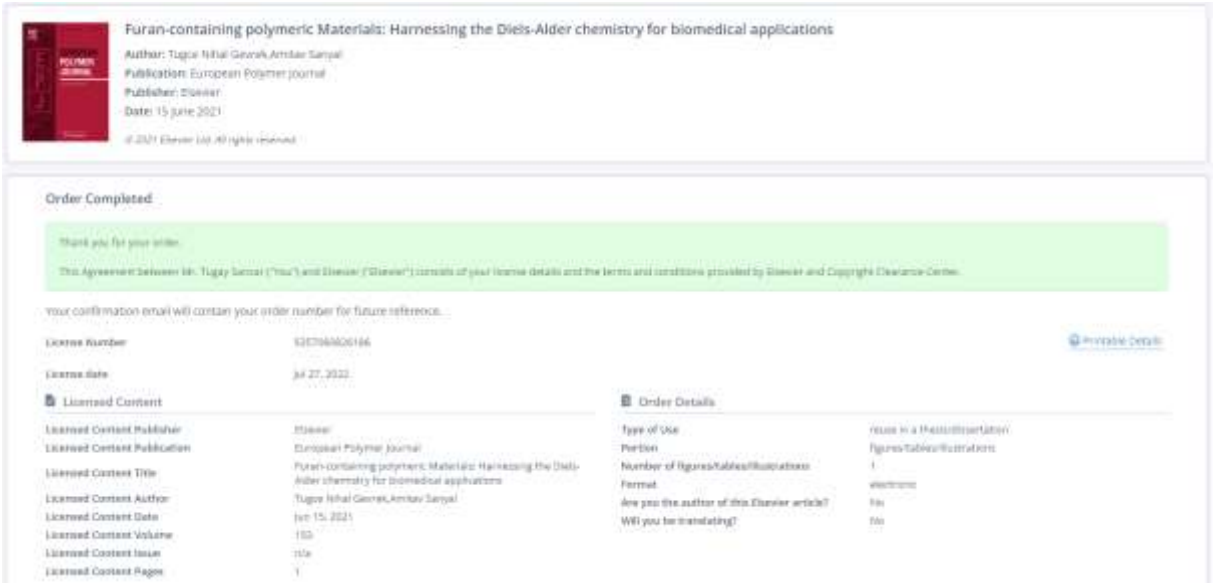

Figure A.23. Copyright for Figure 1.23.

Figure A.24. Copyright for Figure 1.24.